The Hong Kong Polytechnic University

Department of Electronic and Information Engineering

Bifurcation Analysis of Three-Phase Grid-connected Converters

Meng HUANG

Supervisor: Prof. C. K. Michael Tse

A thesis submitted in partial fulfilment of

the requirements for the degree of

Doctor of Philosophy

March 2013

Certificate of Originality

I hereby declare that this thesis is my own work and that, to the best of my knowledge and belief, it reproduces no material previously published or written nor material which has been accepted for the award of any other degree or diploma, except where due acknowledgment has been made in the text.

_____(Signed)

Meng HUANG (Name of student)

Abstract

This thesis aims to identify and analyze the nonlinear behavior in the three-phase voltage source converter, which is widely used as an interface converter in a distributed hybrid power system (DHPS). In this system, the converter does not work as a standalone converter but operates as a subsystem that connects to a non-ideal power grid and interacts indirectly with other subsystems via a point of common coupling (PCC). It has been observed that specific bifurcation phenomena occur in this grid-connected system. Bifurcation analysis is carried out to identify these phenomena, and a design-oriented analysis is adopted to derive practical parameter boundaries that divide the various possible operating regimes.

Specifically, a catastrophic bifurcation is identified for the three-phase voltage source converter. When this bifurcation occurs, the DC output of the converter will collapse, and the input line current will expand to a very high level, which is dangerous for the grid. A set of design-oriented parameter boundaries are given. Also, the cause of this special bifurcation is identified by inspecting the nonlinear operation of the converter circuit. This phenomenon is studied experimentally in this thesis.

Furthermore, an irreversible bifurcation phenomenon is reported in a three-phase voltage source converter connected to a non-ideal power grid with an interacting load, which represents a practical form of system configuration. Due to the limited input active power given to the converter by the power grid, the

DC voltage of the converter will drop when the converter fails to get the power it needs. The converter then sinks reactive power and operates "abnormally". A large-signal analysis is adopted to identify the physical origin of the phenomenon and to locate the boundary of the instability. The phenomenon is verified experimentally.

Finally, a low-frequency Hopf-type instability phenomenon in the three-phase voltage source converter is identified when the converter is connected to a non-ideal power grid. An averaged model has been developed for the grid-connected converter system to predict the low-frequency instability. Additionally, as a result of the emergence of low-frequency oscillation, it is found that the stability boundary leading to a catastrophic bifurcation is significantly varied. The low-frequency instability and its effects on the stability margin are verified experimentally.

Publications

Journal papers

- **M. Huang**, C. K. Tse, S.-C. Wong, C. Wan and X. Ruan, "Low-frequency Hopf bifurcation and its effects on stability margin in three-phase PFC power supplies connected to non-ideal power grid," *IEEE Transactions on Circuits and Systems I—Regular Papers*, to appear.

- **M. Huang**, S.-C. Wong, C. K. Tse, and X. Ruan, "Catastrophic bifurcation in three-phase voltage-source converters," *IEEE Transactions on Circuits and Systems I—Regular Papers*, vol. 60, no. 4, pp. 1062–1071, Apr. 2013.

- C. Wan, **M. Huang**, C. K. Tse, S.-C. Wong and X. Ruan, "Nonlinear behavior and instability in three-phase boost rectifier connected to non-ideal power grid with an interacting load," *IEEE Transactions on Power Electronics*, vol. 28, no. 7, pp. 3255–3265, Jul. 2013.

- C. Wan, **M. Huang**, C. K. Tse, S.-C. Wong and X. Ruan, "Irreversible bifurcation phenomenon in power-grid connected converter systems," *International Journal of Bifurcations and Chaos*, vol. 22, no. 6, pp. 1250155-1–8, Jun. 2012.

Conference papers

- **M. Huang**, C. K. Tse and S.-C. Wong, "Hopf-type bifurcation in three-phase PFC power supplies connected to non-ideal power grid," *International Workshop on Chaos-Fractals Theory and Applications*, (IWCFTA 2012), Dalian, China, pp. 151–154, Oct. 2012.

- C. Wan, **M. Huang**, C. K. Tse, S.-C. Wong and X. Ruan, "Irreversible instability in three-phase voltage source converter connected to non-ideal power grid with interacting load," *IEEE Energy Conversion Congress and Exposition*, (IEEE ECCE 2012), Raleigh, North Carolina, USA, pp. 1406–1411, Sep. 2012.

- **M. Huang**, C. K. Tse and S.-C. Wong, "Line-frequency instability of three-phase PFC power supplies connecting to non-ideal power grid," *IEEE International Symposium on Circuits and Systems*, (IEEE ISCAS 2012), Seoul, Korea, pp. 213–216, May 2012.

- **M. Huang**, C. K. Tse, S.-C. Wong and X. Ruan, "Catastrophic bifurcation in three-phase voltage source converters," *International Workshop on Chaos-Fractals Theories and Applications*, (IWCFTA 2011), Hangzhou, China, pp. 147–151, Oct. 2011.

- **M. Huang**, S.-C. Wong, C. K. Tse and X. Ruan, "Catastrophic bifurcation in three-phase boost rectifiers," *IEEE Energy Conversion Congress and Exposition*, (IEEE ECCE 2011), Phoenix, Arizona, USA, pp. 1381–1384, Sep. 2011.

Acknowledgments

It is my great fortune to have the opportunity of pursuing my PhD study under the guidance of my supervisor, Prof. C. K. Michael Tse. I would like to express my sincere thanks to him for providing me a conducive environment for research, mental catalyst to innovative thinking, inspiring discussion for effective problem solving, and patient guidance when I was struggling with my study. He is always enthusiastic in giving suggestions that stimulate further thoughts on the research of power electronic circuits and systems. And he is so kind as to share his philosophy which is beneficial to me in all aspects of my life. I have had a very pleasant time during my study in his group.

I would also like to thank Dr. S. C. Wong for his great suggestions and help on my research work. His constructive ideas and views help me move forward in the course of my research. The many effective comments and discussions help me find and solve the problems effectively. I am also very grateful to all the colleagues and friends of the Applied Nonlinear Circuits and Systems Research Group. I really enjoy the environment and collaboration here.

I gratefully acknowledge the Research Committee of The Hong Kong Polytechnic University for its financial support during the entire period of my candidate.

Last but not least, I would like to thank my mother for her love and sacrifice which have always been the biggest motivation for me to move forward.

Contents

List of Figures

List of Tables

Chapter 1

Introduction

1.1 Motivation

Power generation systems were first constructed in 1881. Over the past 130 years, a simple centralized structure has been adopted for power distribution, in which electric power is generated from central generating plants and transmitted to the final users unidirectionally. With the increasing demand of electric power, huge generating plants and complex distribution networks have been developed. However, the system suffers from a number of disadvantages. First, the system requires the consumption of chemical energy resources such as coal and natural gas. The use of these fossil fuels has negative effects on the environment as it produces greenhouse gases like carbon dioxide, sulfur dioxide, etc. These kinds of non-renewable resources are limited on our earth. At the current rate of energy consumption, the non-renewable resources may only sustain for about 100 more years, posing a serious "energy crisis" for our earth [1]. As a result, the use of renewable or alternative energy sources has been growing rapidly. Up to 2011, renewable energy has accounted for over 25% of the world's total energy consumption. The actual amount of global renewable power capacity grows even faster, as shown in Fig. 1.1 [2].

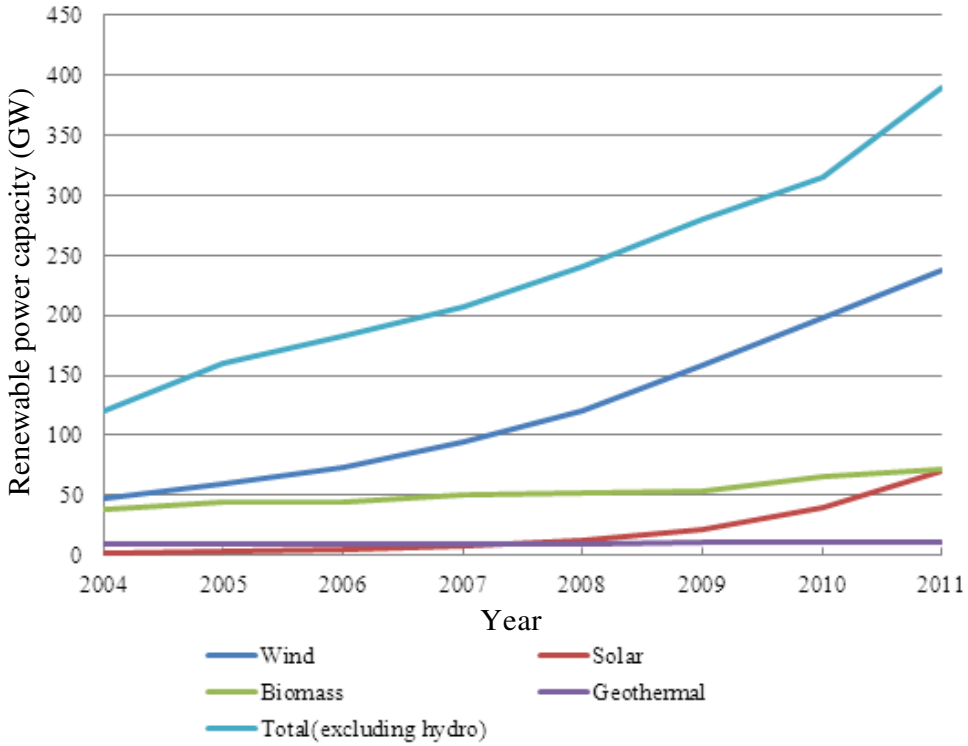

Figure 1.1: Global renewable power capacity excluding hydroelectric power.

Secondly, the centralized structure of the power grid is prone to intentional attacks. When one central generation plant collapses, the whole grid it supports will be blacked out. In the northeast blackout of 2003 in the U.S. and Canada, the failures of several key transmission lines made one power station go offline. This fault spread out through the power grid quickly and finally affected an estimated 10 million people in Ontario and 45 million people in eight U.S. states [3]. Blackouts would cause serious consequences due to the highly dependence on electricity of many cities. Transportation systems will be paralyzed without electricity, commercial activities and public services would be forced to shut down causing great financial losses. More recently, the blackout in India left more than 600 million people without electricity [4].

In order to provide robust power distribution, some new technologies have been developed. One popular solution is the distributed generation system. Distributed generation is an effective approach to the manufacture and transmission

of electric power. It reduces the amount of energy lost in transmitting electricity because energy is generated very near where it is used, even at the same premises. This reduces the size and number of power lines that must be constructed. If renewable energy resources are used as distributed generation resources, the resulting distributed hybrid power system can also be referred to as renewable energy systems.

Distributed generation allows collection of energy from many sources, and has lower environmental impact and improved security of supply. In addition to requiring less long-distance power transmission, local power production reduces waste by lessening dependance on the infrastructure of large power plants and distribution systems. The future power system will consist of several subsystems called distributed power systems (DPS) with both stand-alone and plug-and-produce functionalities, which include the efficient capture of renewable energy sources. A conceptual view of this kind of systems can be shown in Fig. 1.2 [5].

The pollution related to current energy production can be reduced if more renewable power sources, such as wind power, solar power, fuel cells, can be connected to the local power grid. Thus, the system is best described as distributed hybrid power system (DHPS) as it involves the integration of renewable sources with the power distribution grid. A detailed representation of the system is shown in Fig. 1.3, which highlights the final connection of the users and the grid.

When a final user with distributed resources needs to connect to the power grid, a bidirectional power converter is needed. When there is not enough local power, the user can acquire power from the main grid. However, when the local power generating device can provide enough power, the excess power can be stored or even transmitted back to the grid. Thus, bidirectional power converters are essential for the construction of a distributed generation system.

The three-phase alternative current (AC) power is adopted in the existing power system because it is easy to generate and transmit. In the DHPS, a large

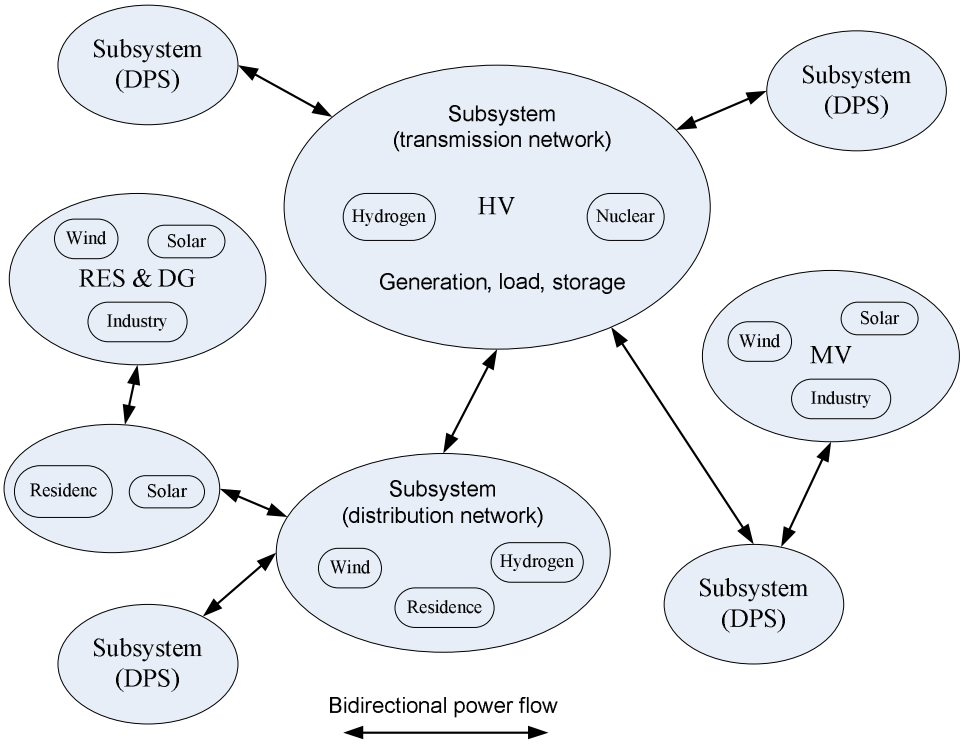

Figure 1.2: General power system based on several subsystems or distributed power systems (DPS).

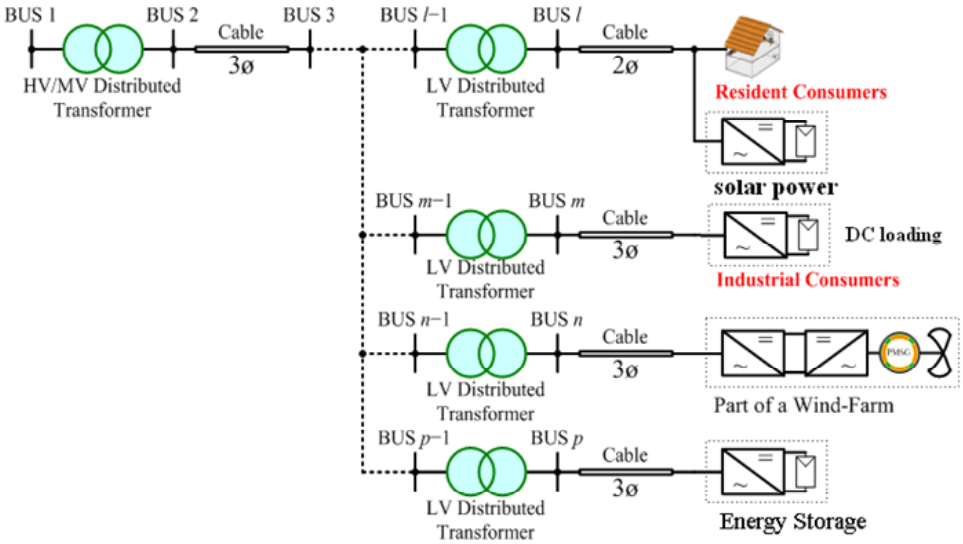

Figure 1.3: Distributed hybrid power system (DHPS).

amount of direct current (DC) devices such as energy storage, solar power, even DC link capacitors in wind power, are included at the user end. As a result, bidirectional three-phase AC-DC converters are needed for this application.

In this study, a widely used three-phase AC-DC converter is chosen as the subject of investigation. The nonlinear behavior of this converter is studied in this thesis, especially under distributed power system environment. The nonlinearity of operation is shown to cause stability problems or oscillations in this system. Our aim is to specify the risk of the undesirable phenomena and provide design guidelines to guarantee operation in a safe region.

1.2 Literature Review

1.2.1 Three-Phase Voltage Source Converters

Traditionally, AC-DC converters, which are also known as rectifiers, are developed using diodes and thyristors to provide controlled and uncontrolled unidirectional and bidirectional DC power. For the bidirectional power flow from the AC utility grid to DC output and vice versa, an ideal converter is normally used. AC-DC converters are widely employed in uninterruptible power supply (UPS) systems, power supplies for telecommunication equipment, HVDC systems, distributed energy sources such as wind energy generation systems, battery energy storage systems, power conversion systems for process technology such as electroplating, welding units, battery charging [6, 7, 8, 9]. Due to its wide usage in power conversion systems and renewable energy systems, the three-phase AC-DC converter has attracted much research attention, which mainly lies in the following aspects.

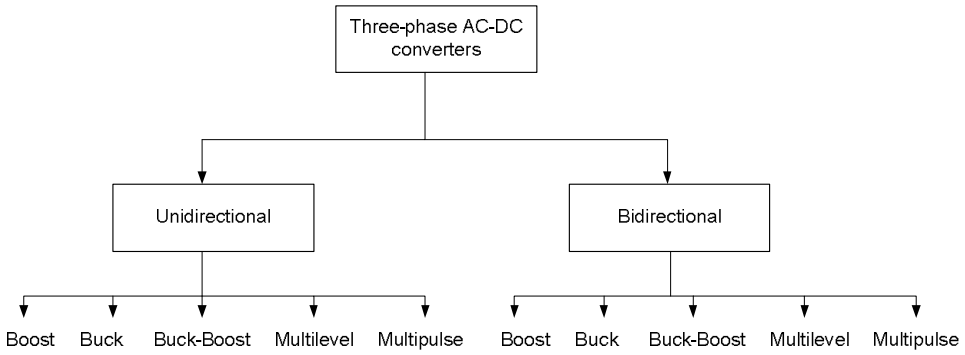

Figure 1.4: Converter-based classification of improved power quality converters.

Topologies

The simplest idea of converting AC power into DC power is to use a diode rectifier [10, 11]. Operating at a low switching frequency (line frequency), they can also be called line-commutated converters. However, the input current and output voltage cannot be controlled. Thus, there are harmonic distortions in the line current and unity power factor (UPF) cannot be achieved. Since high harmonic content cannot be accepted in the power grid, and the reactive power generated by rectifiers would cause power loss through increased conduction loss in the transmission line, new standards have been introduced by governments or organizations to limit the harmonic content and improve power factor of the current drawn from the power line by rectifiers. Consequently, new topologies have been deployed for rectification applications [12, 13, 14, 15, 16, 17].

Thanks to the development of various technologies in the last couple of decades such as power circuit configurations, control strategies, solid-state devices, integrated circuits and magnetics, many practical forms of three-phase power converters have been developed. These converters can be basically categorized into unidirectional and bidirectional power flow. According to different applications, these converters can be further classified into the following categories, as shown in Fig. 1.4 [18].

For the bidirectional power flow from the AC grid to the DC output, an

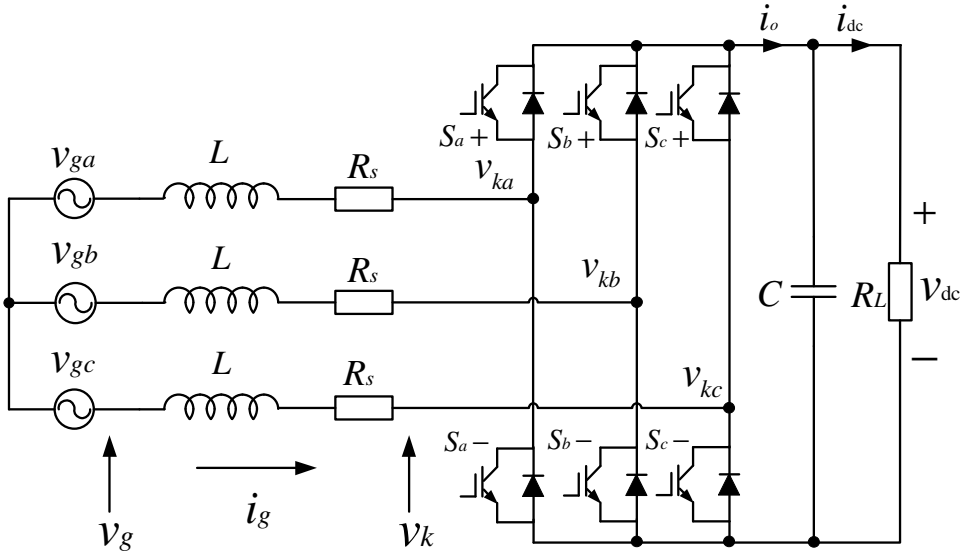

Figure 1.5: Circuit of the three-phase voltage source converter.

ideal converter is normally required in renewable energy generation systems, such as the doubly-fed induction generator (DFIG) in wind power, the charging / discharging converter in electrical vehicles (EV), or line interactive UPSs [19, 20, 21, 22, 23, 24, 25, 26]. Although the buck-boost converters have more flexibility in applications and the multilevel and multipulse converters can further achieve better performance with lower harmonic distortions, they cost too much on devices or require much more complex control strategies. Thus, for general applications, the boost rectifier is still the most popular choice. There are typical applications of boost rectifiers in wind power [9, 27], photovoltaic systems [28], electrical vehicles [29], etc.

The three-phase boost rectifier is also known as the three-phase voltage source converter (VSC), or three-phase power factor correction (PFC) or three-phase pulse-width-modulated (PWM) regenerative rectifier. In this thesis, all these terms are referring to the same power converter circuit shown in Fig. 1.5.

This universal topology has the advantage of using a low-cost three-phase module with a bidirectional energy flow capability. Also, it can provide unity power factor (UPF) [30]. Comparing to the traditional solutions such as thyristor

or chopper, the three-phase voltage source converter reduces the number of power devices and is capable of grid current and power factor control.

Control strategies

Until the 1990s, AC-DC converters had been dominated by uncontrolled rectifiers or line-commutated phase-controlled rectifiers. The forced-commutation concept in three-phase VSCs had been proposed for some time [31], but only since the advent of semiconductor devices and micro-controllers, forced-commutated pulse width modulated (PWM) three-phase VSCs had begun to draw much more attention. Some early works on this topic can be found in the literature, such as the hysteretic current control (HCC) proposed by Ooi *et al.* in 1987 [32]. However, the main drawback of this control is that its average switching frequency varies with the DC load current. Thus, the predictive current control strategy with fixed switching frequency was proposed by Wu *et al.* [33].

The control strategies of the three-phase VSCs can be generally classified into two basic types: indirect current control and direct current control. One of the first type of indirect current control is the phase and amplitude control (PAC) [34, 35], which has a simple structure and provides a good switching pattern. Some emerging ideas include the direct power control (DPC), where no internal current loops or PWM modulator block is needed and the converter switching signals are appropriately determined by a switching table based on the instantaneous errors between the estimated and the actual values of active and reactive power [36]. Without the control for the input current, such control strategies are simple and can be implemented without using current sensors. However, the drawbacks are the slow response of the converter, and some potential safety or stability issues due to the elimination of the current loop [37].

Direct current control has better performance amidst these problems. The initial solution was the previously mentioned hysteresis current control (HCC)

[32], which can also be regarded as an AC current control (CC). The main disadvantage of the HCC is that its average switching frequency f_s varies with the DC load current. To address this issue, a predictive current control strategy with fixed switching frequency (PCFF) was proposed in [33].

However, the most widely used control technique is the voltage oriented control (VOC), which was developed in [38, 39], based on the use of a rotating dq-reference frame model in which the d-axis is aligned to the grid voltage vector. This is a dual method of the field oriented control (FOC) for AC motor drivers, and demonstrates great convenience because the space-vector of the fundamental has constant components in the dq-frame while other harmonics have sinusoidal components. The objective of the converter is to generate or absorb sinusoidal current at the fundamental frequency. Thus, the components of the reference current in the dq-frame are DC quantities. A mathematical model for the three-phase VSC with VOC was proposed in [40]. This model is found useful for practical design. Additionally, the voltage loop and the current loop, which are actually the outer loop and the inner loop, can be considered as being decoupled. This will result in a much simpler control design, which will be further discussed in Section 2.3.

Many other advanced controls have been presented in the literature to achieve optimum performance. In 1999, Kom *et al.* [41] proposed the feedforward current control using a formula to predict the switching space vector so that the current sensor can be eliminated. Also Wang *et al.* [42] introduced a method of active damping for current control to take advantage of the the zero impedance offered by LCL-filter at its resonance frequency.

Modulation techniques

Many AC-DC power converters employ carrier-based PWM methods due to their fixed switching frequency, low ripple current, and well-defined harmonic spectrum

characteristics. The aim of the modulation is to program a "per carrier cycle average output voltage" equal to the reference signal. Employing the triangle-intersection technique [43] or direct digital pulse programming technique [44], carrier-based PWM methods provide a linear relationship between the reference and output voltages within a limited range.

The modulator characteristics determine that there are linear and non-linear regions for the PWM method. In the simple and widely used modulator, which is the sinusoidal PWM (SPWM) [43, 45, 46], the sinusoidal reference waveform (the modulation wave) of each phase and a periodic triangular carrier wave are compared and the intersection points determine the commutation instants of the associated inverter leg switches. However, the portion of the modulation signal having a larger magnitude than the triangular wave peak value remains unmodulated, and the gate signals remain on or off for a full carrier cycle.

Operating in the nonlinear modulation range, or in more common terms, the over-modulation range could be problematic. First, a large amount of subcarrier frequency harmonic currents are generated. Second, the fundamental component voltage gain decreases significantly. Also the switching device gate pulses are abruptly dropped [47].

In the over-modulation region, the voltage gain of the PWM modulator is varying [48, 49], leading to a nonlinear command signal-output voltage relationship [50]. This nonlinearity will also cause saturation in the control loop [51]. Thus, some advanced technologies have been adopted to improve the linear range, such as SVPWM, THIPWM, DPWM [44, 52, 53, 54, 55]. However, these modulation technologies will surely add the complexity in digital processing.

Grid interaction

The above-mentioned works are concerned with stand-alone three-phase VSCs, which means that the power grid is considered as an ideal AC voltage source.

However, in a practical power grid, depending on the grid configuration, a large set of grid impedance exsist, e.g., DHPS is commonly installed in weak grids with long radial distribution feeders [56]. The grid impedance may interact with the converter, and cause stability and harmonic problems, even if the converter has been properly designed. Traditionally, phasor-based models are adopted to analyze the effect of interfacing converters on grid stability below the fundamental frequency [57, 58]. Research efforts have been devoted to the stability issues on the grid interaction [59, 60, 61, 62, 63]. It has been shown that sustained harmonic oscillation and other stability problems emerge due to the presence of high impedance [59], [61]. Research has been conducted using a detailed inverter model to analyze the grid interaction and the effect of coupling with other grid-connected converters [64, 50, 65, 66].

However, a set of impedance ratio criteria was developed by Middlebrook in 1976 [67]. It was proposed for input filter design of various of power converters, and proved to be a very effective method for stability design of the converter with input filter [68, 69, 70, 71, 72, 73]. Then this set of criteria was extended to the series connected converters or small systems with power source and load [74, 75, 76, 77, 78, 79, 80, 81]. Recently, due to the concern of system stability of distributed power grids, a generalized impedance-based criterion was used to study stability and power quality issues in AC distributed systems [62, 59].

An unbalanced three-phase grid may cause even harmonics at the DC output and the input current [82]. Some solutions were studied such as the use of negative sequence in the reference current [83] which may lead to uncontrollability of the power factor unfortunately, or, the use of two current controllers for positive and negative sequences [84] which also created stability problems. Recent work has extended the small-signal stability analysis method to three-phase unbalanced systems [62], which may help solve the unbalanced problem from the impedance analysis point of view.

1.2.2 Bifurcation Analysis

Nonlinearity widely exists in power electronic circuits. Active research on this topic began from the late 1980s. In 1988, Hamill and Jefferies [85] first reported the analysis of chaos and bifurcation dynamics in DC-DC converters. Then in 1989, Deane and Hamill [86, 87] examined the first order and second order voltage-mode controlled buck converters. With the input voltage serving as a bifurcation parameter, the converter was shown to bifurcate from stable operation to subharmonic oscillations, then to chaos. Chaos was shown by determining boundary conditions on circuit differential equations, by SPICE simulations and by experiments. In 1990, Krein and Bass [88] observed the unboundedness, chattering, and chaos in simple power electronic circuits experimentally.

In 1994, period-doubling cascades were demonstrated by Tse [89] in a simple boost converter operating in discontinuous mode. This work attempted to model the boost converter, when operating in discontinuous mode, as a first-order iterative map, and to analytically locate the onset of period-doubling bifurcation. Formal theoretical study of the conditions for possible occurrence of period-doubling cascades in the discontinuous mode DC-DC converter was reported in 1997 by Chan and Tse [90]. In 1999, El Aroudi *et al.* [91] also found that Hopf bifurcation can occur at a certain value of the parameters when the pulse width modulation (PWM) period is varied.

Much of the early work had focussed on voltage-mode controlled DC-DC converters. In fact, the current-mode control is very widely used in boost or buck-boost DC-DC converters. The chaotic behavior was first reported in current-model boost converter by Deane [92]. Chan and Tse [90, 93] studied various routes to chaos and their dependance upon the choice of bifurcation parameters. Similar study in the boost converter was reported by Banerjee who summarized much of the previous work in [94].

Furthermore, the chaotic and bifurcation phenomena in paralleling converters were studied. Iu and Tse [95, 96] reported the instability and bifurcation phenomena in parallel-connected buck converters. Then in parallel-connected buck converters, a low-frequency bifurcation phenomenon was found by them in 2003 [97]. Furthermore, Huang *et al.* [98] found that, for parallel-connected buck converters, the system exhibits either a slow-scale bifurcation (Neimark-Sacker bifurcation) or a fast-scale bifurcation (period-doubling), depending on the value of the integral time constant. This kind of coexisting fast-scale and slow-scale bifurcation is found to be a general phenomenon, which is also identified in current-mode controlled DC-DC converters in 2008 by Chen *et al.* [99].

For the single-phase power factor correction (PFC) circuit, Orabi and Ninomiya [100] found that period-doubling oscillation occurs when the load varies from 100% to 15%, or when the output capacitor varies. The nonlinear phenomenon was analyzed by the method of double averaging by Wong *et al.* in 2006 [101]. Then in 2009, Chu *et al.* [102] extended the previous work to a two-stage boost PFC with a downstream DC-DC converter.

In 2003, Süto and Nagy [103] provided some preliminary analysis and simulation results of bifurcation phenomena in three-phase converter systems. Also in 2004, Gao and Chau studied the synchronous reluctance motor drives based on a PID control for speed error regulation, and analyzed Hopf bifurcation and chaos in the system [104]. For a three-phase power system, some initial findings were discussed by Wang [64] and Belkhayat [66].

Bifurcation control is another important topic, which refers to the task of designing a controller that can modify the bifurcating properties of a given system, so as to achieve some desirable dynamical behavior [105]. In 1995, Poddar *et al.* [106] attempted to control chaos in DC-DC converters by identifying the unstable fixed points in every cycle.

1.3 Objectives of the Thesis

Power electronics systems are nonlinear dynamical systems. Current design of power electronics systems is based on linear analysis, and the results are often not satisfactory for some practical conditions. Research on the nonlinear behavior of power converters therefore has significant practical values. In the distributed hybrid power systems, grid-connected power converters are working in a new application environment where the connecting power grid is non-ideal and some other interacting loads may be connected to the point of common coupling (PCC). In such systems, complex bifurcation phenomena may occur under variation of a large number of parameters. Our aims in this thesis are to perform bifurcation analysis to identify these phenomena, and to describe a design-oriented analysis to identify regions in practical parameter space where the system operates in specific operating regimes including stable operation and other possible dynamical behaviors.

1.4 Organization of the Thesis

The thesis is arranged in the following order.

The circuit configuration of the three-phase voltage source converter (VSC) and the mathematical model used for control design are reviewed in Chapter 2. The saturation of the output under the application of the usual modulation techniques is also described. In particular, the expressions of the SPWM output in the linear operation region and the over-modulation region are derived.

Then, the bifurcation and instability phenomena in this converter are identified and analyzed in Chapters 3 to 5.

Specifically, in Chapter 3, the nonlinear operation of a stand-alone three-phase VSC is modeled and analyzed. This nonlinear operation is due to the varying

series resistance of the line reactor and the saturation characteristic of the PWM module. Due to this nonlinearity, the VSC exhibits a catastrophic bifurcation and enters an abnormal operation region.

In Chapter 4, the non-ideal grid conditions are taken into consideration. In addition, some loads may be connected to the power grid at the point of common coupling (PCC). Meanwhile the grid impedance can be different, depending on the grid structure and the location where the converter is connected. With the grid impedance and interacting loads varying unpredictably, an irreversible bifurcation phenomenon has been identified.

In Chapter 5, the effects of grid impedance are studied in some depth. Because the grid impedance is high in a weak grid, which is common in distributed generation systems, the impact of grid impedance on the control design of the three-phase VSC will be discussed in this chapter. A low-frequency oscillation, which can also be regarded as a Hopf bifurcation, is identified. Furthermore, the interaction of the two previously found bifurcation phenomena is studied. In the low-frequency Hopf bifurcation, the expanded limit cycle pushes the VSC closer to the stability boundary of the catastrophic bifurcation, which is highly undesirable for practical purposes. It is shown that the stability margin is affected by variation of grid and converter parameters.

Finally, the thesis concludes in Chapter 6 and some suggestions for future research are also proposed.

Chapter 2

Overview of Three-Phase Voltage Source Converters

Three-phase voltage source converters (VSCs) are designed to provide constant DC bus voltage, with low input harmonic current distortion and a fully controllable power factor. They serve as the essential interface for many power conversion systems with the AC mains. The basic circuit design, modeling and control strategy will be discussed in this chapter. We will focus on the VSC working in the rectifier mode, commonly known as the three-phase boost rectifier. In the rest of this thesis, the terms "three-phase voltage source converter (VSC)", "three-phase boost rectifier", "three-phase power factor correction (PFC) power supply", all refer to the same topology shown in Fig. 2.1.

2.1 Steady-State Operation

Figure 2.1 shows a common three-phase voltage source converter. It can be divided into four parts. The ideal power grid is represented by an AC voltage source. The other parts include a line reactor, which is essentially an inductor, a rectifying bridge with a DC link capacitor, and a DC load connected to the DC

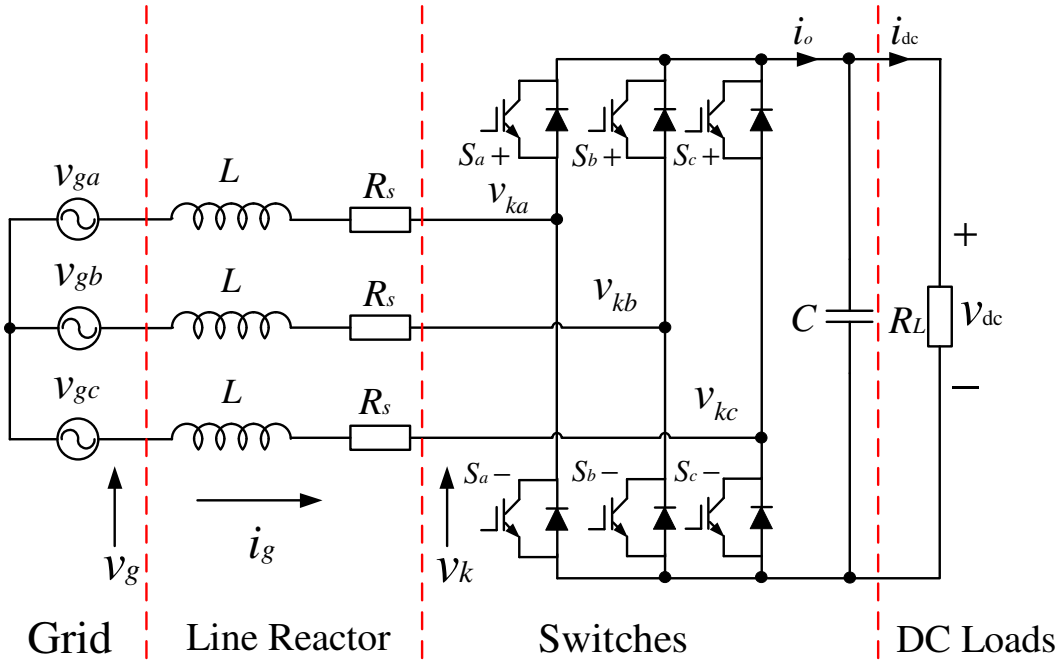

Figure 2.1: Circuit of the three-phase voltage source converter.

side.

For a balanced three-phase system, we can represent this system by a single-phase equivalent circuit, as shown in Fig. 2.2. The voltage source v_{ka} represents the output voltage generated by the six-switch bridge. The line current i_{ga} is determined by the voltage across the inductance L and R_s interconnecting the two voltage sources. When we control the phase angle ϕ and the amplitude of converter voltage v_{kx} $(x = a, b, c)$, we control indirectly the phase and amplitude

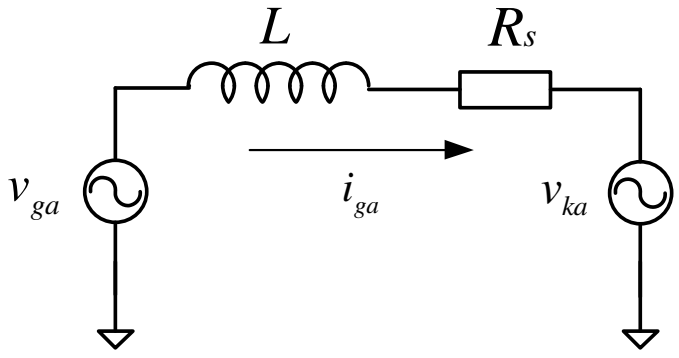

Figure 2.2: Single-phase equivalent circuit for the three-phase voltage source converter.

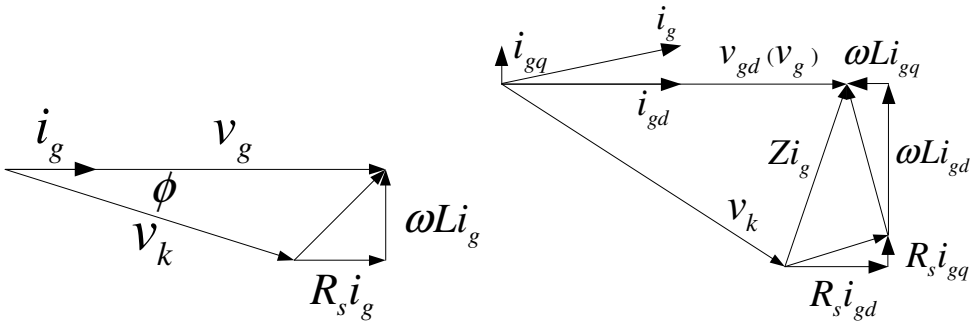

(a) (b)

Figure 2.3: Phasor diagram of a three-phase voltage source converter. (a) The converter works with unity power factor (PF = 1); v_g and i_g are in phase. (b) The converter works with non-unity power factor (PF < 1).

of the line current, as depicted by the phasor diagram shown in Fig. 2.3.

The inductors connecting the grid and switches not only act as input filters, but also provide a current source characteristic of the input circuit and step-up (boost) function of the converter.

2.2 Mathematical Model

For a balanced three-phase system, the three-phase grid voltage and current can be expressed as [107]

$$v_{ga} = V_g \cos(\omega t + \theta(0)) \tag{2.1}$$

$$v_{gb} = V_g \cos(\omega t + \theta(0) - 2\pi/3) \tag{2.2}$$

$$v_{gc} = V_g \cos(\omega t + \theta(0) + 2\pi/3), \tag{2.3}$$

and

$$i_{ga} = I_g \cos(\omega t + \theta(0) + \Delta\theta) \tag{2.4}$$

$$i_{gb} = I_g \cos(\omega t + \theta(0) + \Delta\theta - 2\pi/3) \tag{2.5}$$

$$i_{gc} = I_g \cos(\omega t + \theta(0) + \Delta\theta + 2\pi/3), \tag{2.6}$$

where $\theta(0)$ is the initial phase angle of the system, and $\Delta\theta$ is the phase angle difference between voltage vector and current vector. Obviously, if the converter works in unity power factor (UPF), we will have $\Delta\theta = 0$. Since there is no neutral connection, we obtain

$$i_{ga} + i_{gb} + i_{gc} = 0. \tag{2.7}$$

2.2.1 Converter *abc*-Model

The three-phase VSC can be described by four state equations, one for the voltage of each phase and one for the current on the DC side [40], i.e.,

$$L\frac{di_{ga}}{dt} = -R_s i_{ga} + v_{ga} - v_{ka} \tag{2.8}$$

$$L\frac{di_{gb}}{dt} = -R_s i_{gb} + v_{gb} - v_{kb} \tag{2.9}$$

$$L\frac{di_{gc}}{dt} = -R_s i_{gc} + v_{gc} - v_{kc} \tag{2.10}$$

$$C\frac{dv_{dc}}{dt} = i_{ga}S_a + i_{gb}S_b + i_{gc}S_c - i_{dc}, \tag{2.11}$$

where $S_x(x = a, b, c)$ is the switching function, which can be naturally defined as

$$S_x = \begin{cases} 1 & \text{if upper switch is on} \\ 0 & \text{if upper switch is off} \end{cases} \tag{2.12}$$

The output voltage of the six-switch bridge v_k can also be expressed in terms

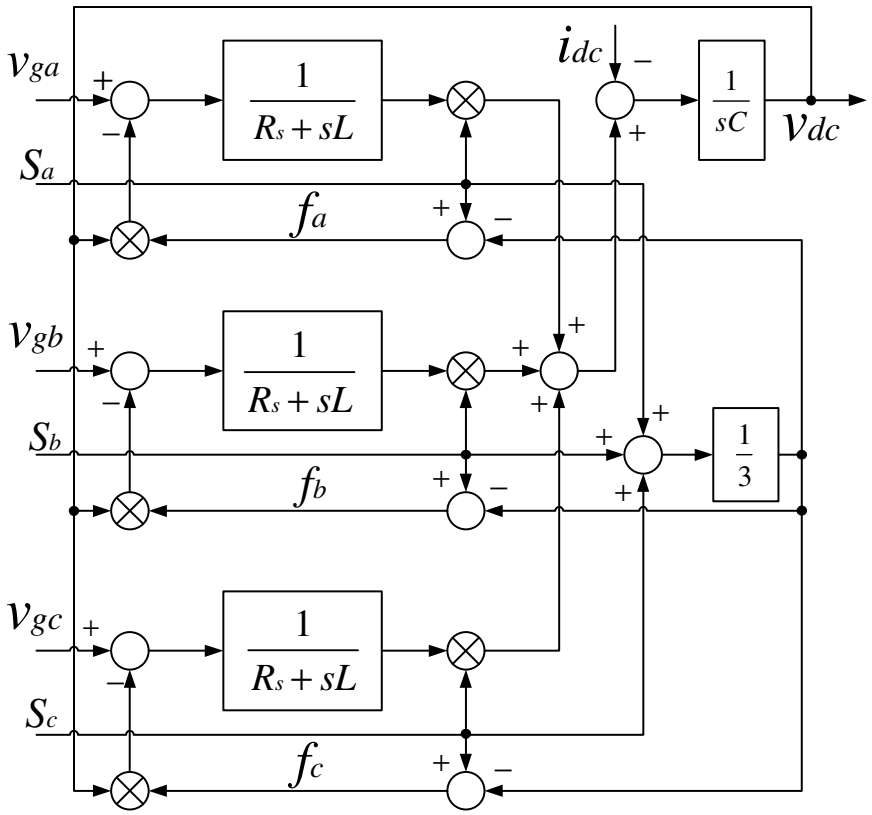

Figure 2.4: The *abc*-model of the three-phase voltage source converter.

of the switching functions.

$$v_{ka} = f_a v_{dc} = (S_a - \frac{S_a + S_b + S_c}{3}) v_{dc} \tag{2.13}$$

$$v_{kb} = f_b v_{dc} = (S_b - \frac{S_a + S_b + S_c}{3}) v_{dc} \tag{2.14}$$

$$v_{kc} = f_c v_{dc} = (S_c - \frac{S_a + S_b + S_c}{3}) v_{dc}. \tag{2.15}$$

A block diagram representation of this three-phase *abc*-model is shown in Fig. 2.4.

2.2.2 Converter $\alpha\beta$-Model

We define the amplitude invariant Clarke transformation as

$$T_{\alpha\beta} = \frac{2}{3}\begin{bmatrix} 1 & -\frac{1}{2} & -\frac{1}{2} \\ 0 & \frac{\sqrt{3}}{2} & -\frac{\sqrt{3}}{2} \end{bmatrix}. \tag{2.16}$$

Then, the grid voltage vector v_g in the three-dimensional stationary reference frame can be transformed into a two-dimensional stationary reference frame by applying the matrix on the three-dimensional vector v_g, which is

$$v_{g\alpha\beta} = T_{\alpha\beta} \cdot v_g \tag{2.17}$$

Thus, the *abc*-model described by (2.11) is transformed to

$$L\frac{di_{g\alpha}}{dt} = -R_s i_{g\alpha} + v_{g\alpha} - v_{k\alpha} \tag{2.18}$$

$$L\frac{di_{g\beta}}{dt} = -R_s i_{g\beta} + v_{g\beta} - v_{k\beta} \tag{2.19}$$

$$C\frac{dv_{dc}}{dt} = \frac{3}{2}(i_{g\alpha}S_\alpha + i_{g\beta}S_\beta) - i_{dc}. \tag{2.20}$$

The complex vector in the two-dimensional stationary reference frame $v_{g\alpha\beta}$ is also rotating counterclockwise, which is same as that in the three-dimensional stationary reference frame.

2.2.3 Converter dq-Model

Applying the Park transformation to the stationary reference frame $\alpha\beta$-model, the transfer matrix is given as

$$T_{dq} = \begin{bmatrix} \cos\theta_v & \sin\theta_v \\ -\sin\theta_v & \cos\theta_v \end{bmatrix}. \tag{2.21}$$

In this transformation, the transfer matrix is time varying, i.e.,

$$\theta_v = \omega t + \theta(0). \tag{2.22}$$

The two-dimensional stationary reference frame grid voltage vector $v_{g\alpha\beta}$ is further transformed to the two-dimensional synchronous reference frame, i.e.,

$$v_{gdq} = T_{dq} \cdot v_{g\alpha\beta}. \tag{2.23}$$

Finally, the expression of the grid voltage can be written as

$$v_{gdq} = T_{dq} \cdot T_{\alpha\beta} \cdot v_g \tag{2.24}$$

$$= T_{dq} \cdot T_{\alpha\beta} \cdot V_g \begin{bmatrix} \cos(\omega t + \theta(0)) \\ \cos(\omega t + \theta(0) - 2\pi/3) \\ \cos(\omega t + \theta(0) + 2\pi/3) \end{bmatrix} \tag{2.25}$$

$$= V_g \begin{bmatrix} \cos(\omega t + \theta(0) - \theta_v) \\ \sin(\omega t + \theta(0) - \theta_v) \end{bmatrix}. \tag{2.26}$$

From (2.22), we only need to make sure that θ_v could follow the grid phase angle $\omega t + \theta(0)$, which can be detected and calculated from the three-phase grid voltage. Hence, it can be easily found that the elements of the complex vector in two-dimensional synchronous reference frame v_{gdq} only have two constant values, since $\cos 0 = 1$ and $\sin 0 = 0$.

In particular, it should be noted that all the three-phase elements, such as grid current i_g, output voltage of bridge v_k, and passive elements L, R_s, should be transformed into the dq-model under the two-dimensional synchronous reference frame. Fortunately, the passive elements can stay the same form as they are under the three-dimensional stationary reference frame.

Obviously, there are a lot of benefits of using this transformation. Firstly, the three-dimensional signals or elements are transformed to two-dimensional signals or elements, which means that it is much simpler to process the parameters. Secondly, the sinusoidal signals are transformed to constant values, for example, the grid voltage which is shown in (2.26). Thus, it is more convenient for the control design.

However, there are cross-coupling items coming out from this transformation, which can be shown as follows.

$$L\frac{d}{dt}(T_{dq}\cdot\begin{bmatrix} i_{g\alpha} \\ i_{g\beta} \end{bmatrix}) = -R_s(T_{dq}\cdot\begin{bmatrix} i_{g\alpha} \\ i_{g\beta} \end{bmatrix}) + T_{dq}\cdot\begin{bmatrix} v_{g\alpha} \\ v_{g\beta} \end{bmatrix} - T_{dq}\cdot\begin{bmatrix} v_{k\alpha} \\ v_{k\beta} \end{bmatrix} \tag{2.27}$$

$$LT_{dq}\cdot\frac{d}{dt}\begin{bmatrix} i_{g\alpha} \\ i_{g\beta} \end{bmatrix} + L(\frac{d}{dt}T_{dq})\begin{bmatrix} i_{g\alpha} \\ i_{g\beta} \end{bmatrix} = -R_s\begin{bmatrix} i_{gd} \\ i_{gq} \end{bmatrix} + \begin{bmatrix} v_{gd} \\ v_{gq} \end{bmatrix} - \begin{bmatrix} v_{kd} \\ v_{kq} \end{bmatrix} \tag{2.28}$$

$$L\frac{d}{dt}\begin{bmatrix} i_{gd} \\ i_{gq} \end{bmatrix} + L\begin{bmatrix} 0 & \omega \\ -\omega & 0 \end{bmatrix}\begin{bmatrix} i_{gd} \\ i_{gq} \end{bmatrix} = -R_s\begin{bmatrix} i_{gd} \\ i_{gq} \end{bmatrix} + \begin{bmatrix} v_{gd} \\ v_{gq} \end{bmatrix} - \begin{bmatrix} v_{kd} \\ v_{kq} \end{bmatrix} \tag{2.29}$$

Using the above transformation, the entire model of the three-phase voltage source converter can be written in the dq-transformation as follows

$$L\frac{di_{gd}}{dt} = \omega L i_{gq} - R_s i_{gd} + v_{gd} - v_{kd} \tag{2.30}$$

$$L\frac{di_{gq}}{dt} = -\omega L i_{gd} - R_s i_{gq} + v_{gq} - v_{kq} \tag{2.31}$$

$$C\frac{dv_{dc}}{dt} = \frac{3}{2}(S_d i_{gd} + S_q i_{gq}) - i_{dc}. \tag{2.32}$$

A block diagram of this two-dimensional dq-model (2.32) in synchronous reference frame is shown in Fig. 2.5. It should be noticed that the cross-coupling exists

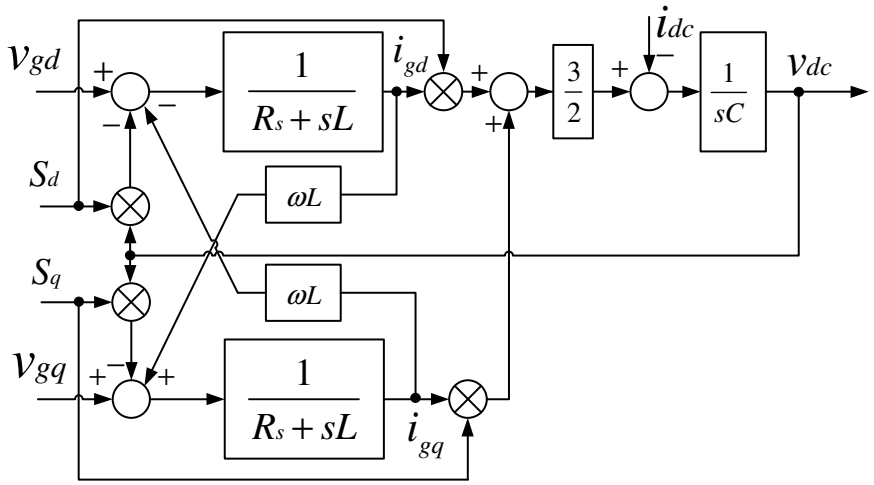

Figure 2.5: The dq-model of the three-phase voltage source converter.

due to the rotating feature, as denoted by ωL in Fig. 2.5. However, by inserting $\omega = 0$, this diagram can be degenerated to $\alpha\beta$-model in the two-dimensional stationary reference frame. The cross-coupling should be compensated when designing the control strategy to achieve a decoupled control.

2.3 Control Design

2.3.1 Current Regulator

As mentioned in Section 1.2.1, the vector oriented control (VOC) is widely used in the three-phase voltage source converter, due to the features of fixed switching frequency and fine current tracking capability of the inner current loop.

First of all, the cross-coupling should be compensated in the control as mentioned in Section 2.2. Then, the current control regulator can be reduced to a first-order delay, by decoupling the d and q axes. In this control, the block named "ωL" is applied to compensate the inductive cross-coupling of the circuit.

Using the above compensation technique, the current loop is simplified as the block diagram shown in Fig. 2.7. Since the same control applies to both d and q axis regulators, subscripts d and q are omitted here. The parameters are defined

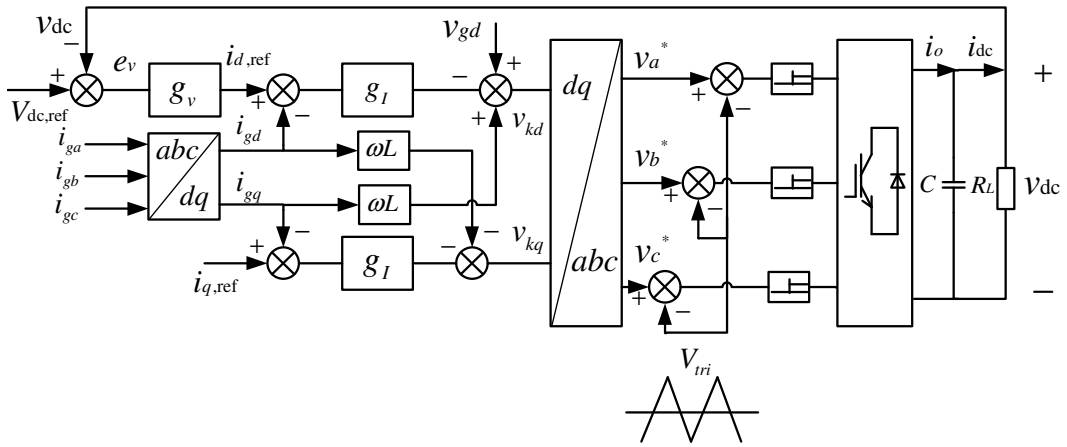

Figure 2.6: Control block diagram of the three-phase voltage source converter.

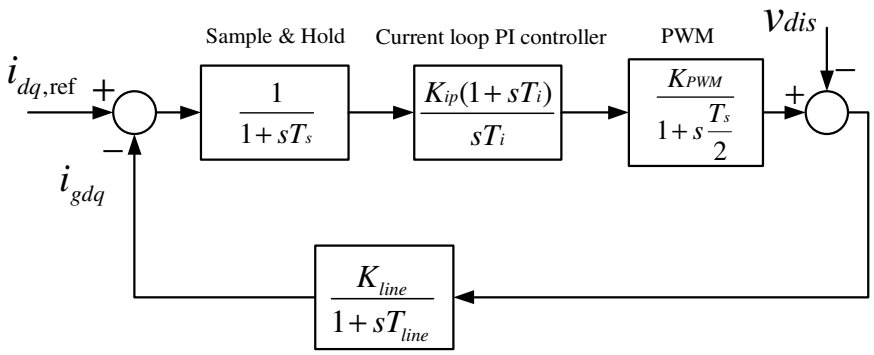

Figure 2.7: Block diagram of the inner current loop.

as follows.

T_s	sampling time
K_{ip}	DC gain of current loop PI controller
T_i	time constant of current loop PI controller
K_{PWM}	gain of PWM module
K_{line}	gain of line reactor
T_{line}	time constant of line reactor

The power unit has a time constant which is one half of the sampling period T_s [40]. To further simplify the block diagram shown in Fig. 2.7, the two blocks with smallest time constants (sample & hold and PWM) are merged together to

form a single block with equivalent time constant T_{ei}, which is given by

$$T_{ei} \approx T_s + \frac{T_s}{2} = 1.5T_s. \tag{2.33}$$

The dominant pole in the load can be canceled by setting the internal time of the PI controller equal to that of the load

$$T_i = T_{line} \tag{2.34}$$

With the simplification of (2.33) and the time constant selection of (2.34), the closed-loop transfer function of the system in Fig. 2.7 can be written as

$$H_{ci} = \frac{1}{1 + \frac{sT_{line}}{K_i K_{PWM} K_{line}} + \frac{s^2 T_{line} T_{ei}}{K_{ip} K_{PWM} K_{line}}}. \tag{2.35}$$

It is a typical second-order system, and the damping factor is given by

$$\zeta^2 = \frac{T_{line}}{4K_{ip} T_{ei} K_{PWM} K_{line}} = \frac{1}{2} \tag{2.36}$$

The closed-loop transfer function (2.35) can be further simplified by neglecting the s^2 term. The first-order approximation is obtained as

$$H_{ci} = \frac{i_{gdq}}{i_{dq,\text{ref}}} = \frac{1}{1 + sT_{et}}. \tag{2.37}$$

where $T_{et} = 4T_{ei}\zeta^2$. The closed-loop system can be optimized to a critically damped system, which means $\zeta = \sqrt{2}/2$. Thus, we can design the proportional gain K_{ip} from the above information.

2.3.2 DC Bus Voltage Regulator

The DC bus voltage regulator can be modeled as Fig. 2.8. The current loop is

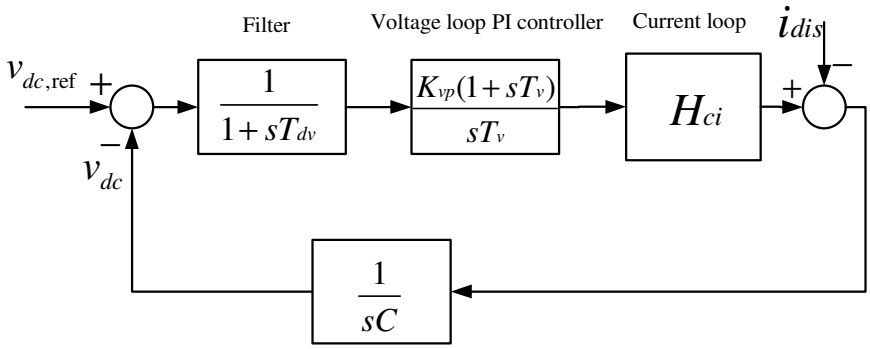

Figure 2.8: Block diagram of the outer voltage loop.

represented by a simple block H_{ci} in this diagram, a T_v is the time constant of the PI controller. The parameters are defined as follows.

T_{dv}	feedback-loop delay due to sampling, processing time and filter
K_{vp}	DC gain of voltage loop PI controller
T_v	time constant of voltage loop PI controller

Same as the analysis of the current loop, the equivalent time constant T_{ev} can be obtained by combining the two smallest time constants in the block diagram of Fig. 2.8, i.e.,

$$T_{ev} = T_{dv} + 2T_{ei}. \tag{2.38}$$

The open-loop transfer function is thus given by

$$H_{ov} = \frac{K_{vp}(1 + sT_v)}{sT_v(1 + sT_{ev})sC}. \tag{2.39}$$

The system response can be designed as a Type-II system [108].

2.4 Modulation Technique

In the most straightforward implementation, generation of the desired output voltage is achieved by comparing the desired reference waveform (command sig-

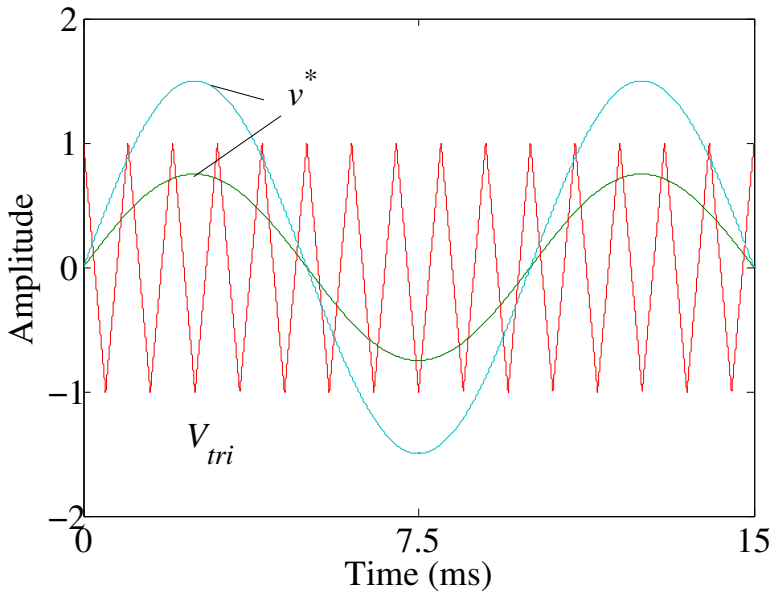

Figure 2.9: The command signal v^* is intersecting with the triangle wave V_{tri}.

nal) with a high-frequency triangular carrier wave.

The most widely used modulator is the sinusoidal PWM (SPWM). In this method, the sinusoidal reference waveform (the modulation wave) of each phase and a periodic triangular carrier wave are compared and the intersection points determine the commutation instants of the associated inverter leg switches. In the three-phase voltage source converter shown in Fig. 2.1, associated with SPWM method shown in Fig. 2.9, the fundamental component $\hat{v}_k$ at line frequency f of phase voltage v_{kx} (with $x = a, b, c$) is generated from the pulse-width-modulated output capacitor voltage v_{dc} using switch-pair S_x+ and S_x-.

The control signal of the switch pair are generated from comparison of v^* $(= v_a^*, v_b^*, v_c^*)$ with fixed frequency f_s and constant-magnitude triangular wave V_{tri}. The modulation index can be defined as the ratio of the peak value of the command signal and the carrier wave, i.e.,

$$m = \frac{v^*}{V_{tri,\text{peak}}}. \tag{2.40}$$

For $m \leq 1$, the relationship between $\hat{v}_k$ and v^* (or m) can be considered linear, i.e.,

$$\hat{v}_k = \frac{v_{\mathrm{dc}}}{2} m. \tag{2.41}$$

However, the portion of the modulation signal having a larger magnitude than the triangular wave peak value remains unmodulated, and the gate signals remain on or off for a full carrier cycle. This will lead to a nonlinear reference output-voltage relationship.

In the triangle intersection technique, when the modulation wave magnitude becomes larger than the peak of the triangular wave, switching during that carrier cycle ceases, and the corresponding switch remains locked to the inverter pole within the carrier cycle. This condition is defined as the "saturation" of the particular phase. Though not commonly utilized, the terms "unmodulated phase" will be frequently utilized to indicate that the modulation signal of the corresponding phase becomes larger than the triangular carrier wave and modulation ceases. At the beginning of the over-modulation region, depending on the modulator type, one or two of the three modulation waves are simultaneously saturated. As the modulation index increases, the saturated segments of each modulation wave and the number of simultaneously saturated phases increase according to the waveform characteristic of each modulator until the six-step operating mode is reached [109].

In the over-modulation region, the output of the modulation module is saturated. For a general case, a typical input-output characteristic curve for the saturation nonlinearity can be described as

$$v_k(\omega t) = v_k(\theta) = \begin{cases} \hat{v}_k^* \sin\theta; & 0 < \theta < a \\ \frac{V_{\mathrm{dc}}}{2}; & a < \theta < \frac{\pi}{2}, \end{cases} \tag{2.42}$$

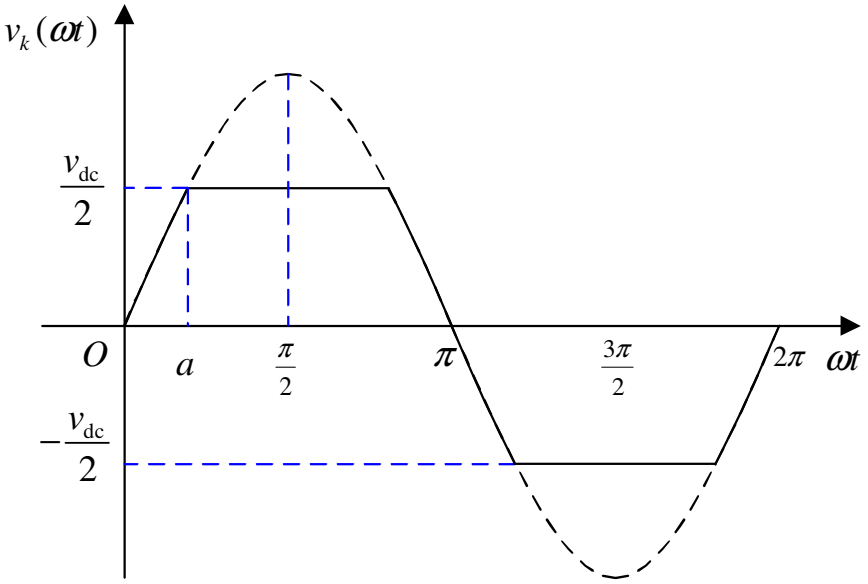

Figure 2.10: The output of the switch bridge when working in over-modulation region.

where $\hat{v}_k^*$ is the peak value of the input command signal, and $\theta = \omega t$.

Since the output $v_k(\theta)$ is an odd function, its Fourier series expansion has only sine terms. The fundamental harmonic component of the output of $v_k(\theta)$ can be given by

$$v_k(\theta) = V_{k1} \sin\theta, \tag{2.43}$$

where

$$\begin{aligned} V_{k1} &= \frac{1}{\pi}\int_0^{2\pi} v_k(\theta)\sin\theta d(\theta) \\ &= \frac{4}{\pi}\int_0^{\pi/2} v_k(\theta)\sin\theta d\theta \ ; (\text{quarter wave symmetry}) \\ &= \frac{4}{\pi}(\int_0^{a} \hat{v}_k^* \sin^2\theta d\theta + \int_a^{\pi/2} \frac{v_{dc}}{2}\sin\theta d\theta) \\ &= \frac{4}{\pi}\hat{v}_k^* \int_0^{a} \frac{1}{2}(1-\cos 2\theta)d\theta + \frac{4}{\pi}\frac{v_{dc}}{2}\int_a^{\pi/2}\sin\theta d\theta. \end{aligned} \tag{2.44}$$

Specifically, when the output gets saturated, the output voltage reaches the

maximum value, i.e., $\hat{v}_k^* \sin a = \frac{v_{\rm dc}}{2}$. Then, (2.44) can be further simplified as

$$\begin{aligned} V_{k1} &= \frac{4}{\pi}\hat{v}_k^* \frac{1}{2}(a - \frac{1}{2}\sin 2a) + \frac{4}{\pi}\hat{v}_k^* \sin a \cos a \\ &= \frac{\hat{v}_k^*}{\pi}(2a + \sin 2a) \end{aligned} \tag{2.45}$$

Following the previous definition, $a = \sin^{-1} \frac{\frac{v_{\rm dc}}{2}}{\hat{v}_k^*} = \sin^{-1} \frac{1}{m}$, and (2.45) can be written as

$$\begin{aligned} V_{k1} &= \frac{\hat{v}_k^*}{\pi}(2\sin^{-1}\frac{1}{m} + 2\frac{1}{m}\cos a) \\ &= \frac{\hat{v}_k^*}{\pi}(2\sin^{-1}\frac{1}{m} + 2\frac{1}{m}\sqrt{1-(\frac{1}{m})^2}) \\ &= \frac{v_{\rm dc}}{\pi}(m\sin^{-1}\frac{1}{m} + \sqrt{1-(\frac{1}{m})^2}). \end{aligned} \tag{2.46}$$

Thus, the output voltage of the modulated signal is

$$v_k(\omega t) = V_{k1}\sin\omega t. \tag{2.47}$$

The peak value of the output voltage when modulated in the over-modulation region is V_{k1}, which can be written as

$$\hat{v}_k = \frac{v_{\rm dc}}{\pi}(m\sin^{-1}\frac{1}{m} + \sqrt{1-(\frac{1}{m})^2}). \tag{2.48}$$

The expression of $\hat{v}_k$ is summarized as

$$\hat{v}_k = \begin{cases} \frac{v_{\rm dc}}{2} m \ ; m \le 1 \\ \frac{v_{\rm dc}}{\pi}(m\sin^{-1}\frac{1}{m} + \sqrt{1-(\frac{1}{m})^2}) \ ; m > 1 \end{cases} \tag{2.49}$$

When $m \le 1$, the relationship between $\hat{v}_k$ and m is linear. However, when $m > 1$, the relationship is nonlinear and will be saturated at $\frac{2v_{\rm dc}}{\pi}$, as shown in Fig. 2.11.

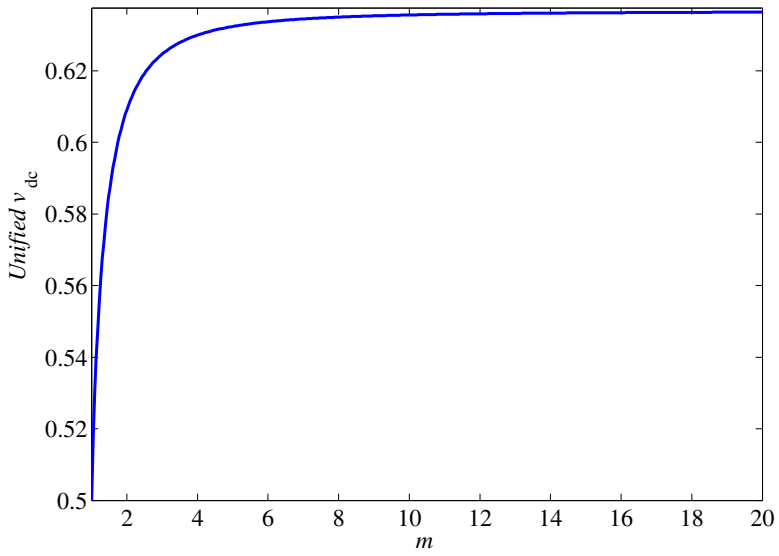

Figure 2.11: The output of the switch bridge becomes saturated when modulation index increases.

If the modulation index keeps increasing, the output of the switching bridge $\hat{v}_k$ will saturate, and the switching pattern will reach the six-step mode operation, which can be seen in [109] and Section 4.1.

2.5 Summary

In this chapter, we have briefly reviewed the basics of three-phase voltage source converters. The steady-state operation is described, and a simple mathematical model is introduced. Using Park and Clarke transformations, the model is transformed from a three-phase stationary reference frame *abc*-model to a two-phase synchronous reference frame *dq*-model, which can be readily controlled by a decoupled dual loop control strategy. The control design has also been discussed in this chapter. In particular, the pulse-width modulation technique is reviewed here. The saturation nonlinearity is explained when the converter is working in the over-modulation region.

Chapter 3

Catastrophic Bifurcation

We first consider the three-phase voltage source converter connected to an ideal power grid. The common control which has been discussed in Chapter 2 is implemented by a proportional-integral (PI) scheme. Although much research work has been developed for better regulation of the output voltage [110, 111, 112, 113], the main focus of previous works has been on the operation and control of the voltage source converter within a relatively small range of operating conditions. Such linear techniques obviously fall short of predicting large-signal transient stability. In particular, due to output voltage disturbances, such as those produced by capacitive loads, the inner current loop can be easily driven into over-modulation and possible six-step operation mode.

We will start from the situation of an additional load connected to the DC side of the voltage source converter. A catastrophic bifurcation is identified for the three-phase voltage source converter. When this bifurcation occurs, the DC output of the converter will collapse, and the input line current will expand to a very high level, which is dangerous for the grid. A set of design-oriented parameter boundaries are given. Also, the cause of this special bifurcation is identified by analyzing the nonlinear operation of the converter circuit. This phenomenon is finally observed in experiments, which will also be shown in this chapter.

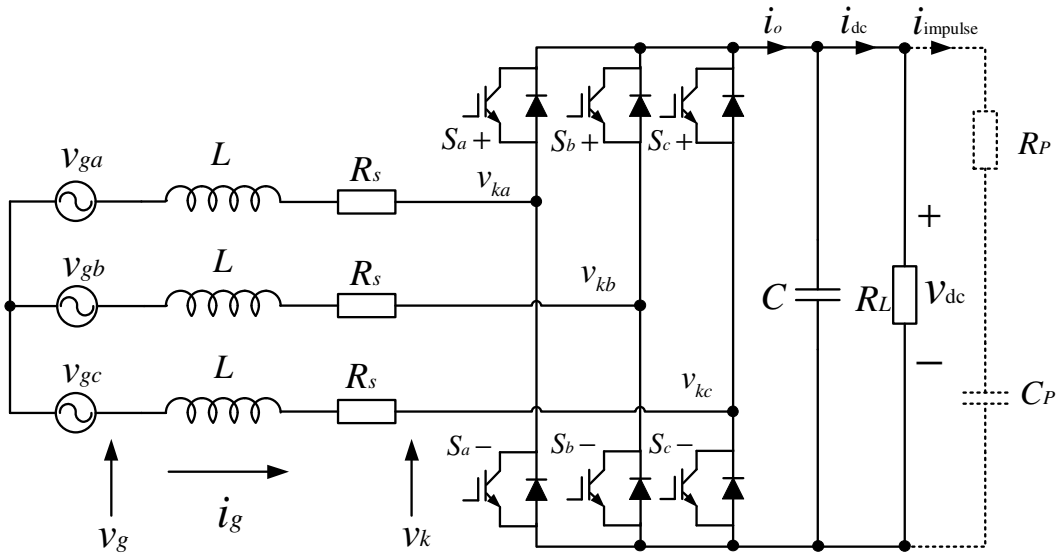

Figure 3.1: Three-phase voltage source converter.

3.1 A Glimpse at Catastrophic Bifurcation

The circuit of Fig. 3.1 and the associated control of Fig. 3.2 are implemented using MatLab. The circuit components used in the simulation are shown in Table 3.1. A three-phase utility of 110 Vrms, which is available in North America, is used for illustration of the phenomenon. In practice, the rectifier circuit can provide a regulated voltage of 360 V at a rated output power of 4 kW for a load of $R_L = 32\ \Omega$.

The switches are implemented with three CM150DY-24H dual IGBT modules to make sure that the rectifier can survive after the catastrophic bifurcation. Equivalent resistance values of R_s ranging from 0.1 Ω to 1 Ω are used to model the possible range of loss associated with device, conductor resistance and switching losses of the converter circuit. The efficiencies of the rectifier at $R_L = 110\,\Omega$ using $R_s = 0.1\,\Omega$ and 1 Ω are 92.3% and 89.3%, respectively, which are comparable to that of similar hard-switching three-phase rectifier circuits (typically around 90%) [114].

Figure 3.3 shows the transient waveforms of the rectifier when an additional

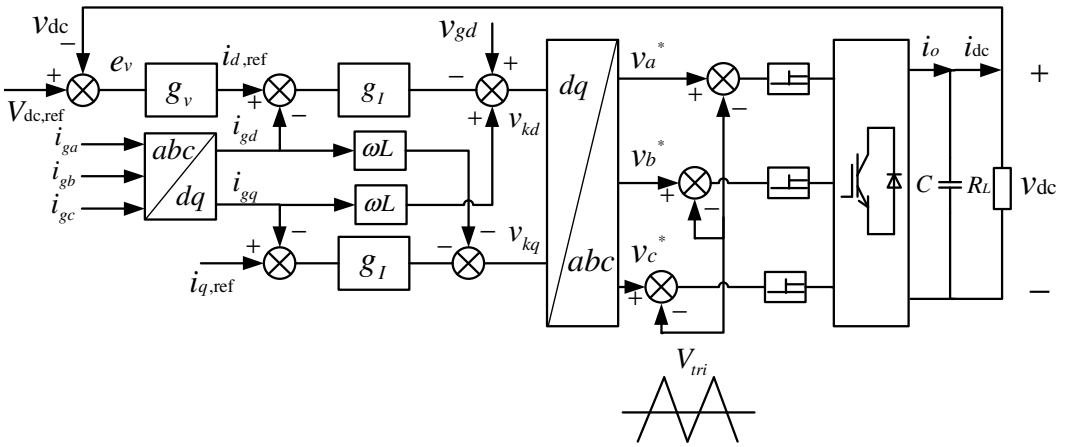

Figure 3.2: Controller schematic of the three-phase voltage source converter in rotating dq reference frame.

load comprising a series connection of a capacitor C_P and a resistor R_P as given in dotted lines in Fig. 3.1, is connected in parallel to the output of the rectifier at $t = 0.3$ s. This additional load essentially removes the charges stored in the output capacitor much faster than the controller's response. An equivalent step output voltage disturbance is thus created to test the response of the controller inside the rectifier.

The controller design normally compromises between the performances of the input power factor correction and the output voltage regulation of a rectifier [102]. A rule of thumb is to set the controller bandwidth close to the mains frequency (100 Hz) of the utility grid. However, the grid frequency is normally low and the power converters connected as loads to the rectifier are responding much faster. Thus, the electronic load manifests practically as an equivalent step output voltage disturbance which perturbs frequently the output voltage of the rectifier. The amount of output voltage disturbance depends on several parameters such as the time constant of the series connected R_PC_P load, the output filtering capacitance C and the response time of the controller. However, it will be more convenient to use a small varying R_P and a constant C_P from which the magnitude of the impulse current can be used as an approximate measure for

Table 3.1: Circuit components values of the three-phase voltage source converter.

$v_{ga,gb,gc}$	$v_{\rm dc}$	f	f_s	L	R_s	C
110 Vrms	360 V	50 Hz	10 kHz	4.2 mH	0.1–1 Ω	2.35 mF

the amount of voltage disturbance. It has been observed that the converter is stable if

- the additional load is light and purely resistive,
- the additional load is connected at cold start, and
- the difference between $v_{\rm dc}$ and the voltage across the additional load before the load is connected to the converter output is small.

When the impulse load current, which is a measure of the equivalent step output voltage disturbance, is high enough as shown in Fig. 3.3, it can be observed that the input line current increases suddenly to a very high value and stays there for the rest of the time unless the converter is shut down manually or by some protection mechanism. Normal operation is observed at the beginning of the simulation. Upon application of an impulse load current, the operation loses stability and enters a (unstable) regime that is accompanied by an expansion in the line current magnitude. Meanwhile, the output voltage $v_{\rm dc}$ drops abruptly to 0 V. However, the system behaves differently with different sets of parameter values. Comparing Figs. 3.3(a) and (b) with Figs. 3.3(c) and (d), we observe different dynamic behavior corresponding to different sets of circuit parameters.

Since the reactive power can be defined as

$$Q_a = v_{ga} i_{ga} \sin \Delta\phi, \text{for phase-a,} \tag{3.1}$$

where $\Delta\phi$ is the phase difference between line voltage and current. In Fig. 3.3(b), with a small R_s, the expansion of reactive power is clearly evidenced. This is the key consequence of this bifurcation phenomenon. Moreover, as R_s increases, real

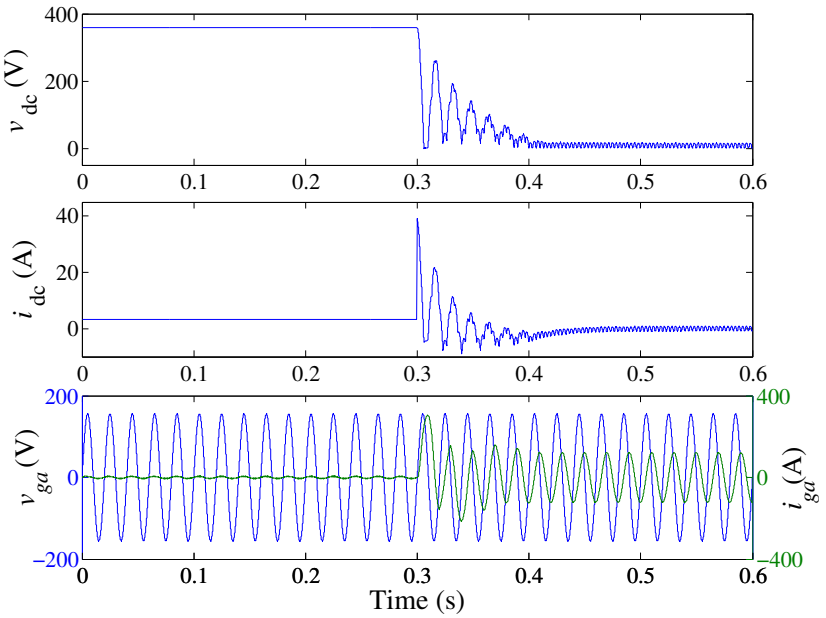
400
200
0
v_{dc} (V)
0 0.1 0.2 0.3 0.4 0.5 0.6
40
20
0
i_{dc} (A)
0 0.1 0.2 0.3 0.4 0.5 0.6
200
0
−200
v_{ga} (V)
400
0
−400
i_{ga} (A)
0 0.1 0.2 0.3 0.4 0.5 0.6
Time (s)

(a)

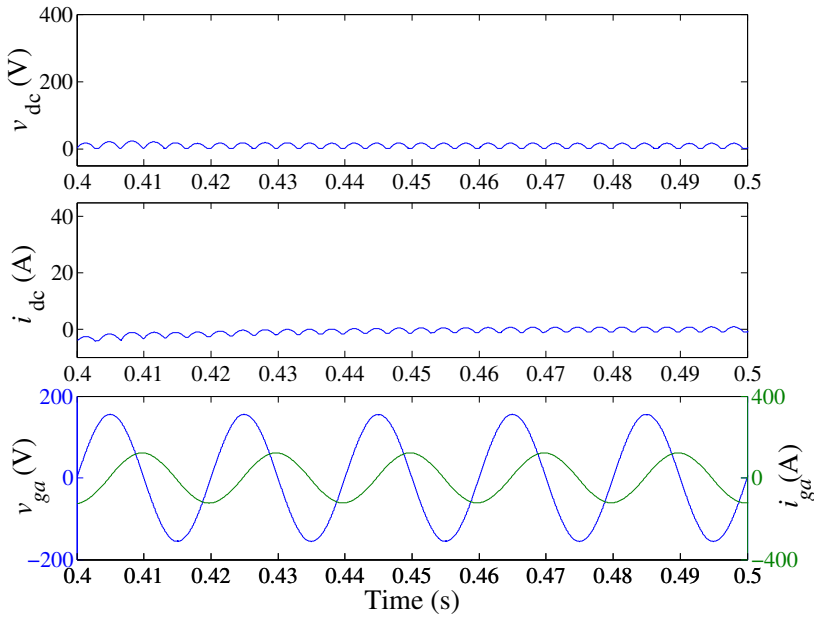
400
200
0
v_{dc} (V)
0.4 0.41 0.42 0.43 0.44 0.45 0.46 0.47 0.48 0.49 0.5
40
20
0
i_{dc} (A)
0.4 0.41 0.42 0.43 0.44 0.45 0.46 0.47 0.48 0.49 0.5
200
0
−200
v_{ga} (V)
400
0
−400
i_{ga} (A)
0.4 0.41 0.42 0.43 0.44 0.45 0.46 0.47 0.48 0.49 0.5
Time (s)

(b)

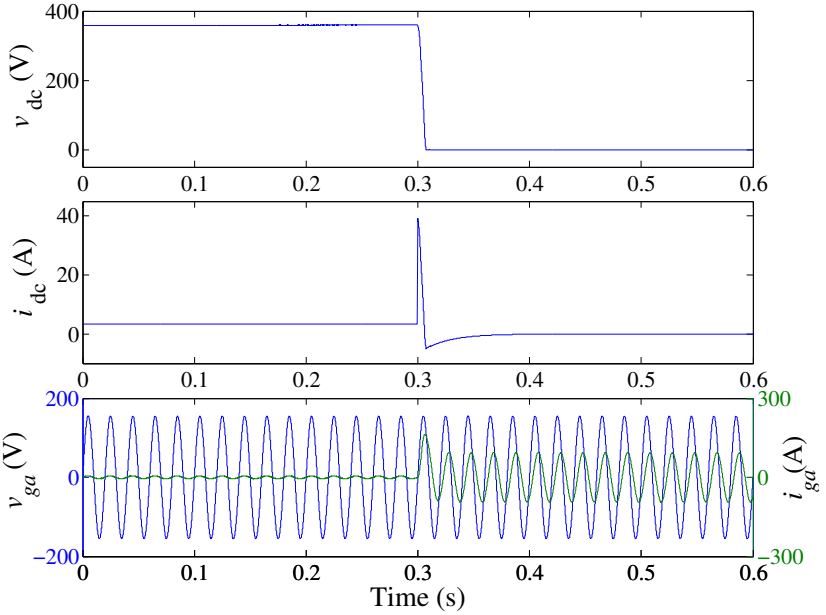

(c)

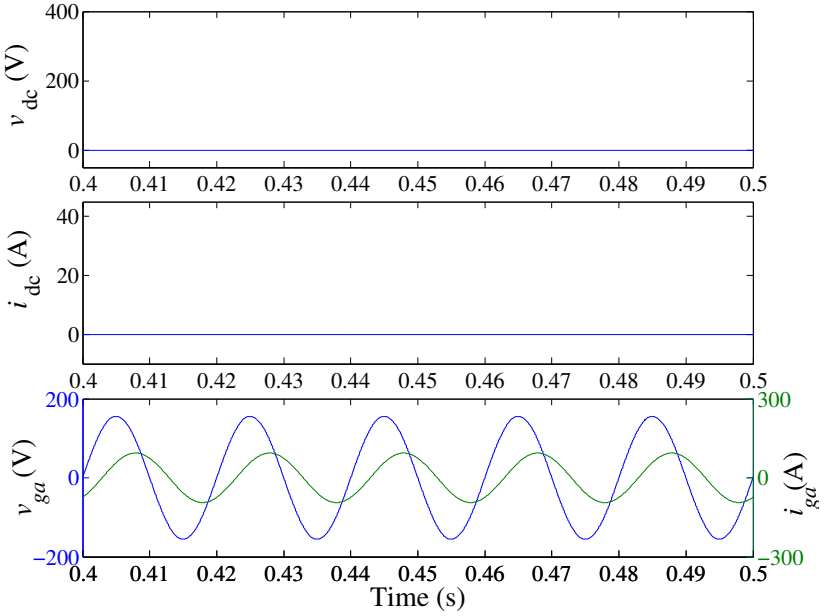

(d)

Figure 3.3: Transient waveforms showing catastrophic bifurcation of the rectifier at a load of $R_L = 110\ \Omega$. The system exhibits different dynamic behavior corresponding to different set of parameters. (a) for $R_s = 0.1\ \Omega$ and using a series load of capacitor of 2.35 mF and resistor of 10 Ω, (c) for $R_s = 1\ \Omega$ and using a series load of capacitor of 2.35 mF and resistor of 10 Ω. The input line current i_{ga} rises to a very high value and stays there after a capacitive load is connected to the output of the rectifier at $t = 0.3$ s. Here, the size of the step capacitive load and the series resistor can be regarded as bifurcation parameters, varying which would cause catastrophic bifurcation. (b) and (d) are the close-up waveforms of (a) and (c) showing the expansion of reactive power after the bifurcation point.

power loss in R_s adds to the reactive power expansion, as shown in Figs. 3.3(c) and (d).

The sudden irreversible increase in current magnitude can be considered as a catastrophic bifurcation, and is certainly a very undesirable behavior of the rectifier. In general, bifurcations can be classified into continuous and discontinuous bifurcations, depending on whether the states of the system are varying continuously or discontinuously as the control parameters are varied gradually through their critical values [64, 115, 116]. The discontinuous bifurcation phenomenon is usually accompanied with a structural change in the system as the control parameters are varied through the critical point, and such a bifurcation may cause undesirable or even catastrophic consequences as the state variables may exhibit undesirably wide excursion in the state space causing damage to some system components. In our case, the system experiences a sudden expansion of reactive power, which is dangerous for both the converter and the power grid. Thus, we describe the kind of bifurcation here as *catastrophic bifurcation* to distinguish the dangerous boundary from safe boundaries of other bifurcations. Moreover, the expanded current magnitude is not reversible by changing the capacitor load, and the large current magnitude could only be removed by shutting down the system.

3.2 Phase Portraits of Catastrophic Bifurcation

To illustrate the routes to catastrophic bifurcation, phase portraits of the control parameters of $i_{d,\mathrm{ref}}$ and i_{gd} are plotted as shown in Fig. 3.4. The phase portraits are obtained by applying a series load R_P–C_P, with $C_P = 2.35$ mF, to the output of the stable operating rectifier. Two different impulse magnitudes using $R_P = 30\ \Omega$ and $R_P = 10\ \Omega$ are applied, corresponding to the scenarios before and after the bifurcation. The results are a stable normal operating portrait and a catastrophic operating portrait, respectively, as shown in Fig. 3.4.

The stable phase portrait in Fig. 3.4 (a) is plotted using an impulse magnitude of 12 A ($R_P = 30\ \Omega$). After the impulse disturbance, the trajectory of the phase portrait of $i_{d,\text{ref}}$ and i_{gd} goes through a single transient loop and manages to return to the original stable operating point. For the catastrophic phase portrait shown in Fig. 3.4 (a), which corresponds to an impulse magnitude of 36 A ($R_P = 10\ \Omega$), the trajectory fails to converge to any bounded attractor, with i_{gd} following a damped oscillating path and $i_{d,\text{ref}}$ diverging to infinity. It should be noted that the range of $i_{d,\text{ref}}$ shown in Fig. 3.4 is for the purpose of illustrating the failure of convergence of the trajectory beyond the bifurcation point. In practice, $i_{d,\text{ref}}$ is limited by design, and so is the trajectory.

Similar behavior can be observed for the rectifier with $R_s = 1\ \Omega$ as shown in Fig. 3.4 (b), except that the trajectory is damped to a smaller magnitude of i_{gd}. The trajectory beyond the catastrophic bifurcation point likewise diverges to infinity.

3.3 Boundary of Catastrophic Bifurcation

The catastrophic bifurcation shown in Section 3.1 is caused by the nonlinear characteristics of the DC transfer functions of the current loop, as will be explained later in this chapter. The steady-state values of i_{gd} and i_o versus $i_{d,\text{ref}}$ for various values of R_s are shown in Fig. 3.5. Essentially, as shown in Fig. 3.5, both i_{gd} and i_o are nonlinearly related to $i_{d,\text{ref}}$, with possible unimodal and saturation characteristics.

In view of these nonlinear characteristics of the current transfer functions, we have performed a series of simulations to locate the catastrophic bifurcation boundaries in selected parameter spaces [117, 118]. Since the bifurcation is affected by a number of bifurcation parameters, we apply impulse load currents with pulse duration of approximately 1 to 5 ms, which is much faster than the

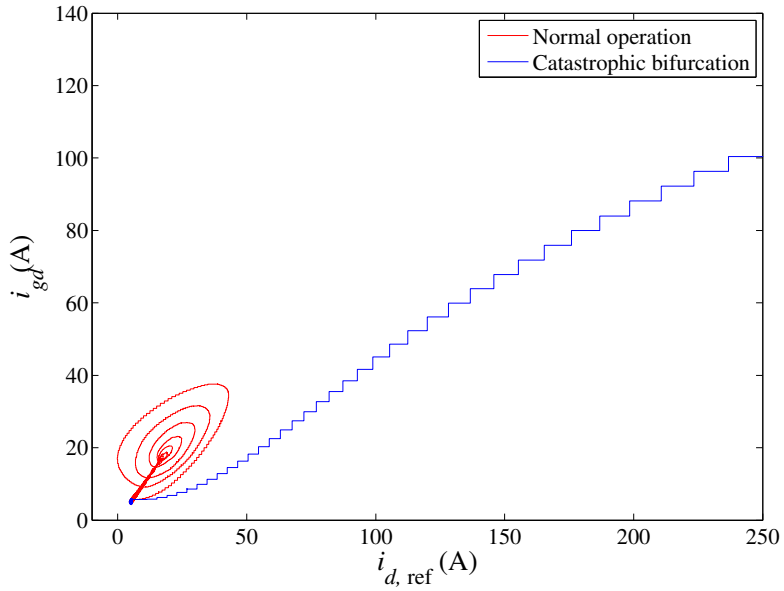

(a)

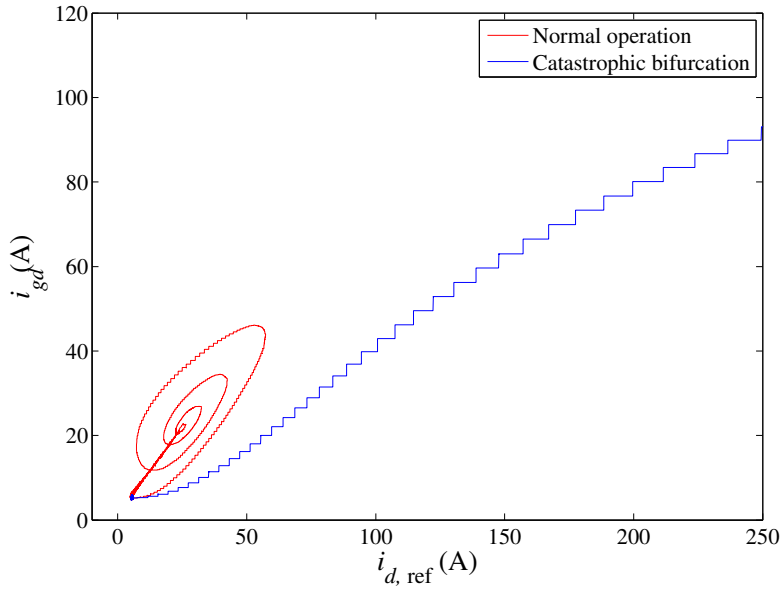

(b)

Figure 3.4: Phase portrait views of catastrophic bifurcation. (a) $R_s = 0.1\ \Omega$; (b) $R_s = 1\ \Omega$. The range of $i_{d,\mathrm{ref}}$ shown is for the purpose of illustrating the failure of convergence of trajectory beyond the bifurcation point. In practice, $i_{d,\mathrm{ref}}$ is limited by design, and so is the trajectory.

voltage loop and is sufficiently long for the purpose of triggering the bifurcation for different values of R_s and R_L. Note that the bifurcation has been shown to

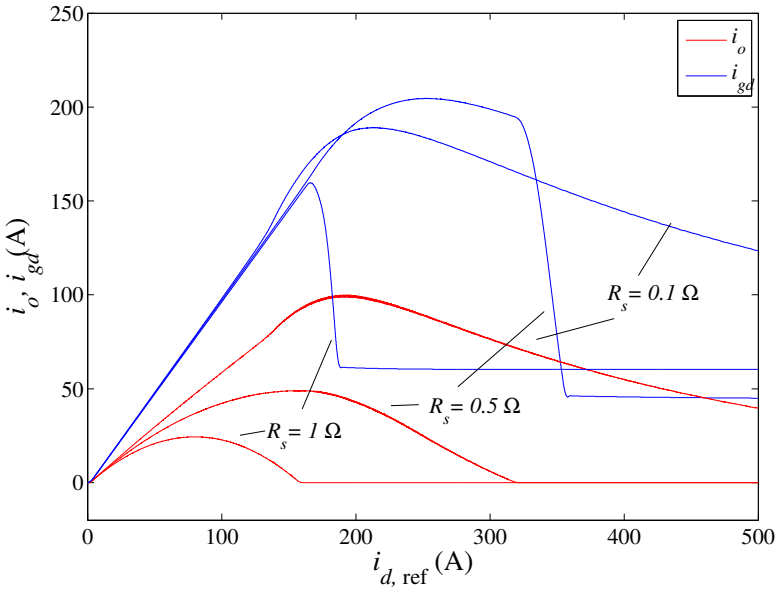

Figure 3.5: Steady-state plots of i_{gd} and i_o versus $i_{d,\mathrm{ref}}$, where v_{dc} is kept at 360 V by varying output resistance R_L.

be irreversible, and hence an impulse load current is suitable for studying this bifurcation and is also feasible for experimental study to be conducted later in the laboratory for verification purposes. The use of impulse load current would avoid the need for using a high power DC current load in the experiments. The boundaries found are shown in Fig. 3.6.

3.4 Analysis of Catastrophic Bifurcation

To understand the catastrophic bifurcation, it is essential to understand the system control in terms of the functional blocks shown in Fig. 3.2. The system is controlled by an inner current loop and an outer voltage loop. The inner current loop aims to minimize the error between the reference signal $(i_{d,\mathrm{ref}}, i_{q,\mathrm{ref}})$ and the current sensed (i_{gd}, i_{gq}). The outer voltage loop is responsible for minimizing the voltage difference between $V_{\mathrm{dc,ref}}$ and v_{dc}. The PI control is implemented in the rotating coordinate system instead of a stationary one. Here, the control loop

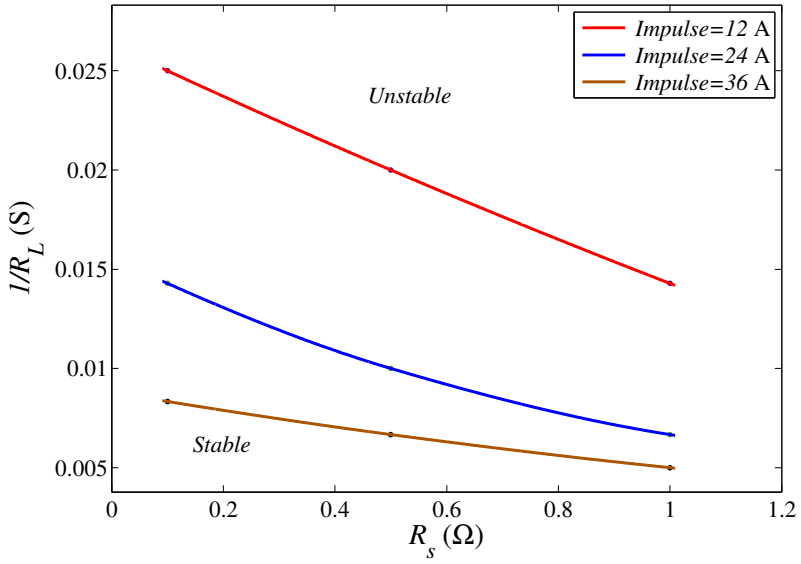

(a)

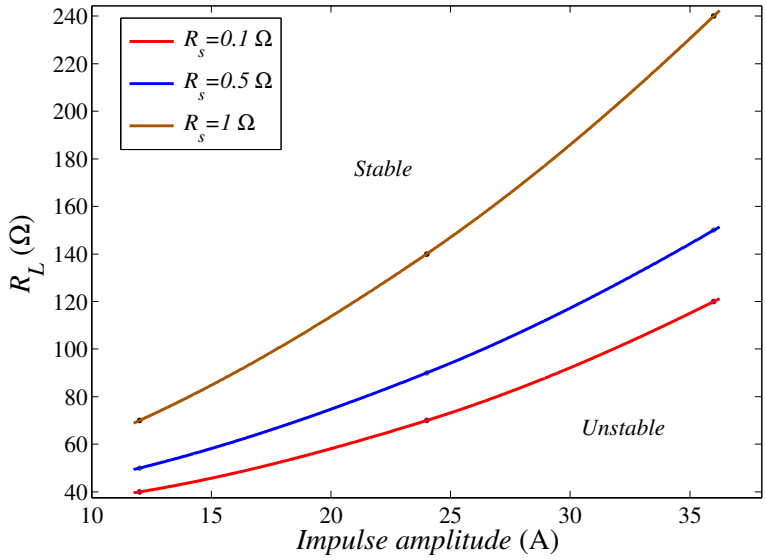

(b)

Figure 3.6: Bifurcation boundaries of the rectifier in parameter spaces of (a) $1/R_L$ versus R_s; and (b) R_L versus impulse.

can be simplified into a dual loop control for implementation. The control parameters, which are normalized in the practical system, are adopted in the model as well.

3.4.1 Inner Current Loop

The objective of the inner current loop is to provide a current i_{gx} (where $x = a, b, c$) which is either in-phase or anti-phase to the line voltage v_g, and whose magnitude is controlled by an external voltage loop. Specifically, the phase current i_g is generated by controlling v_k modulated from the capacitive voltage $v_{\rm dc}$, as shown in Fig. 3.1. The phase voltage v_k is a SPWM modulated version of v_k^*. The triangular wave angular frequency ω_s defines the switching frequency of the switches in Fig. 3.1. Denote the voltage command signal v_k^* as

$$v_k^* = V_k \sin(\omega t + \theta_k), \tag{3.2}$$

where $\omega = 2\pi f$. Assume that $\omega_s \gg \omega$, which is normally true. We have

$$\overline{v_k} = K \frac{v_{\rm dc}}{2} \frac{v_k^*}{V_{tri,\rm peak}}, \tag{3.3}$$

where $V_{tri,\rm peak}$ is the peak of V_{tri} and K is a scaling factor for control purpose.

Here, in (3.3), $\overline{v_k}$ is the state-space average of v_k over a switching period $T_s = \frac{2\pi}{\omega_s}$. We will use v_k for $\overline{v_k}$ subsequently to avoid symbol explosion. It is noted that v_k in (3.3) is modulated with the peak-to-peak magnitude of $v_{\rm dc}$ and is clamped between $\pm\frac{v_{\rm dc}}{2}$. Therefore, (3.3) is rewritten as

$$v_k(t) = K \frac{v_{\rm dc}}{2} m_k(t), \tag{3.4}$$

where

$$m_k(t) = \begin{cases} 1 & \text{if } |n_k(t)| \geq 1 \\ n_k(t) & \text{if } |n_k(t)| < 1 \end{cases}, \tag{3.5}$$

with

$$n_k(t) = \frac{v_k*}{V_{tri,\text{peak}}}.$$

Using this average model, the voltage-source rectifier in Fig. 3.1 can be formulated as follows.

$$L\frac{di_g}{dt} = v_g - R_s i_g - v_k \tag{3.6}$$

$$C\frac{dv_{\text{dc}}}{dt} = \sum_{x=a,b,c} i_g m_{kx}(t) - i_{\text{dc}} \tag{3.7}$$

Using three-dimensional stationary to two-dimensional synchronous reference frame transformation mentioned in Sections 2.2.1 to 2.2.3, equations (3.6) and (3.7) are expressed in d-q-0 transformed variables as

$$L\frac{di_{gd}}{dt} = \omega L i_{gq} + v_{gd} - R_s i_{gd} - v_{kd} \tag{3.8}$$

$$L\frac{di_{gq}}{dt} = -\omega L i_{gd} + v_{gq} - R_s i_{gq} - v_{kq} \tag{3.9}$$

$$i_{g0} = 0 \quad \text{(balanced 3-phase system)} \tag{3.10}$$

where subscripts d, q and 0 correspond to the standard d-q-0 transformed variables; i_{gd} and i_{gq} are used to represent the magnitude and phase respectively of i_{gx}, where $x = a, b, c$. The control of the system is illustrated in Fig. 3.2, where equations (3.8) and (3.9) are used in the inner-current loop and (3.7) is used in the outer-voltage loop.

Based on the PI control of current loop in Fig. 3.2, the control voltages are

$$v_q^* = -\omega L i_{gd} - g_I(e_q) \tag{3.11}$$

$$v_d^* = v_{gd} + \omega L i_{gq} - g_I(e_d) \tag{3.12}$$

where $e_q = i_{q,\text{ref}} - i_{gq}$ and $e_d = i_{d,\text{ref}} - i_{gd}$ are errors and $g_I(\cdot)$ is the PI compensa-

tion function of the current loop. The current-loop closed-loop equation can be formulated by equating (3.8), (3.9), (3.11) and (3.12) for (v_{kq}, v_{kd}) and (v_q^*, v_d^*) using either the time-domain piecewise linear equations (3.4) and (3.5) or the continuous-time fundamental component approximated equation (2.49).

Normally, the control system is optimized for the region of linear modulation. Therefore, (2.41) is used. Equations (3.8), (3.9), (3.11) and (3.12) can be combined by putting $v_{kq} = v_q^*$ and $v_{kd} = v_d^*$ with $K = \frac{2V_{tri,\text{peak}}}{V_{\text{dc,ref}}}$. Suppose the voltage loop is stable and v_{dc} is regulated at $V_{\text{dc,ref}}$. Thus, we have

$$L\frac{de_q}{dt} - (K_{ip} - R_s)e_q - K_{ii}\int e_q dt = R_s i_{q,\text{ref}} \tag{3.13}$$

$$L\frac{de_d}{dt} - (K_{ip} - R_s)e_d - K_{ii}\int e_d dt = R_s i_{d,\text{ref}} \tag{3.14}$$

where $g_I(x) = K_{ip}x + K_{ii}\int x dt$ with K_{ip} and K_{ii} being design constants.

From (3.13) and (3.14), the relationship between system implementation and inner current loop control parameters can be found easily. The stability of the inner current loop can be achieved by properly choosing the circuit and control parameters in these two equations. Here, we assume that the parameters are properly designed and the inner current loop works normally.

It can be observed that when the modulation enters the nonlinear region of (2.48) or (3.5), the control deviates from the optimal system characteristic of (3.13) and (3.14). Fortunately, the exact dynamics of the current control loop are not crucial in explaining the catastrophic bifurcation observed here, since the inner current loop is much faster than the outer voltage loop. Using power balance (3.15), the steady-state current transfer function (3.16) can be obtained. To simplify the analysis, the aggregated inductor resistive loss is considered as

the equivalent total loss of the converter.

$$P_{\text{load}} = P_{\text{input}} - P_{\text{loss}} \tag{3.15}$$

$$i_o = \frac{3\left(v_{gd}i_{gd} + v_{gq}i_{gq} - R_s\left(i_{gd}^2 + i_{gq}^2\right)\right)}{2v_{\text{dc}}} \tag{3.16}$$

The steady-state transfer functions of i_o and i_{gd} versus $i_{d,\text{ref}}$ are plotted as shown in Fig. 3.5 using both (3.16) and circuit simulations with different values of R_s. It is evidenced from (3.16) and Fig. 3.5 that there is a maximum i_o, denoted as $i_{o,\max}$ with corresponding $i_{gd}(i_{o,\max})$. There are two possible i_{gd}'s for any output current $i_o < i_{o,\max}$. Denoting the two i_{gd}'s as i_{gd1} and i_{gd2}, we have

$$i_{gd1} < i_{gd}(i_{o,\max}) < i_{gd2}. \tag{3.17}$$

The unimodal transfer function shown in Fig. 3.5 has indicated two saturation mechanisms. According to (3.11), (3.12) and (3.16), i_o increases with increasing v_q^* and v_d^* which can be caused by increasing $i_{d,\text{ref}}$ and keeping $i_{q,\text{ref}}$ at zero within the current control loops. With the current control loop kept below saturation, we have $(v_{kq}, v_{kd}) \approx (v_q^*, v_d^*)$ and $(i_{gq}, i_{gd}) \approx (i_{q,\text{ref}}, i_{d,\text{ref}}) = (0, i_{d,\text{ref}})$, i.e.,

$$i_{gq} = 0, \text{ and} \tag{3.18}$$

$$i_{gd} = i_{d,\text{ref}}. \tag{3.19}$$

However, i_o saturates at $i_{o,\max} = \frac{v_{gd}^2}{8v_{\text{dc}}R_s}$ due to the output power saturation as indicated in the i_o versus $i_{d,\text{ref}}$ transfer functions for $R_s = 1\ \Omega$ and $0.5\ \Omega$, as shown in Fig. 3.5. Before i_o saturates, i_{gd} increases linearly with increasing $i_{d,\text{ref}}$.

When R_s is sufficiently small, as shown in the transfer curves for $R_s = 0.1\ \Omega$ plotted in Fig. 3.5, the current control loop would saturate before i_o does. The

current control loop saturates when v_{kq} and v_{kd} reach the upper bound given by

$$\sqrt{v_{kd}^2 + v_{kq}^2} \leq V_{k,\max} = \frac{2v_{\rm dc}}{\pi}, \tag{3.20}$$

where $V_{k,\max}$ is the maximum magnitude of the fundamental at ω given by (2.48) or the fundamental component of v_k in (3.4). Using (3.8) and (3.9), the critical value $i_{gd,\rm critical}$ of i_{gd} occurs at

$$i_{gd,\rm critical} = \frac{v_{gd}R_s + \sqrt{v_{gd}^2 R_s^2 + (R_s^2 + \omega^2 L^2)(v_{gd}^2 - V_{k,\max}^2)}}{R_s^2 + \omega^2 L^2} \tag{3.21}$$

For any $i_{d,\rm ref} > i_{gd,\rm critical}$, the converter can no longer maintain a unity power factor. From (3.11) and (3.12), the steady-state saturation errors of e_q and e_d dominate, giving

$$\frac{v_d^*}{v_q^*} = \frac{-(i_{d,\rm ref} - i_{gd})}{-(i_{q,\rm ref} - i_{gq})} = \frac{-(i_{d,\rm ref} - i_{gd})}{i_{gq}}. \tag{3.22}$$

Therefore, using (3.20), we have

$$v_{kd,\rm saturated} = \frac{-(i_{d,\rm ref} - i_{gd})}{\sqrt{(i_{d,\rm ref} - i_{gd})^2 + i_{gq}^2}} V_{k,\max} \tag{3.23}$$

$$v_{kq,\rm saturated} = \frac{i_{gq}}{\sqrt{(i_{d,\rm ref} - i_{gd})^2 + i_{gq}^2}} V_{k,\max} \tag{3.24}$$

From (3.8) and (3.9), $v_{kd,\rm saturated}$ and $v_{kq,\rm saturated}$ are also given by

$$v_{kd,\rm saturated} = \omega L i_{gq} + v_{gd} - R_s i_{gd} \tag{3.25}$$

$$v_{kq,\rm saturated} = -\omega L i_{gd} + v_{gq} - R_s i_{gq} \tag{3.26}$$

Eliminating $v_{kd,\rm saturated}$ and $v_{kq,\rm saturated}$ from (3.23) to (3.26), the values of i_{gd} and i_{gq} after $i_{d,\rm ref} \geq i_{gd,\rm critical}$ can be calculated in terms of $i_{d,\rm ref}$ as $i_{gd} =$

$h_d(i_{d,\text{ref}})$ and $i_{gq} = h_q(i_{d,\text{ref}})$. Both $h_d(i_{d,\text{ref}})$ and $h_q(i_{d,\text{ref}})$ can be calculated in a straightforward manner, and we can write

$$i_{gd} = f_d(i_{d,\text{ref}}), \text{ and} \tag{3.27}$$

$$i_{gq} = f_q(i_{d,\text{ref}}) \tag{3.28}$$

where

$$f_d(i_{d,\text{ref}}) = \begin{cases} i_{d,\text{ref}} & \text{if } i_{d,\text{ref}} < i_{gd,\text{critical}} \\ h_d(i_{d,\text{ref}}) & \text{if } i_{d,\text{ref}} \geq i_{gd,\text{critical}} \end{cases} \quad \text{and} \tag{3.29}$$

$$f_q(i_{d,\text{ref}}) = \begin{cases} 0 & \text{if } i_{d,\text{ref}} < i_{gd,\text{critical}} \\ h_q(i_{d,\text{ref}}) & \text{if } i_{d,\text{ref}} \geq i_{gd,\text{critical}} \end{cases} \tag{3.30}$$

The i_o versus $i_{d,\text{ref}}$ transfer function for various values of R_s can be calculated using (3.16), (3.18), (3.19), (3.27) and (3.28), as given in Fig. 3.7(a).

The detailed calculation results can be listed below, when $R_s = 0.1\ \Omega$,

$$\begin{aligned} h_d(i_{d,\text{ref}}) = (&8789230.0 i_{d,\text{ref}} + 2968560.0 * (4.0 i_{d,\text{ref}}^2 - 72.94 i_{d,\text{ref}} - 65066.38)^{(1/2)} \\ &+3876.0 i_{d,\text{ref}} (0.5 (4.0 i_{d,\text{ref}}^2 - 72.94 i_{d,\text{ref}} - 65066.38)^{(1/2)} - 13.41) \\ &+2635.0 i_{d,\text{ref}}^2 - 122963706.47) \\ &/ (289.0 i_{d,\text{ref}}^2 - 5270.0 i_{d,\text{ref}} + 4084250.0) \end{aligned} \tag{3.31}$$

$$\begin{aligned} h_q(i_{d,\text{ref}}) = (&624650.0 i_{d,\text{ref}} + 459420.0 * (4.0 i_{d,\text{ref}}^2 - 72.94 i_{d,\text{ref}} - 65066.38)^{(1/2)} \\ &-50388.0 i_{d,\text{ref}} (0.5 (4.0 i_{d,\text{ref}}^2 - 72.94 i_{d,\text{ref}} - 65066.38)^{(1/2)} - 13.41) \\ &-34255.0 i_{d,\text{ref}}^2 + 551050584.12) \\ &/ (289.0 * x^2 - 5270.0 * x + 4084250.0) \end{aligned} \tag{3.32}$$

When $R_s = 0.5\ \Omega$,

$$\begin{aligned} h_d(i_{d,\text{ref}}) = (&222091150.0 i_{d,\text{ref}} + 63612000.0 * (4.0 i_{d,\text{ref}}^2 - 319.59 i_{d,\text{ref}} - 43835.12)^{(1/2)} \\ &+552900.0 i_{d,\text{ref}} (0.5(4.0 i_{d,\text{ref}}^2 - 319.59 i_{d,\text{ref}} - 43835.12)^{(1/2)} - 58.76) \\ &+375875.0 i_{d,\text{ref}}^2 - 12893105734.54) \\ &/(9409.0 i_{d,\text{ref}}^2 - 751750.0 i_{d,\text{ref}} + 116521250.0) \end{aligned} \tag{3.33}$$

$$\begin{aligned} h_q(i_{d,\text{ref}}) = (&78081250.0 i_{d,\text{ref}} + 57427500.0 (4.0 i_{d,\text{ref}}^2 - 319.59 i_{d,\text{ref}} - 43835.12)^{(1/2)} \\ &-1437540.0 i_{d,\text{ref}} (0.5(4.0 i_{d,\text{ref}}^2 - 319.59 i_{d,\text{ref}} - 43835.12)^{(1/2)} - 58.76) \\ &-977275.0 i_{d,\text{ref}}^2 + 7335134909.79) \\ &/(9409.0 i_{d,\text{ref}}^2 - 751750.0 i_{d,\text{ref}} + 116521250.0) \end{aligned} \tag{3.34}$$

The catastrophic bifurcation will be explained in the next subsection in terms of the interaction of this current transfer function and the outer voltage loop.

3.4.2 Outer Voltage Loop

The outer voltage loop is responsible for minimizing the voltage difference between $V_{\text{dc,ref}}$ and v_{dc}. The control of the output voltage, as described in Fig. 2.6, is given as

$$i_{d,\text{ref}} = g_v(e_v), \tag{3.35}$$

where

$$e_v = V_{\text{dc,ref}} - v_{\text{dc}}, \tag{3.36}$$

$$g_v(e_v) = K_{vp} e_v + K_{vi} \int e_v dt. \tag{3.37}$$

with K_{vp} and K_{vi} being design constants used in the converter implementation.

Combining with (3.7) and (3.16), the voltage loop-gain state equation is obtained as

$$C\frac{de_v}{dt}+\frac{3}{2}\frac{v_{gd}f_d\left(g_v(e_v)\right)-R_s\left(f_d^2\left(g_v(e_v)\right)+f_q^2\left(g_v(e_v)\right)\right)}{v_{\rm dc}}-\frac{v_{\rm dc}}{R_L}=0. \tag{3.38}$$

The outer voltage loop can be designed according to (3.37) and (3.38). The circuit and control parameters can be chosen according to system specification. Here, instead of optimizing the circuit and control parameters, we focus on the undesirable operation described by these two equations. Since (3.38) is nonlinear, we apply the usual linearization and perturbation procedure to obtain the following small signal equation:

$$C\frac{d\hat{e}_v}{dt}+\frac{3}{2}\frac{v_{gd}f_d'-2R_s(f_df_d'+f_qf_q')}{v_{\rm dc}}g_v(\hat{e}_v)=0, \tag{3.39}$$

where v_{gd} is the steady-state solution of the converter. The values of $v_{\rm dc}$ can be approximated as $V_{dc,\rm ref}$. Substituting $y=\int\hat{e}_v dt$, (3.39) can be rewritten as

$$\ddot{y}+\frac{3}{2C}\frac{v_{gd}f_d'-2R_s(f_df_d'+f_qf_q')}{V_{\rm dc,ref}}(K_{vp}\dot{y}+K_{vi}y)=0, \tag{3.40}$$

and the characteristic equation is

$$\lambda^2+\frac{3}{2C}\frac{v_{gd}f_d'-2R_s(f_df_d'+f_qf_q')}{V_{\rm dc,ref}}(K_{vp}\lambda+K_{vi})=0. \tag{3.41}$$

The roots of the characteristic equation can be easily found. The root locus is computed for parameters listed in Table 3.1 with $R_s=1\ \Omega$, as illustrated in Fig. 3.7. When the output current i_o is increasing, which would result in an increment in $i_{d,\rm ref}$, the roots of the characteristic equation (3.41) move along the red locus shown in Fig. 3.7 (b). Once this root locus hits the origin of the complex s-plane, it splits into two real roots which move in opposite directions. A right

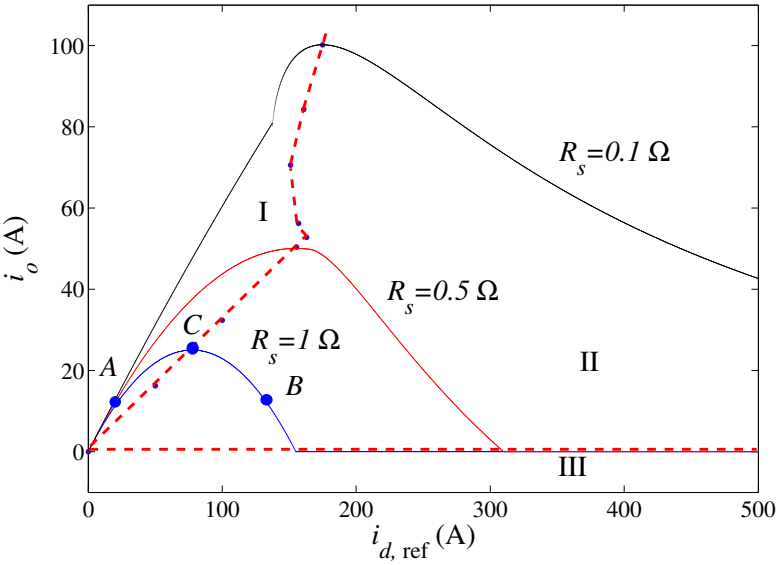

(a)

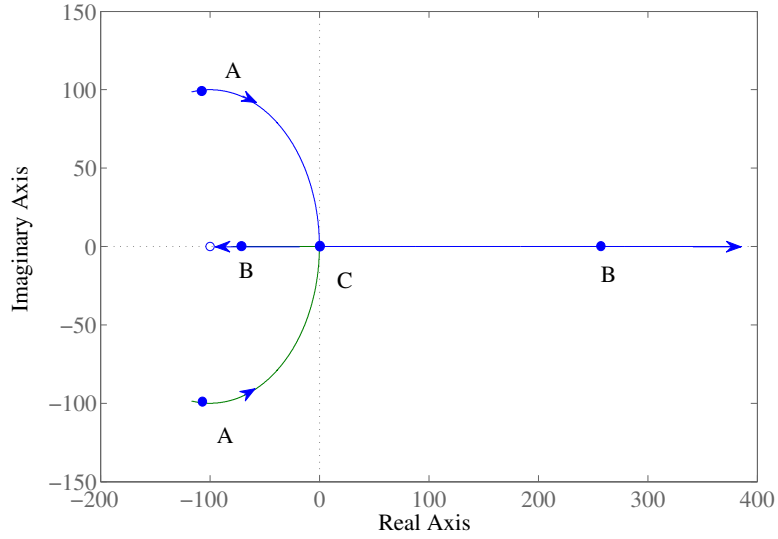

(b)

Figure 3.7: (a) Operating plots i_o versus $i_{d,\text{ref}}$; (b) root locus on s-plane of outer voltage loop characteristic equation. Operating point A (region I) corresponds to stable operation with characteristic roots located in the stable left-half s-plane. Critical operating point C corresponds to characteristic roots merging to origin in the s-plane. Crossing point C, the system moves to unstable region II, corresponding to a characteristic root located in the positive real axis. The system cannot stay in this unstable operating state and drifts to region III irreversibly.

half plane (RHP) root immediately emerges, meaning that the outer voltage loop is no longer stable. More specifically, referring to Fig. 3.7 (a), with $i_o < i_{o,\max}$, we have $i_{d,\text{ref}} = i_{gd1}$ or i_{gd2} as explained earlier. If $i_{d,\text{ref}} = i_{gd1} < i_{gd}(i_{o,\max})$, corresponding to point A (region I) in Fig. 3.7 (a), the roots of the characteristic equation are complex and satisfy

$$Re|\lambda| < 0, \tag{3.42}$$

and the system is stable. However, as $i_{d,\text{ref}}$ increases, point A moves towards the critical point C, where $i_o = i_{o,\max}$. At this point, the roots of the characteristic equation are 0. As $i_{d,\text{ref}}$ increases further, the operating point moves to point B (region II), which is unstable as the roots are real with

$$\lambda_1 < 0, \lambda_2 > 0. \tag{3.43}$$

The system fails to operate stably at B and drifts towards region III, as shown in Fig. 3.7 (a). The operating point cannot revert to region I unless $i_{d,\text{ref}}$ is reset.

Thus, if the system is subject to external perturbation such that it enters the unstable region, then $i_{d,\text{ref}}$ will be driven to a much higher value (corresponding to region III), which causes the system to enter an abnormal state where no active power is produced.

Clearly, the boundary of the catastrophic bifurcation can be calculated in terms of the incremental $i_{d,\text{ref}}$ that is pushed by external perturbation. The condition for the occurrence of catastrophic bifurcation is when $i_{d,\text{ref}}$ is pushed to the critical operation point $i_{gd}(i_{o,\max})$ where the characteristic roots land on the real axis and one enters the unstable region, i.e.,

$$\Delta i_{d,\text{ref}} = i_{gd}(i_{o,\max}) - i_{gd} \tag{3.44}$$

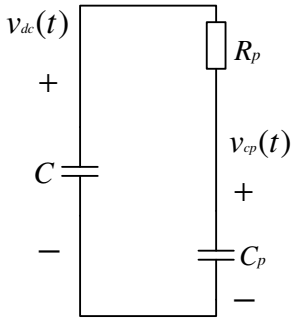

Figure 3.8: Discharge model for the estimation of output voltage variation upon insertion of the impulse load of $R_P C_P$.

Furthermore, suppose $\Delta i_{d,\mathrm{ref}}(t)$ is driven by the impulse current upon insertion of R_P–C_P at $t = 0$ on the DC side, i.e.,

$$\Delta i_{d,\mathrm{ref}}(t) = g_v(e_v) = g_v(V_{dc,\mathrm{ref}} - v_{dc}(t)), \tag{3.45}$$

where

$$v_{dc}(t) = \frac{V_{dc,\mathrm{ref}}(e^{-\frac{t}{R_P C_{eq}}} + \frac{C}{C_P})}{1 + \frac{C}{C_P}}, \text{ and} \tag{3.46}$$

$$C_{eq} = \frac{C C_P}{C + C_P} \tag{3.47}$$

are estimated from the model given in Fig. 3.8. We assume that the outer voltage loop has nearly no response within the delay time t_d [108], which is given by

$$t_d \cong \frac{1.1 + 0.125\delta + 0.469\delta^2}{\omega_n}, \tag{3.48}$$

where δ and ω_n are calculated from the characteristic equation (3.41). Considering the fast transient within t_d, variation of voltage due to $i_o R_L$ and the integration effect of g_v have been ignored in the calculation for simplicity. Thus, the R_P that

may drive the converter into catastrophic bifurcation is given by

$$R_P = -\frac{t_d}{C_{eq}\ln((1-\frac{i_{gd}(i_{o,\max})-i_{gd})}{K_{vp}V_{dc,\mathrm{ref}}})(1+\frac{C}{C_P})-\frac{C}{C_P})} \tag{3.49}$$

When $R_s = 1\ \Omega$ and the steady-state load current $i_o = 3.27$A, an R_P smaller than 15.5 Ω, or an impulse current higher than 23.5 A, is enough to drive the converter into catastrophic bifurcation.

3.5 Experimental Observation

Our purpose here is to verify the catastrophic bifurcation phenomenon identified and analyzed in previous sections. Table 3.2 gives the component values used. For experimental feasibility, a non-optimized equivalent value of $R_s = 1\ \Omega$ is used to illustrate the existence of the catastrophic bifurcation. Figure 3.9 shows the experimentally observed bifurcation behavior, which is in perfect agreement with the simulated results given in Figs. 3.3 (c) and (d). The undesirable operation can be clearly identified in the waveform. The system achieves normal operation, and quickly moves to an abnormal one upon application of a current impulse. The result shows that the converter exhibits the bifurcation phenomenon mentioned in Section 3.4.

Note that we use a non-optimized R_s here due to the current rating constraint of the main switches, nonetheless, the result adequately validates the phenomenon as explained in Section 3.1. The impulse current amplitude used is 36 A, as calculated in the previous section. For smaller R_s, the current expansion is expected to be very severe without a proper limiting arrangement, as shown in the simulated waveforms given in Figs. 3.3 (a) to (b). This phenomenon is clearly highly undesirable and should be avoided.

The real power loss of the converter can be calculated considering the total

Table 3.2: Circuit components values of the experimental three-phase voltage source converter with an input protective transformer. The component values of L, R_s and C are referred to the transformer secondary.

Parameters/Components	Values
$v_{ga,gb,gc}$	110 Vrms
$v_{\rm dc}$	360 V
f	50 Hz
f_s	10 kHz
L	4.2 mH
R_s	1 Ω
C	2.35 mF
R_L	110 Ω
R_P	10 Ω
C_P	2.35 mF
K_{vp}	2 Ω^{-1}
K_{vi}	500 $(\Omega s)^{-1}$

resistance of converter R_{total}. For the balanced three-phase system, the real power loss is

$$P_{loss} = 3i_{ga,\rm RMS}^2 R_{total}. \tag{3.50}$$

In the experiment, the $i_{ga,\rm RMS}$ expands from 4 A to 43.53 A. Therefore, the real power loss increases over 100 times.

3.6 Summary

Catastrophic bifurcation has been found for the three-phase boost power rectifier. Essentially, the input current suddenly expands as a sufficiently large step load is connected, or under variation of other parameters. The root cause of this phenomenon is the nonlinear characteristics of the current transfer functions of the converter. The output current will reach a maximum as the control reference current increases, altering the system's loop-gain, thereby destabilizing the system. A common practice of preventing this catastrophic bifurcation is to clamp the control reference current below the maximum point. Stability boundaries

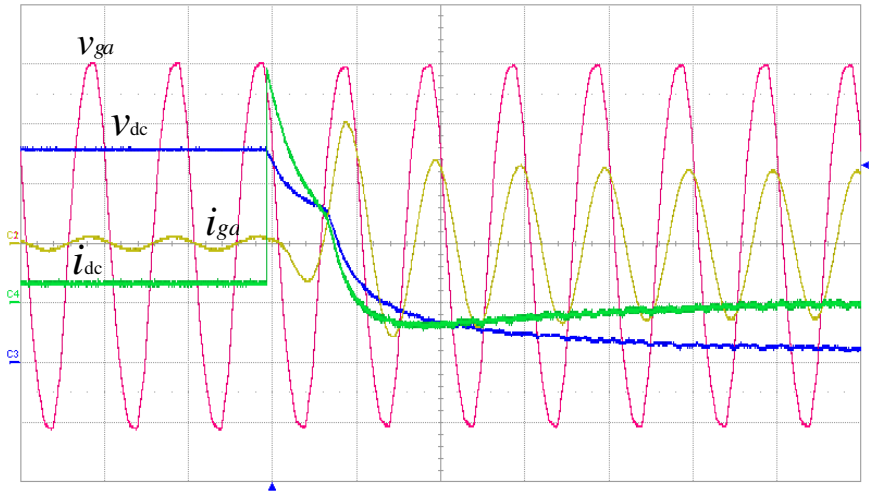

(a)

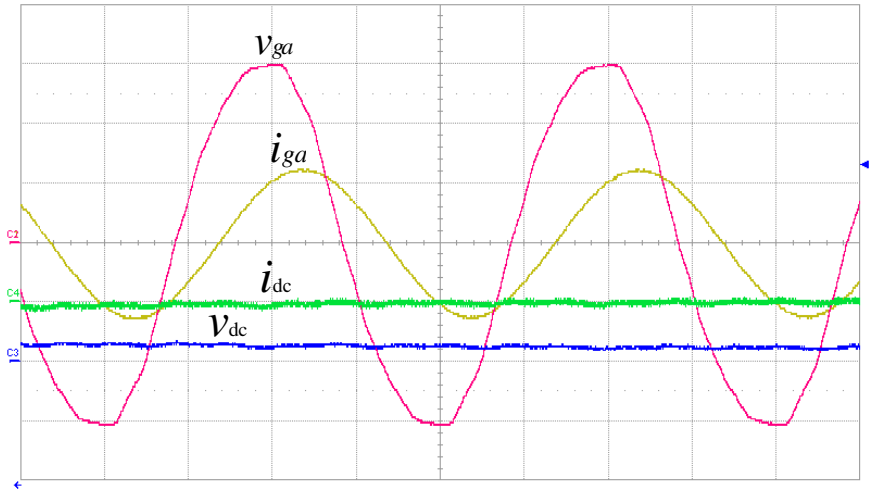

(b)

Figure 3.9: Experimental waveforms showing catastrophic bifurcation of the rectifier when it is triggered by a current impulse shown as green channel 4 (10 A/div). Channel 1 (red, 50 V/div), channel 2 (yellow, 50 A/div) and channel 3 (blue, 100 V/div) are waveforms of phase-a line voltage v_{ga}, line current i_{ga} and output voltage $v_{\rm dc}$, respectively. (a) Waveforms of the one-shot transient response at 20 ms/div with timing of the triggering load current impulse. The system clearly experiences a transition from normal operation to an abnormal one. (b) Enlarged waveforms at 5 ms/div after the impulse triggering, where the line input current i_{ga} stays high, and output voltage drops to a value much below the reference voltage of the voltage loop of the rectifier circuit.

have been identified for the converter, clearly suggesting how stability could be affected by variation of some selected parameters.

In this chapter, we report the catastrophic bifurcation in the three-phase voltage source converter and identify the cause of the bifurcation. Our results provide design information regarding the choice of operating parameters that would ensure proper stable operation. Specifically we consider a common control scheme applied to the three-phase voltage source converter, and we show that the bifurcation is caused by the nonlinear operation of the converter circuit. When triggered by an impulse load current, the system loses stability in a catastrophic bifurcation which is accompanied by an expansion of reactive power or equivalently an expanded excursion in the state space.

Chapter 4

Irreversible Bifurcation Phenomenon

The three-phase voltage source converter is normally designed with the assumption of ideal input voltage conditions. However, non-ideal voltage conditions are common in practical input supply sources, especially in weak AC systems [60, 119]. In addition, some other loads may connect to the power grid at the point of common coupling (PCC) in practice. Under such a situation, the system works under non-ideal input conditions and is at the same time interacting with other loads via the grid, as depicted in Fig. 4.1. In this representation, L_g represents the grid impedance, which is mostly inductive in practice. Also, a simplified three-phase balanced interacting load R is connected to the same PCC.

With the grid impedance and interacting load varying unpredictably, if the design of the control loop assumes the presence of an ideal power grid, undesirable problems can be expected when the system works under the influence of a realistic source impedance and variation of interacting load. In this chapter, we will study the situation that the grid impedance is inductive and a three-phase balanced resistive load is connected at the same PCC which is interacting with the VSC.

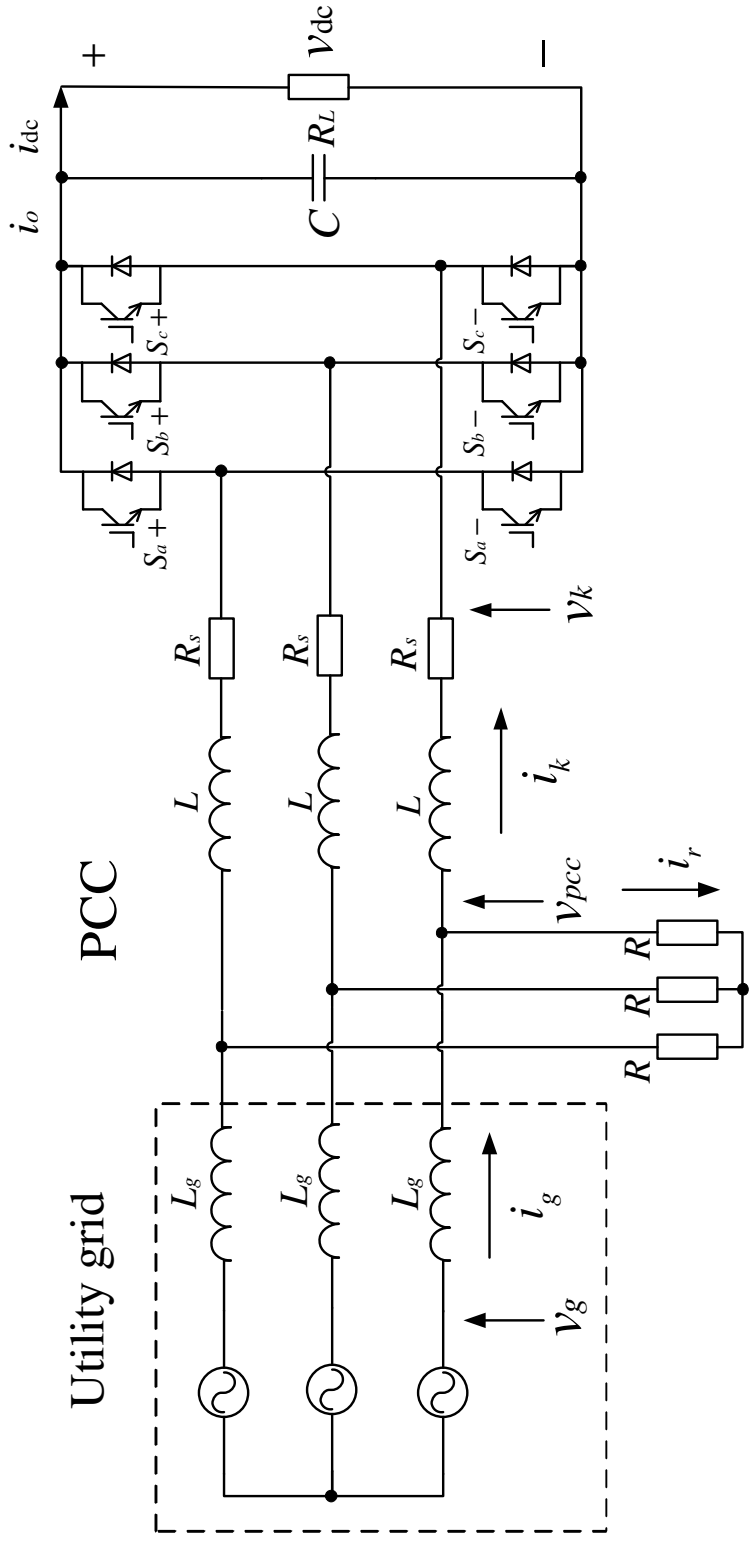

Figure 4.1: Three-phase voltage source converter or boost rectifier connecting to non-ideal grid with interacting load.

Table 4.1: Parameters of non-ideal power grid and interacting load.

$v_{ga,gb,gc}$	f	L_g	R
110 Vrms	50 Hz	0.1–4 mH	0.4–10 Ω

Table 4.2: Circuit parameters of the three-phase voltage source converter.

$V_{\mathrm{dc,ref}}$	R_s	L	C	R_L	f_s
360 V	0.01 Ω	1.2 mH	2.35 mF	32 Ω	10 kHz

4.1 A Glimpse at the Instability

The circuit is shown in Fig. 4.1, and the control stays the same as shown in Chapter 3. The whole system is implemented using MatLab. The circuit components and grid parameters used in the simulation are shown in Tables 4.1 and 4.2. Instability has been observed with the values of the interacting load resistance used in the simulation. Figure 4.2 and 4.3 show the transient waveforms illustrating the instability when a varying resistive interacting load is presented with the grid impedance $L_g = 3$ mH.

From Fig. 4.2, we observe that, when the interacting resistive load becomes heavy, the output voltage V_{dc} cannot be maintained at the regulated level, and decreases to a very small level. Furthermore, the whole transient process can be observed in Fig. 4.2(b). Moreover, the magnitude of the input current soars to a very high value while the input voltage drops to a small value unless the converter is shut down manually or by some protection mechanism. Meanwhile, the phase shift of voltage $v_{ka,kb,kc}$ approaches 180° relative to the input line voltage, as shown in Fig. 4.3. The expansion of reactive power is clearly evidenced in Fig. 4.3.

In addition, from Fig. 4.4(a), we see that the switching signals work at the line frequency with the phase shift being 180° relative to the input line voltage. Furthermore, as shown in Fig. 4.4(b), the command signals are much larger than the triangular carrier wave, and are intersecting with the carrier at the line frequency. The transition to instability can be regarded as a catastrophic bifurcation

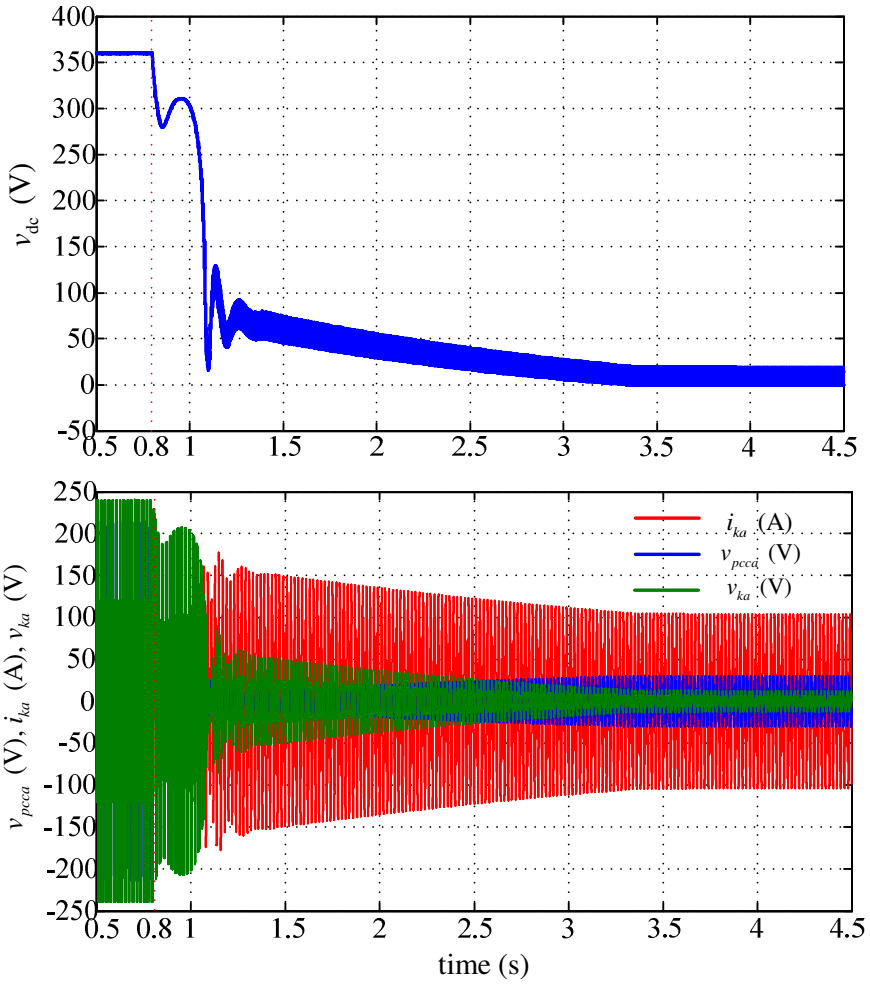

(a)

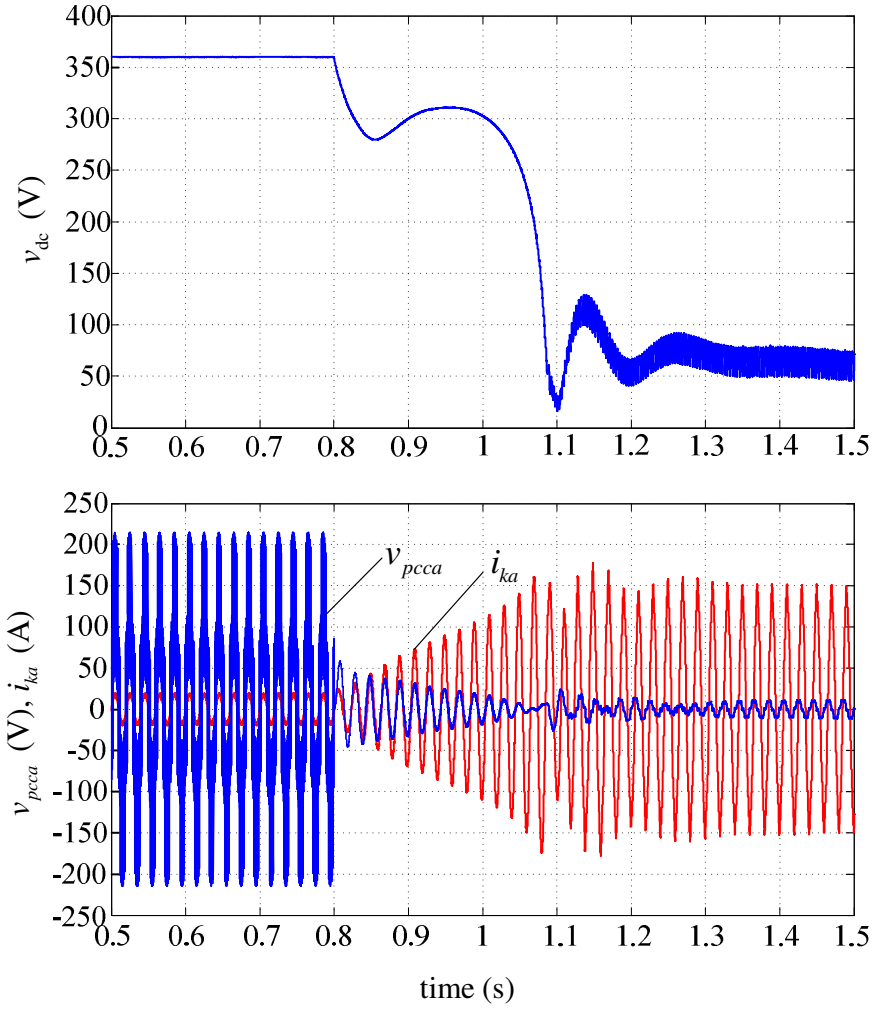

(b)

Figure 4.2: Irreversible instability caused by presence of grid impedance and interacting load. (a) Transient waveforms for $R = 0.4\ \Omega$ connecting to PCC at $t = 0.8$ s. (b) Enlargement of the waveforms of (a) around $t = 1$ s. The instability can only be removed by shutting down the system.

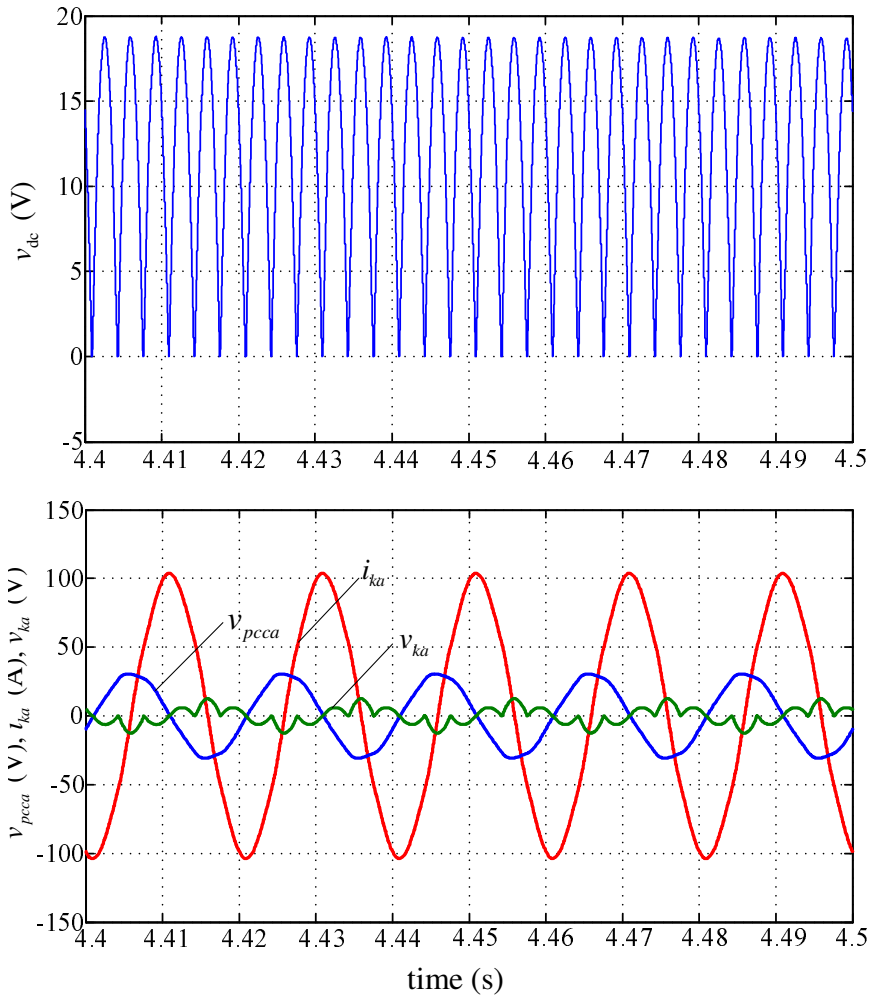

Figure 4.3: Waveforms of the converter after becoming unstable.

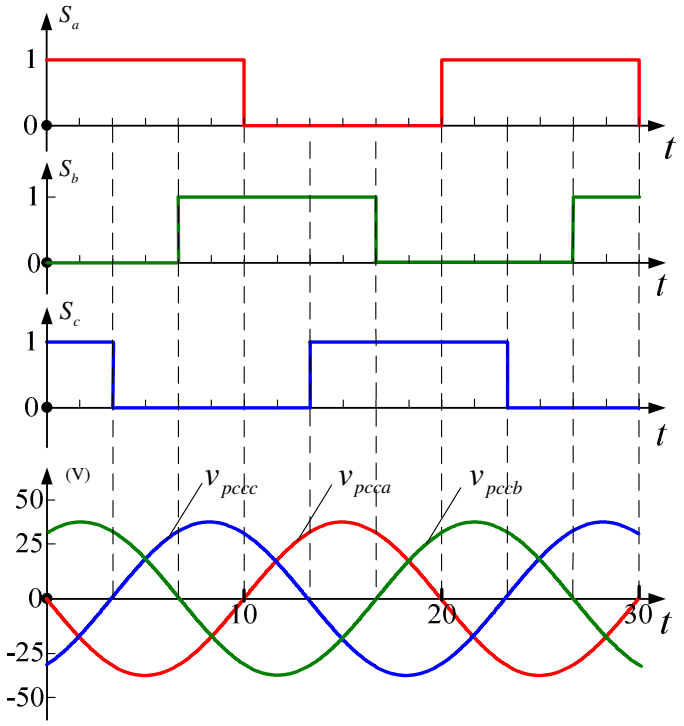

(a)

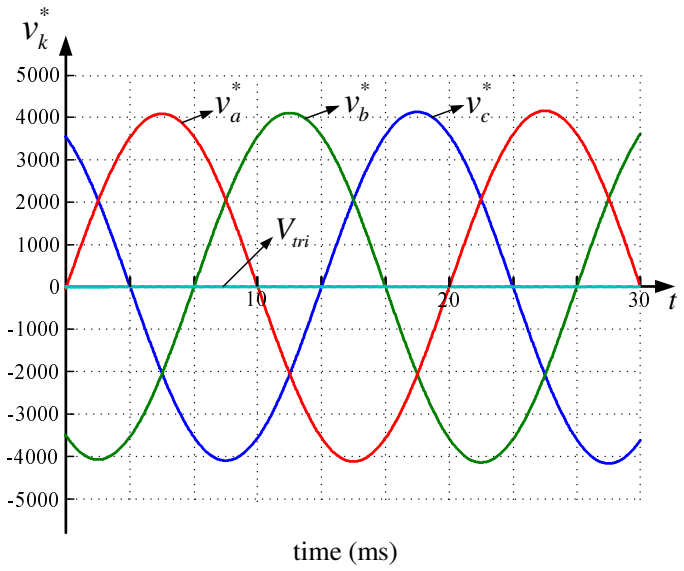

(b)

Figure 4.4: Switching signals and command signals of the converter after becoming unstable. (a) Switching signals of converter which is consistent with PCC voltages. (b) Command signals after getting into instability.

as shown in Chapter 3, which is not reversible by reducing the interacting load current. The large current can only be removed by shutting down the system.

4.2 Analysis of the Instability

4.2.1 System Operating Principle

In order to get a clear understanding of the instability phenomenon of the system, it is necessary to employ a suitable model for the power grid and to take adequate account of the operating characteristics of the rectifier. For a balanced three-phase system, the single-phase equivalent model shown in Fig. 4.5 is valid. Also, we can infer that the currents i_g, i_r and i_k have the same phase angle when the converter is working with unity power factor. From KVL and KCL, we get

$$\vec{V}_g = \vec{V}_{pcc} + \vec{V}_{L_g} \tag{4.1}$$

$$I_g = I_r + I_k \tag{4.2}$$

where $\vec{V}_g$, $\vec{V}_{pcc}$, and $\vec{V}_{L_g}$ are the vectors of v_{gx}, v_{pccx} and v_{L_gx} $(x = a, b, c)$; V_{L_g}, V_{pcc} and V_k are the rms values of v_{L_gx}, v_{pccx} and v_{kx}, respectively; and I_r, I_k and I_g are the root mean square (RMS) values of i_{rx}, i_{kx} and i_{gx}, respectively. From (4.1) and (4.2), we observe that the phase angle between $\vec{V_{pcc}}$ and $\vec{V_{L_g}}$ is exactly 90°. Furthermore, the magnitude relationship of parameters V_g, V_{pcc} and V_{L_g} can be represented by

$$V_g^2 = V_{pcc}^2 + V_{L_g}^2 \tag{4.3}$$

From the foregoing analysis, we readily see that the relationship of V_{L_g}, V_{pcc} and V_g in the grid side is linear. Also, P_{out} can be provided to the converter according to $P_{\text{out}} = 3P_o = 3V_{pcc}I_k$. Therefore, putting $V_{L_g} = \omega L_g I_g$, $V_{pcc} = RI_r$

and $P_{\text{out}} = 3P_o = 3V_{pcc}I_k$ to (4.2) and (4.3), we have

$$9(\omega L_g)^2 I_k^4 + \frac{6(\omega L_g)^2}{R} I_k^2 P_{\text{out}} + \left[1 + \left(\frac{\omega L_g}{R}\right)^2\right] P_{\text{out}}^2 = 9V_g^2 I_k^2 \quad (4.4)$$

where $\omega = 2\pi f$, and V_g is constant. Thus, P_{out} exhibits a maximum at $P_{\text{out,max}}$, i.e., the input active power of the converter is limited. In other words, the input current of converter I_k varies nonlinearly with the converter power P_{out}.

To find the maximum power $P_{\text{out,max}}$, we set $dP_{\text{out,max}}/dI_k = 0$, and use (4.4) to obtain

$$P_{\text{out,max}} = \frac{V_g^2 + (R^2 + (\omega L_g)^2)}{2(\omega L_g)^2} - \frac{\sqrt{(R^2 + (\omega L_g)^2)(R^2 + (\omega L_g)^2 + 2V_g^2 R)}}{2(\omega L_g)^2} \quad (4.5)$$

Thus, the system is stable if the load satisfies

$$P_{\text{in,ref}} = \frac{V_{\text{dc,ref}}^2}{R_L} \leq P_{\text{out,max}} \quad (4.6)$$

Here, the inductor power loss can be ignored since $R_s \approx 0$.

4.2.2 Transient to Instability

The three-phase active rectifier in the system can be represented by an average model under a sinusoidal pulse-width-modulation (SPWM) scheme. The fundamental component $\hat{v_k}$ at line frequency f of phase voltage v_{kx} (with $x = a, b, c$) is generated from the pulse-width-modulated output capacitor voltage v_{dc} using switch-pair S_x+ and S_x-. The switching signals of the switch-pair are generated by comparison of the sinusoidal phase voltage signal v_x^* ($x = a, b, c$) and the constant-magnitude triangular wave V_{tri}, as shown in Fig. 2.6. The operation characteristics of the PWM are shown in Fig. 4.6, where m is the modulation index (i.e., $m = \frac{v^*}{V_{\text{tri,peak}}}$). When $m \leq 1$, the orbit of the control signal v_k remains

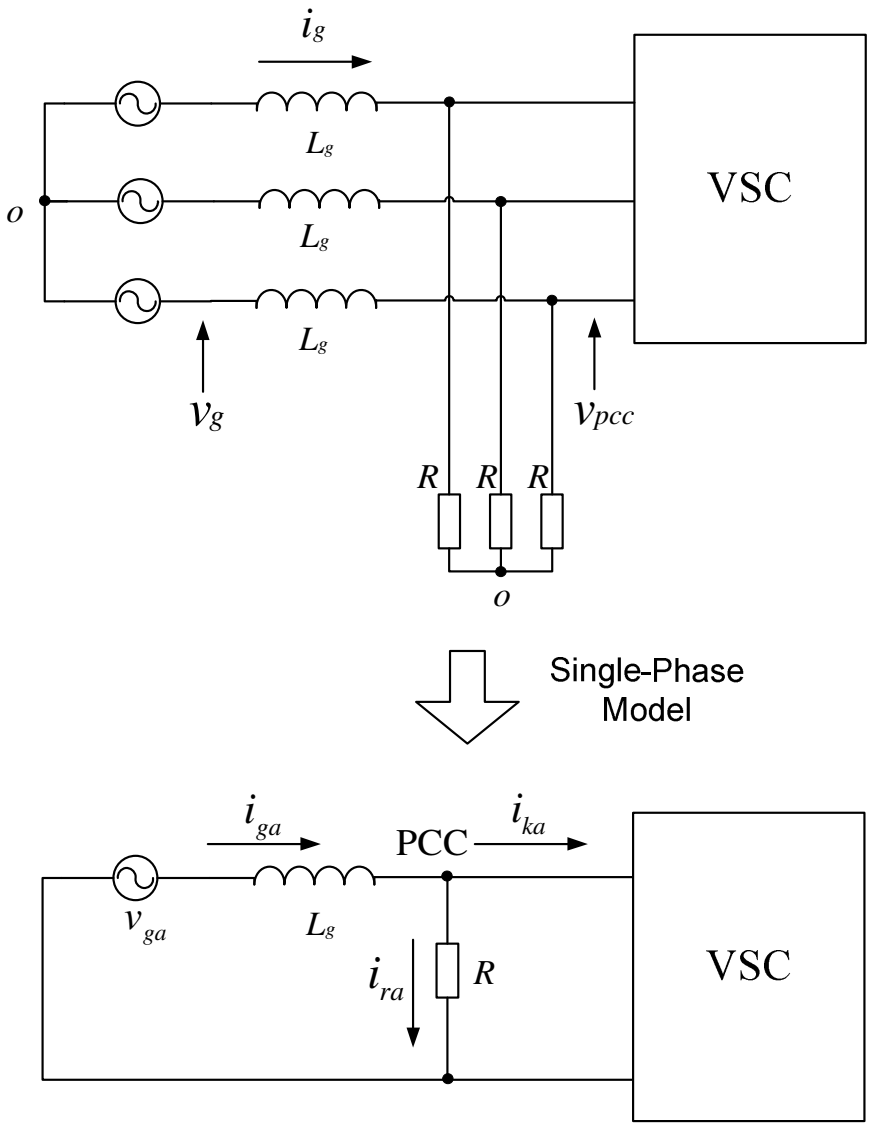

Figure 4.5: Single-phase equivalent model.

below the peak of the triangular carrier V_{tri}, and the relation between $\hat{v}_k$ and m (or v_k^*) can be considered linear, i.e.,

$$\hat{v}_k = \frac{v_{\text{dc}}}{2} m. \tag{4.7}$$

However, when $m > 1$, the peak of the command v_k^* exceeds the peak of the triangular carrier. Only the portion of v_k^* below the peak of the carrier is effective and the remaining part makes the duty cycle constant (1 or 0). Thus, the PWM

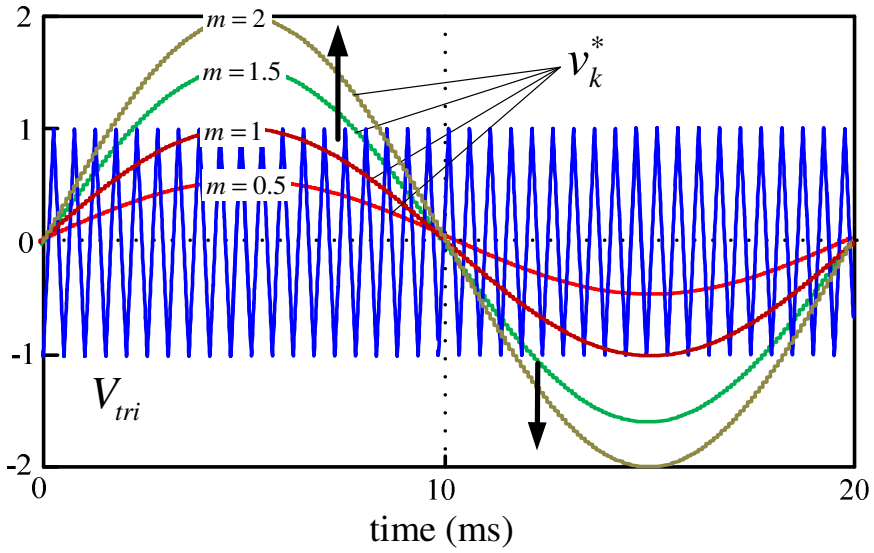

Figure 4.6: Voltage modulation signal v_k^* and carrier signal V_{tri}.

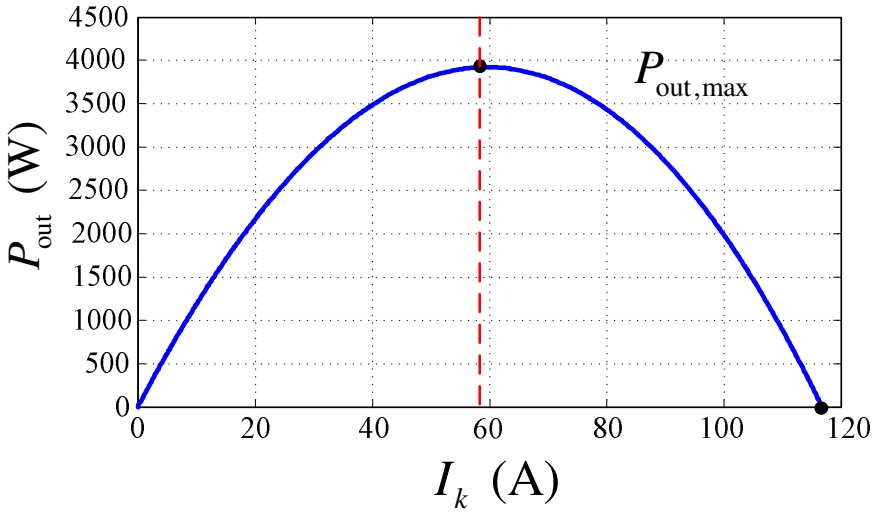

Figure 4.7: Active power P_{out} versus input current I_k.

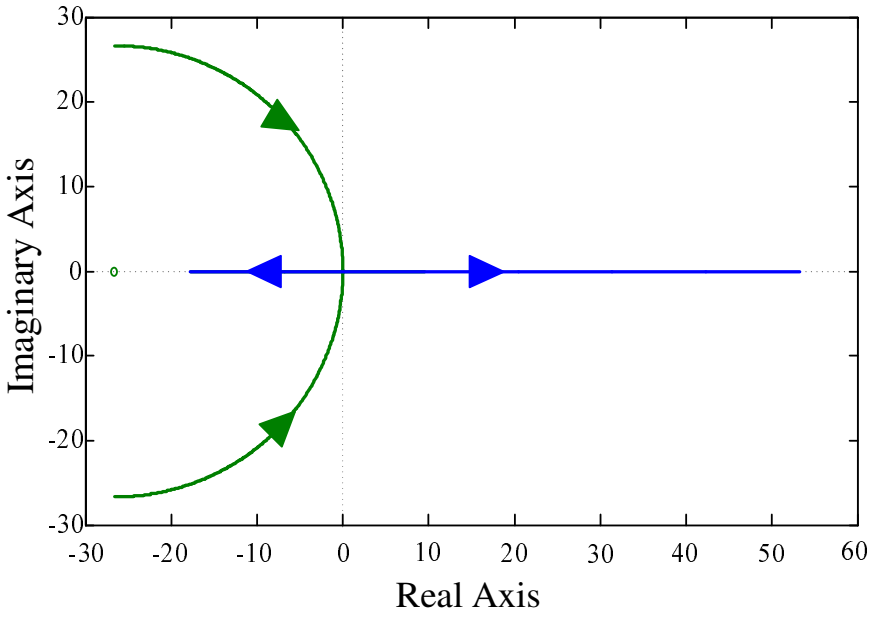

Figure 4.8: Locus of eigenvalues as I_k increases.

signal starts to drop pulses. As v_k^* becomes larger, the effective part becomes smaller, as shown in Fig. 4.6. Thus, the linearity between $\hat{v}_k$ and v_k^* no longer holds as shown in Chapter 2, and $\hat{v}_k$ becomes

$$\hat{v}_k = \frac{v_{\rm dc}}{\pi}\left(m\sin^{-1}\frac{1}{m} + \sqrt{1-\left(\frac{1}{m}\right)^2}\right). \tag{4.8}$$

The control signal v_k^* can be described as

$$v_k^* = \frac{2}{v_{\rm dc}} V_k^* \sin(\omega t + \theta_v) \tag{4.9}$$

where $\omega = 2\pi f$. Practically, since $\omega_s \gg \omega$, we can apply averaging to get

$$\overline{v_k} = \frac{v_{\rm dc}}{2}\frac{v_k^*}{V_{\rm tri,peak}} \tag{4.10}$$

where $V_{\rm tri,peak}$ is the peak value of $V_{\rm tri}$, $\overline{v_k}$ is the average value of v_k over a switching period $T_s = 2\pi/\omega_s$. Considering the fundamental component only, we write v_k for $\overline{v_k}$ subsequently to avoid confusion. From equations (4.7) and (4.8), the system

would work in the linear region when $v_k^* \leq \frac{v_{\rm dc}}{2}$.

Thus, using the average model, the three-phase boost rectifier can be modeled as

$$L\frac{di_{kx}}{dt} = v_{pccx} - R_s i_{kx} - v_{kx};\ \text{for } x = a, b, c \tag{4.11}$$

$$C\frac{dv_{\rm dc}}{dt} = i_o - \frac{v_{\rm dc}}{R_L}. \tag{4.12}$$

Employing synchronous reference frame transformation of three-dimensional vector, the system can be described in the $dq0$ rotating coordinate, i.e.,

$$L\frac{di_{kd}}{dt} = \omega L i_{kq} + v_{pccd} - R_s i_{kd} - v_{kd} \tag{4.13}$$

$$L\frac{di_{kq}}{dt} = -\omega L i_{kd} + v_{pccq} - R_s i_{kq} - v_{kq} \tag{4.14}$$

$$C\frac{dv_{dc}}{dt} = \frac{3}{2v_{\rm dc}}(v_{pccd} i_{kd} + v_{pccq} i_{kq}) - \frac{v_{\rm dc}}{R_L} \tag{4.15}$$

where subscripts d, q and 0 corresponds to the standard $dq0$ transformed variables and $i_0 = 0$ since the three-phase system is balanced. The i_{kd} and i_{kq} can represent the magnitude and phase respectively of i_{kx} $(x = a, b, c)$. The control of the converter is illustrated in Fig. 3.2, where equations (4.13) and (4.14) are used in the inner current loop and (4.15) is used in the outer voltage loop. The inner current loop aims to minimize the errors between the reference signals $(i_{d,\rm ref}, i_{q,\rm ref})$ and the sensed currents (i_{kd}, i_{kq}). The outer voltage loop is responsible for minimizing the voltage difference between $v_{\rm dc,ref}$ and $v_{\rm dc}$.

Based on the PI control of current loop in Fig. 3.2, the control voltages are shown as

$$v_d^* = v_{pccd} + \omega L i_{kq} - g_I(\Delta e_{id}) \tag{4.16}$$

$$v_q^* = v_{pccq} - \omega L i_{kd} - g_I(\Delta e_{iq}) \tag{4.17}$$

where $\Delta e_{id} = i_{d,\text{ref}} - i_{kd}$ and $\Delta e_{iq} = i_{q,\text{ref}} - i_{kq}$ are errors and $g_I(.)$ is the PI compensation function of the current loop. As described in Fig. 3.2, the control of the output voltage can also be given as

$$i_{d,\text{ref}} = g_V(\Delta e_v) = K_{vp}\Delta e_v + K_{vi}\int_0^t \Delta e_v dt \tag{4.18}$$

where $\Delta e_v = v_{\text{dc,ref}} - v_{\text{dc}}$ is the error and $g_V(.)$ is the PI control function of the voltage loop. Fortunately, the exact dynamics of the current control loop are not crucial in explaining the irreversible instability observed here, since the inner current loop is much faster than the outer voltage loop. Moreover, since the currents i_{kd} and i_{kq} can closely follow the reference, the relation $i_{kq} = i_{q,\text{ref}} = 0$ holds, and the rectifier is still working with unity power factor even when the converter is transiting to instability, as shown in Fig. 4.2(b). Thus, we may analyze the cause of instability using (4.4).

To simplify the analysis, resistive losses in series with inductors are ignored since $R_s \approx 0$. Applying the power balance (4.19), and using (4.4) (i.e., $i_{kd} = \sqrt{2}I_k$), the current transfer function (4.20) can be obtained.

$$P_{\text{in}} = P_{\text{out}} = v_{\text{dc}} i_o \tag{4.19}$$

$$P_{\text{out}} = f(i_{kd}) = 3i_{kd}\frac{-(\omega L_g)^2 i_{kd} + R\sqrt{2V_g^2(R^2 + (\omega L_g)^2) - (\omega L_g)^2 R^2 i_{kd}^2}}{2(R^2 + (\omega L_g)^2)} \tag{4.20}$$

Combining (4.12), (4.18), (4.19) and (4.20), and ignoring the fast dynamics of the current loop (i.e., assuming $i_{kd} = i_{d,\text{ref}}$), the voltage loop gain state equation is obtained as follows:

$$C\frac{d\Delta e_v}{dt} + \frac{f(g_v(\Delta e_v))}{v_{\text{dc}}} - \frac{v_{\text{dc}}}{R_L} = 0 \tag{4.21}$$

Thus, the characteristic equation can be obtained as

$$\lambda^2 + \frac{1}{Cv_{\mathrm{dc,ref}}}\frac{df}{di_{kd}}(K_{vp}\lambda + K_{vi}) = 0. \tag{4.22}$$

To study the system's stability using the characteristic equation, we use the parameters listed in Tables I and II, with $L_g = 3$ mH and $R = 0.4\Omega$. Using (4.4), we obtain the characteristic shown in Fig. 4.7. Furthermore, $\frac{df}{di_{kd}} > 0$ when $P_{\mathrm{in,ref}} < P_{\mathrm{out,max}}$, and the roots of (4.22) are negative, which means that the system is stable. On the contrary, as the input active power increases exceeding $P_{\mathrm{out,max}}$, i.e., $P_{\mathrm{in,ref}} > P_{\mathrm{out,max}}$, the converter would still make its active current i_{kd} increase beyond the point $P_{\mathrm{in,ref}} = P_{\mathrm{out,max}}$ while the grid can no longer provide enough power. Thus, the input active power would collapse as the current increases, i.e., $\frac{df}{di_{kd}} < 0$, and the converter is unstable as the roots of the characteristic equation are real with $\lambda_1 < 0, \lambda_2 > 0$. The root locus is illustrated in Fig. 4.8. Therefore, from the analysis above, it can be observed that Δe_v will increase (i.e., $\Delta e_v > 0$).

4.2.3 Unstable Operation

From Fig. 4.7, active current I_k also exhibits a maximum at $I_{k,\mathrm{max}}$, i.e., the input active current i_{kd} of the converter has been limited by the grid since $i_{kd} = \sqrt{2}I_k$. From (4.4), the maximum active current $i_{kd,\mathrm{max}}$ is

$$i_{kd,\mathrm{max}} = \sqrt{2}\frac{V_g}{\omega L_g}. \tag{4.23}$$

However, from the outer loop analysis, Δe_v will get larger, and the $i_{d,\mathrm{ref}}$ has not been limited. Also, based on (4.18) and (4.21), the time derivative of $i_{d,\mathrm{ref}}$ can be

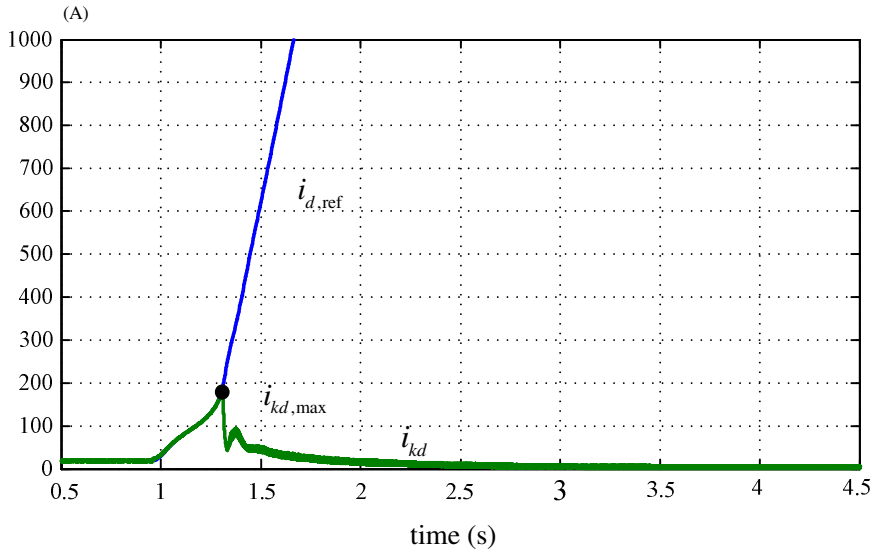

Figure 4.9: Reference current $i_{d,\mathrm{ref}}$ versus active current i_{kd}.

written as

$$\frac{di_{d,\mathrm{ref}}}{dt} = K_{vp}\frac{d\Delta e_v}{dt} + K_{vi}\Delta e_v > 0. \tag{4.24}$$

From (4.24), the current i_{kd} could not follow the reference value $i_{d,\mathrm{ref}}$ after crossing the point $i_{d,\mathrm{ref}} = i_{kd,\mathrm{max}}$, i.e., $\Delta e_{id} > 0$, as shown in Fig. 4.9. Also, we can get $\lim_{t\to+\infty} g(\Delta e_{id}) = +\infty$ from (4.24) since i_{kd} is limited within $(0, i_{kd,\mathrm{max}})$. Combining with (4.16), we get

$$\lim_{t\to+\infty} v_d^* = -\infty \tag{4.25}$$

Thus, $\lim_{t\to+\infty} V^* = \lim_{t\to+\infty}\sqrt{v_d^{*2} + v_q^{*2}} = +\infty \gg v_{\mathrm{dc}}$. From the analysis above, the system works in the nonlinear region when $V_k^* > \frac{v_{dc}}{2}$. But the fundamental component phase angle θ_v is still decided by the values of v_d^* and v_q^* using (4.8).

At the AC side of converter, using the equivalent circuit and ignoring the inductor resistance ($R_s \approx 0$), the vector equation can be obtained as

$$\dot{V}_{pcc} = \dot{V}_k + j\omega L\dot{I}_k \tag{4.26}$$

where $\dot{V}_{pcc} = v_{pccd} + jv_{pccq}$, $\dot{I}_k = i_{kd} + ji_{kq}$, and $\dot{V}_k = v_{kd} + jv_{kq}$. Solving this equation yields

$$\begin{cases} i_{kd} = \frac{1}{\omega L}(v_{pccq} - V_k \sin\theta) \\ i_{kq} = -\frac{1}{\omega L}(v_{pccd} - V_k \cos\theta) \end{cases} \tag{4.27}$$

where $V_k = \sqrt{v_{kd}^2 + v_{kq}^2} \leq \frac{v_{\mathrm{dc}}}{2}$ and $\sin\theta = \frac{v_q^*}{V_k^*}$, $\cos\theta = \frac{v_d^*}{V_k^*}$. Combining (4.25) and (4.27), we get $i_{kq} < 0$. Also, the value of i_{kq} is limited within $(-\frac{v_{pccd}+V_k}{\omega L}, -\frac{v_{pccd}}{\omega L})$, while $i_{q,\mathrm{ref}} = 0$. Similar to the d-axis, we have

$$0 < \frac{v_{pccd}}{\omega L} \leq \Delta e_{iq} \leq \frac{v_{pccd} + V_k}{\omega L} \tag{4.28}$$

$$\lim_{t\to+\infty} v_{pccq}^* = -\infty \tag{4.29}$$

Putting (4.27) and (4.28) in (4.16) and (4.17), we have

$$\lim_{t\to+\infty} \frac{v_q^*}{v_d^*} = \lim_{t\to+\infty} \frac{g(\Delta e_{iq})}{g(\Delta e_{id})} = 0 \tag{4.30}$$

Therefore,

$$\lim_{t\to+\infty} \sin\theta = \lim_{t\to+\infty} \frac{v_q^*}{V_k^*} = 0 \tag{4.31}$$

$$\lim_{t\to+\infty} \cos\theta = \lim_{t\to+\infty} \frac{v_d^*}{V_k^*} = -1 \tag{4.32}$$

It could be inferred that the phase shift of the switching signal approaches 180° relative to the input line voltage v_{pccx} from (4.31) and (4.32), as shown in Fig. 4.4. So, the phase shift of the voltage $v_{kx}(x = a, b, c)$ relatives to the input line voltage $v_{pccx}(x = a, b, c)$ also approaches 180°.

Thus, as $t \to +\infty$, the values of (i_{kd}, i_{kq}) can be written as

$$\lim_{t\to+\infty} i_{kd} = 0 \tag{4.33}$$

$$\lim_{t\to+\infty} i_{kq} = -\frac{1}{\omega L}(v_{pccd} + V_k) \tag{4.34}$$

From the analysis above, it can be shown that the operating state cannot return to the stable state by changing the parameters and the only way to remove instability is by resetting the rectifier.

4.2.4 Analysis of Instability

After the system gets into the irreversible instability, the closed-loop control ceases to work. From (4.25) and (4.29), theoretically, the control loop pushes the command modulation signals under dq-axis toward negative infinity. This will result in the line current saturating at (4.33) and (4.34) due to device limitations. Meanwhile, the active power P_{out} and reactive power Q_{out} of the converter can be rewritten in the dq coordinate as

$$P_{out} = \frac{3}{2}(v_{pccd} i_{kd} + v_{pccq} i_{kq}) \tag{4.35}$$

$$Q_{out} = \frac{3}{2}(v_{pccd} i_{kq} - v_{pccq} i_{kd}) \tag{4.36}$$

Therefore, combining equations (4.33), (4.34), (4.35) and (4.36), we get

$$\lim_{t\to+\infty} P_{out} = 0 \tag{4.37}$$

$$\lim_{t\to+\infty} Q_{out} = -\frac{3}{2\omega L}(v_{pccd}^2 + V_k v_{pccd}) \tag{4.38}$$

From the above equations, it can be shown that after the system getting into irreversible instability, the active power supplied to the converter would drop to zero while the reactive power would expand to very large value. There is not

enough active power to sustain the DC output in the resistive load. The DC output voltage begins to drop. However, the control loop fails to narrow the gap between the voltage reference and the DC output voltage. It can only push the command signals v_d^* and v_q^* toward negative infinity which will cause the output voltage to reach 0 V finally.

The rectifier does not work with unity power factor, but rather work with zero power factor. The system gets into the final unstable state and the reactive power expands at this point. The converter works with significant reactive power transferred from the grid.

Meanwhile, as the dq-axis command signals v_d^* and v_q^* are being pushed to negative infinity, the abnormal v_d^* and v_q^* make the command signal v_k^* increase beyond the peak of the triangular carrier wave. When v_k^* becomes very large, the expanded command signals only intersect with the carrier wave at the line frequency. Moreover, we observe that the switching signals when the modulation index is limited (i.e., $m \leq 1$) would also vary at line frequency since the duty cycle of the switching signals is only determined by the intersection of the command signals and the triangular carrier. The power switches are thus only switched at the line frequency regardless of the modulation index being limited or not.

4.2.5 Derivation of Stability Boundary

From the analysis above, we can get the precise stability boundary analytically from (4.5) and applying $P_{\text{in}} = 3I_k^2 R_s + \frac{v_{dc,\text{ref}}^2}{R_L}$ at the boundary point ($P_{\text{in}} = P_{\text{out,max}}$). It can be readily shown that the theoretical boundary of stability is

given by

$$\begin{aligned} & 4(\omega L_g)^4 R^2 (\frac{3V_g^2 R}{2(\omega L_g)^2} - \frac{v_{dc,\text{ref}}^2}{R_L})^2 \\ & - 12(\omega L_g)^2 V_g^2 [R^2 + (\omega L_g)^2](R + R_s)(\frac{3V_g^2 R}{2(\omega L_g)^2} - \frac{v_{dc,\text{ref}}^2}{R_L}) \\ & + 9[R^2 + (\omega L_g)^2] V_g^4 (R + R_s)^2 = 0. \end{aligned} \tag{4.39}$$

The above analytical result will be used in the next section for comparison with simulation results.

4.3 Simulation Verification

In this section, we provide computer simulation results to verify the analytical findings. Our simulations can be regarded as a viable form of verification as the simulation model is the exact original physical system. In our simulations, the boundaries of stability in the parameter space [116] are actually found by simulating the system under different parameter sets and observing the steady-state behavior for each set of parameters. Comparison of the analytical stability boundaries and those found by numerical simulations are shown in Fig. 4.10. From the results, we conclude that the analytical findings are in perfect agreement with the simulations since the model for power balance and power limitation here can be very precise. Moreover, the effect of variations of parameters V_g, L_g and R_L, R on the stability boundary given in (4.39) can be visualized in Fig. 4.10. Here, since the converter can be regarded as a constant power load (i.e., $R_s \approx 0$), the effects of parameter $v_{\text{dc,ref}}$ on the boundary can be inferred from the stability boundary with the parameter R_L using $v_{\text{dc,ref}} = \sqrt{P_{\text{in}} R_L}$.

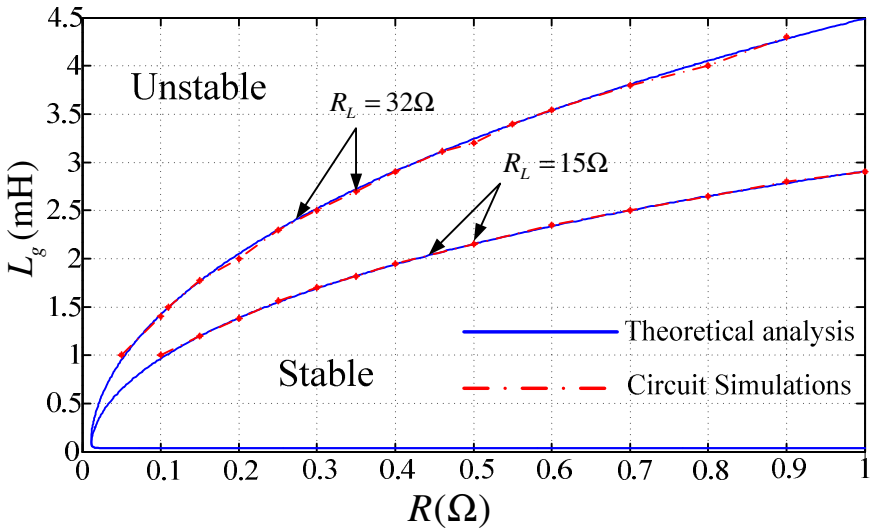
Unstable
$R_L = 32\Omega$
$R_L = 15\Omega$
Stable
Theoretical analysis
Circuit Simulations
L_g (mH)
$R(\Omega)$

(a)

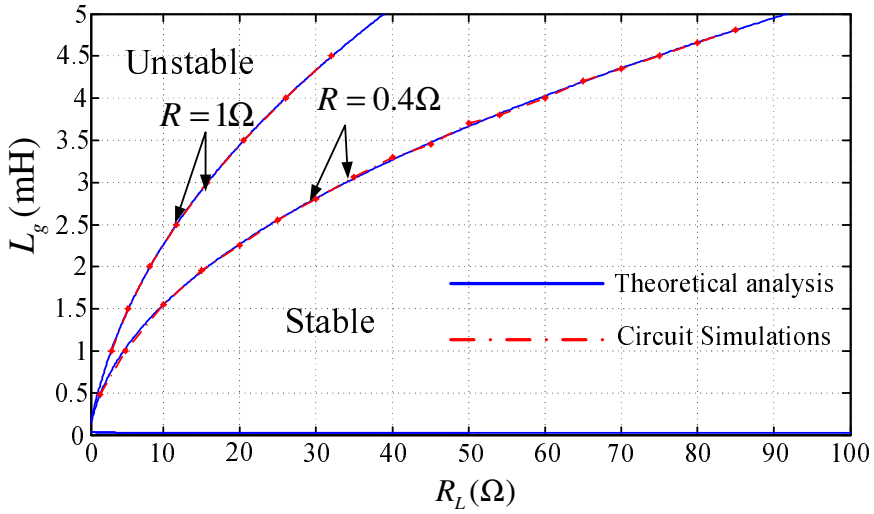
Unstable
$R = 1\Omega$
$R = 0.4\Omega$
Stable
Theoretical analysis
Circuit Simulations
L_g (mH)
$R_L(\Omega)$

(b)

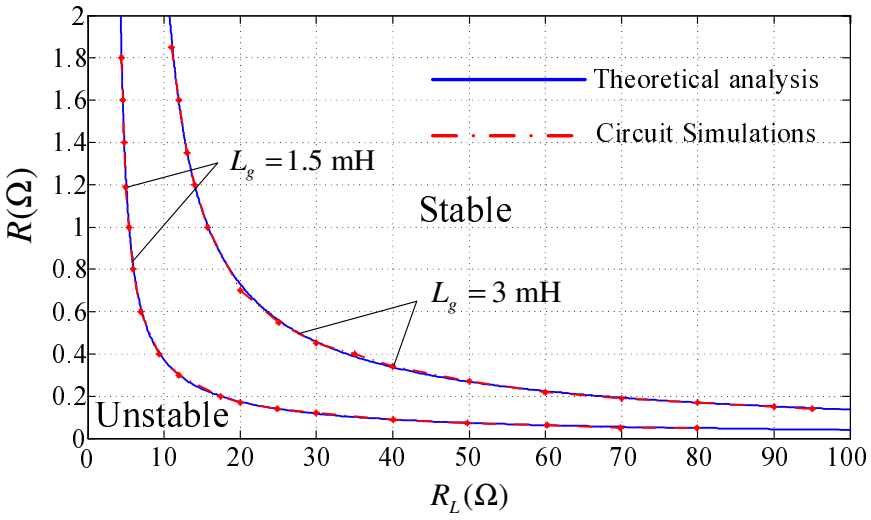
Theoretical analysis
Circuit Simulations
$L_g = 1.5$ mH
Stable
$L_g = 3$ mH
Unstable
$R(\Omega)$
$R_L(\Omega)$

(c)

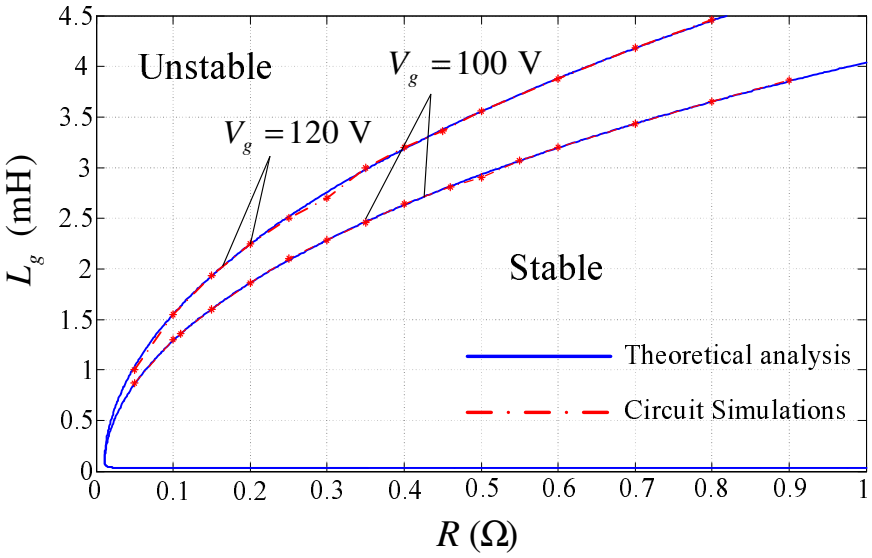

(d)

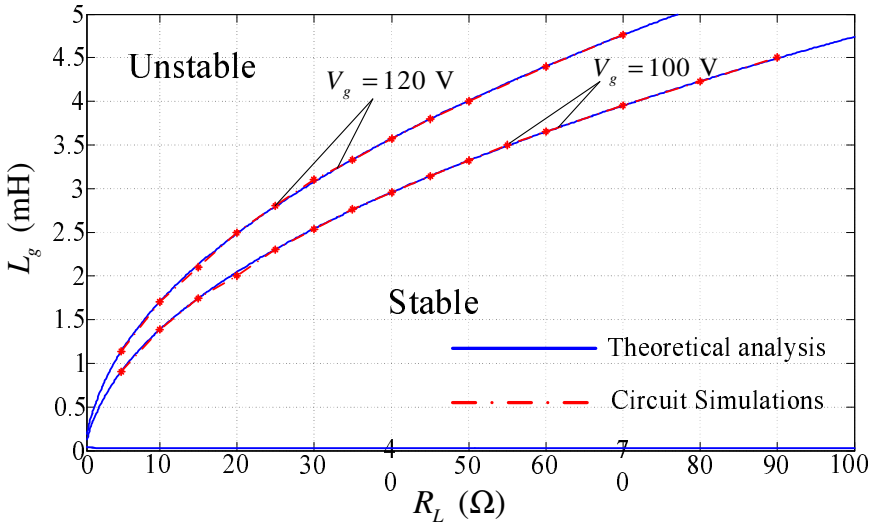

(e)

Figure 4.10: Stability boundaries by analysis and simulations. (a) Boundaries of stability in the parameter space of R and R_L for $L_g = 1.5$ mH and $L_g = 3$ mH with $V_g = 110$ V. (b) Boundaries of stability in the parameter space of R and L_g for $R_L = 15\ \Omega$ and $R_L = 32\ \Omega$ with $V_g = 110$ V. (c) Boundaries of stability in the parameter space of L_g and R_L for $R = 1\ \Omega$ and $R = 0.4\ \Omega$ with $V_g = 110$ V. (d) Boundaries of stability in the parameter space of L_g and R for $V_g = 100$ V and $V_g = 120$ V with $R = 0.4\ \Omega$. (e) Boundaries of stability in the parameter space of L_g and R_L for $V_g = 100$ V and $V_g = 120$ V with $R_L = 32\ \Omega$ under the control parameters $K_{vp} = 0.1, K_{vi} = 8, K_{ip} = 6, K_{ii} = 100$.

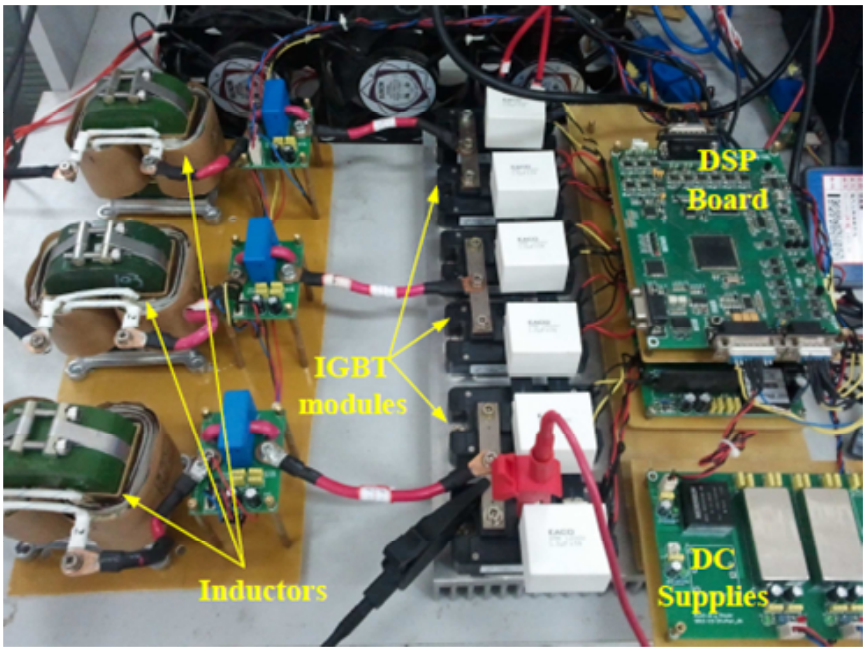

Figure 4.11: Experiment platform for demonstrating irreversible instability.

4.4 Experimental Verification

To verify the nonlinear phenomenon observed in the foregoing sections, we have constructed an experimental system in our laboratory. The complete control has been implemented on a DSP board according to the control function shown in Fig. 3.2. The DSP processor TI TMS320F2812 was employed with the sampling rate of the control board set at 20 kHz. The IGBT modules used in experiment were connected in parallel, and adopted a symmetric PWM modulation at 10 kHz switching frequency applied to the control signals. The experimental platform is shown in Fig. 4.11. A three-phase voltage regulator has been used as the grid voltage V_g in the experiment. The experimental parameters are listed in Tables 4.1 and 4.2 with $L_g = 3$ mH and $R = 0.4\ \Omega$.

Figure 4.12 shows the input voltage and line current before the system crosses the stability boundary. Figure 4.13 shows the instability phenomenon when the interacting load R is connected to the PCC which is similar with the simulation in Fig. 4.2 (b). The transient stages to instability are shown in Figs. 4.13 (b) and

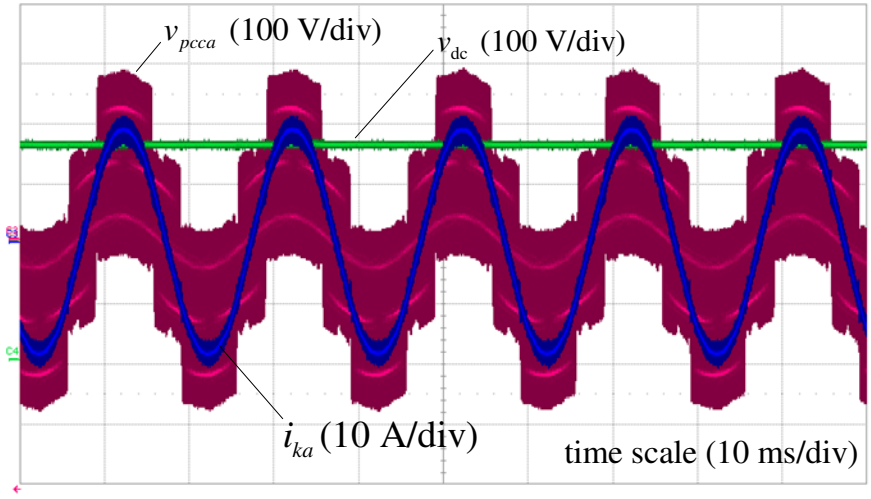

Figure 4.12: Waveforms of $v_{pcca}, i_{ka}, v_{\mathrm{dc}}$ under stable operation.

(c). It can be observed that the converter still works in unity power factor before going to the unstable operation. Figure 4.14 presents the waveforms of v_{pcca}, i_{ka}, and v_{dc} after the system enters the unstable region. It can be shown that the line input current i_{ka} expands to a very high value, and the output voltage v_{dc} drops to a value which is very close to zero. Moreover, the boost rectifier works in the instability region with excessive reactive power absorbed from the power grid while little active power is processed. Since the voltage regulator used in the experiment has a non-zero output impedance, the maximum value of current i_{ka} is a little smaller than the one in the simulation shown in Fig. 4.3. Nonetheless, the experimental results adequately verify the phenomenon as explained in Section 4.2.

4.5 Summary

Three-phase boost power rectifiers connecting to a non-ideal power grid with interacting loads represent a practical form of system configuration. This kind of practical system configurations has been rarely studied in their original form, and in most previous studies, ideal conditions and simplifying assumptions were

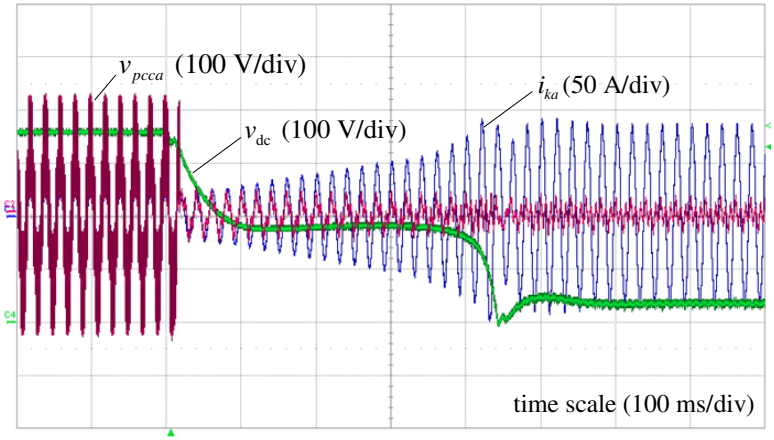

(a)

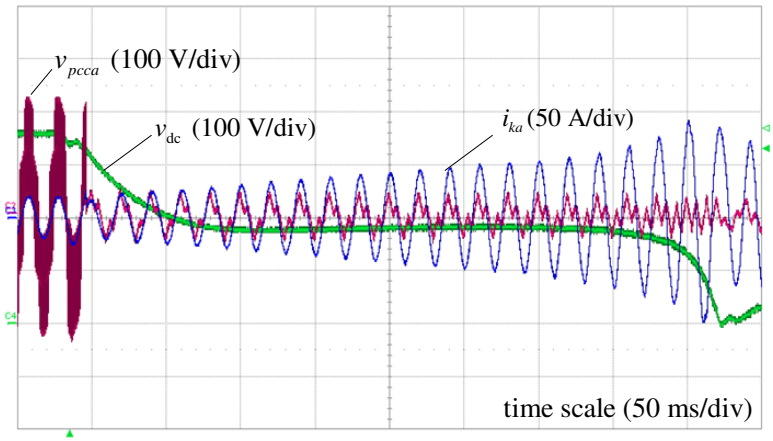

(b)

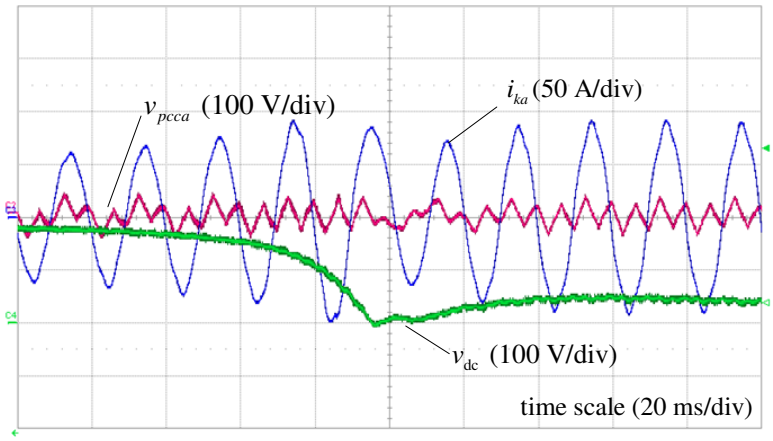

(c)

Figure 4.13: Instability phenomena caused by improper grid impedance and presence of interacting load. (a) Waveforms of v_{pcca}, i_{ka} and v_{dc} showing the transition to unstable operation. (b) Waveforms showing the early stage of the transient to unstable operation. (c) Waveforms showing the later stage of transient.

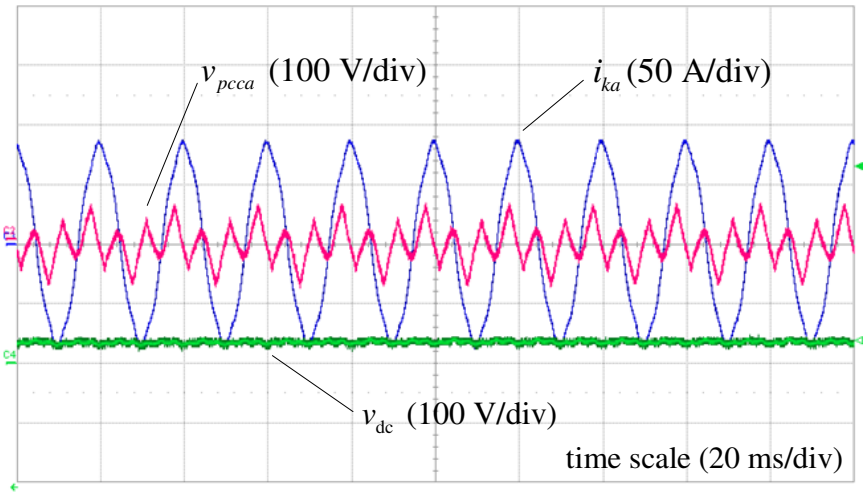

Figure 4.14: Waveforms of $i_{ka}, v_{pcca}, v_{\mathrm{dc}}$ when the converter enters the instability.

made, which often provide incomplete information for the design of the control functions and for the choice of parameters. In this chapter, we study the stability of such grid-connected load-interacting converter systems, and identify an irreversible bifurcation phenomenon. Due to the limited input active power given to the rectifier by the power grid, the DC voltage of the converter will drop when the converter fails to get the power it needs. The converter then sinks reactive power and operates "abnormally". This chapter gives a detailed analysis of the control system failure and the cause of instability. Numerical simulation results have verified the theoretically found stability boundaries. Also, experimental measurements provide verification of the instability phenomenon. Our study clearly illustrates how stability could be affected by variation of power grid parameters. The result provides useful design information regarding the choice of operating parameters that would ensure proper stable operation [120, 121].

Chapter 5

Low-Frequency Hopf Bifurcation

For a VSC connecting to an ideal power grid, the converter is generally regulated with an outer voltage loop which operates in conjunction with a sinusoidal pulse-width-modulated (SPWM) inner current loop. However, in practice, the grid impedance is varying, depending on the location where the converter is connected. The converter connecting to a stiff grid is well understood and designed. Nevertheless, in the weak section of the grid, a significant grid impedance exists while the design of the control loop still assumes an ideal power grid. The mismatch between the practical grid condition and the ideal control assumption will pose a stability issue and may cause harmonic oscillation to occur. The grid stability could be affected by an improper control of the converter. The harmonic current is also an issue of power quality.

The three-phase VSC is connected to the power grid at the point of common coupling (PCC). Under such a situation, the system can be represented by the structure shown in Fig. 5.1. In this Chapter, the value of local interacting load can be set extremely high which may not affect the operation of the VSC. For an ideal power grid, the grid voltage is regarded as an AC voltage source with zero source impedance. In this system, the grid impedance is mostly inductive in practice, as represented by L_g and R_g. The converter is connected to the grid

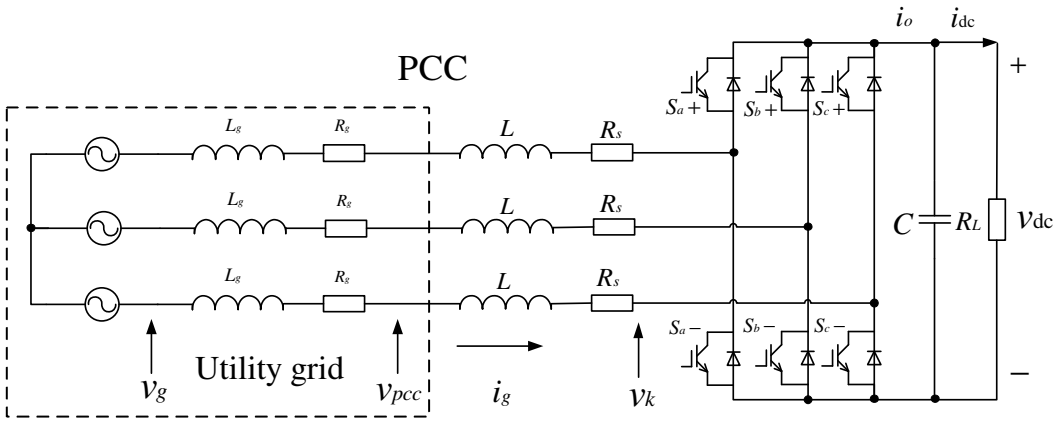

Figure 5.1: Three-phase voltage source converter connecting to non-ideal power grid.

at PCC. Although the converter is properly designed, the grid impedance may interact with the converter, and makes the system unstable. However, the effects of the grid impedance on the control design of three-phase VSC, despite their practical importance, have been rarely discussed.

5.1 A Glimpse at Low-Frequency Instability

An initial probe into the behavior of the system is conducted using a MatLab implementation of the circuit of Fig. 5.1. The control of VSC is implemented by a dual-loop proportional-integral (PI) control, which is same as the control scheme mentioned in Chapter 3. The system parameters used in the simulation are shown in Tables 5.1 and 5.2. Here, L_g and R_g represent the grid impedance, and the total resistance at the grid side is about 0.2 Ω. The inductance of the grid side is varying from 1 nH to 12 mH. In practice, the rectifier circuit can provide a regulated voltage of 360 V at a rated output power of 4 kW for a load of $R_L = 32$ Ω.

Figure 5.2 (a) shows the transient waveforms of the PFC power supply connecting to a non-ideal power grid with inductance $L_g = 12$ mH and resistance $R_g = 0.2$ Ω. Normally, a 300 Hz ripple on the DC output of three-phase PFC

Table 5.1: Parameters of non-ideal power grid.

$v_{ga,gb,gc}$	f	L_g	R_g
110 Vrms	50 Hz	1 nH–12 mH	0.2 Ω

Table 5.2: Circuit parameters of the three-phase voltage source converter.

$V_{dc,\text{ref}}$	R_s	L	C	R_L	f_s
360 V	0.2 Ω	3 mH	1.5 mF	90 Ω	10 kHz

power supply is expected. However, with a non-ideal power grid, a low-frequency oscillation at 150 Hz is observed and can be identified as having emerged from a Hopf-type bifurcation. We observe that the system oscillates at 150 Hz, despite the choice of PI parameters being within the stable range. At the same time, large amount of harmonics emerge on the line current. The phase portrait of the system beyond the Hopf bifurcation is shown in Fig. 5.2 (b), where the red orbit indicates the phase portrait when $L_g = 6$ mH, and the blue expanded phase portrait corresponds to $L_g = 12$ mH.

Figure 5.3 shows the process of the VSC losing stability. The grid impedance L_g is set to 9 mH. The system works in the stable region at the beginning of the simulation. However, as the load current increases, the system becomes unstable. As the load current gets higher, the system exhibits Hopf bifurcation initially (about 0.6 s to 0.65 s), with the DC output oscillating and harmonics emerging from the line current. Then, the system enters catastrophic bifurcation (at around 0.65 s), which is an irreversible instability that cannot be recovered by reducing the load current [51, 116, 117]. The phenomenon clearly shows how the VSC loses stability in the presence of a non-ideal power grid. It has been found that Hopf bifurcation does not occur with an ideal power grid, and the VSC enters the catastrophic bifurcation directly. However, with a non-ideal power grid, the system will exhibit a Hopf-type bifurcation even if the VSC is properly designed. In the sequel, we will probe into details of this low-frequency bifurcation and its interaction with the previously found catastrophic bifurcation.

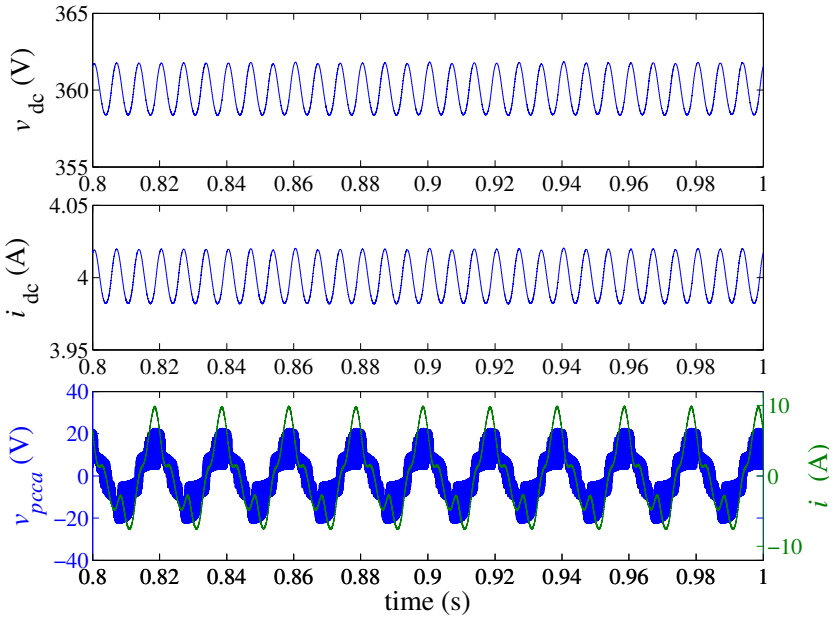

(a)

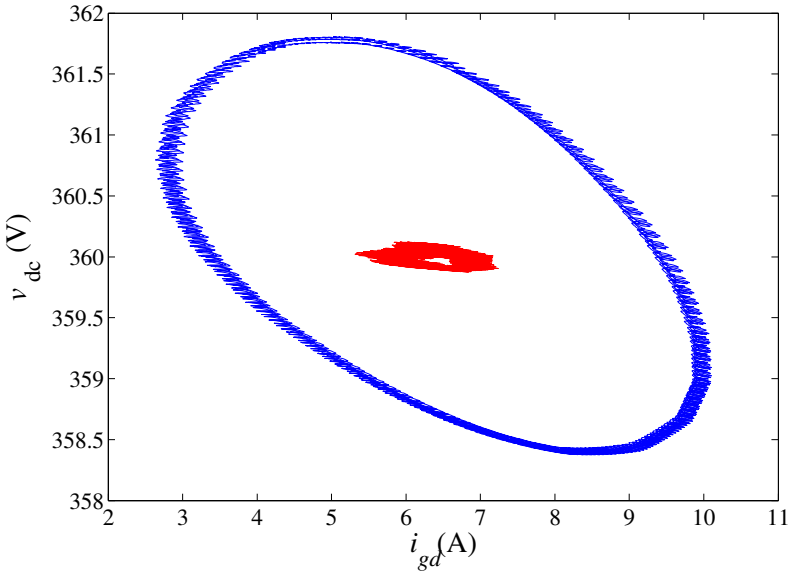

(b)

Figure 5.2: (a) Low-frequency oscillation and (b) phase portrait before (red) and after (blue) Hopf bifurcation when the three-phase voltage source converter is connected to non-ideal power grid, red: $L_g = 6$ mH, blue: $L_g = 12$ mH.

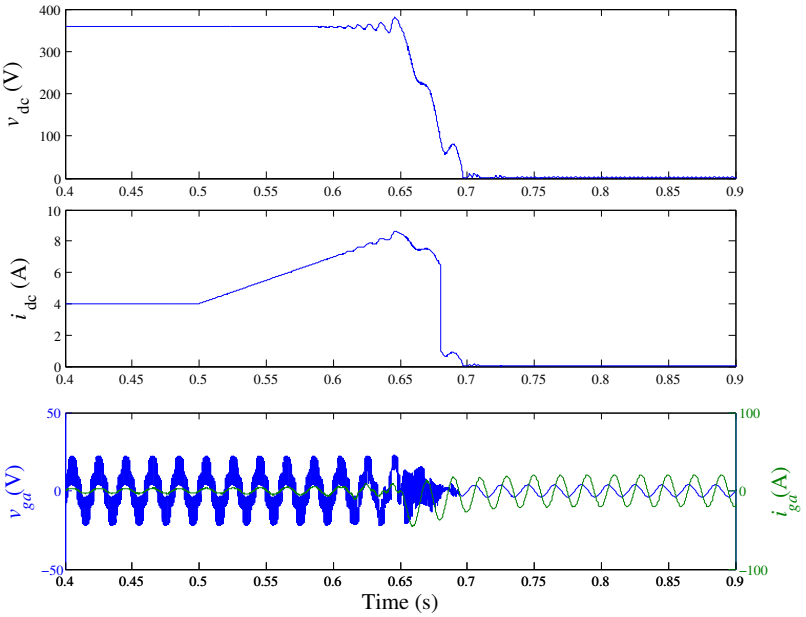

Figure 5.3: The system enters catastrophic bifurcation after going through Hopf bifurcation with rising load current with grid impedance $L_g = 9$ mH and $R_g = 0.2\ \Omega$.

5.2 Analysis of the Grid-Connected System

The working principle of VSC can be represented by an averaged model. In this section, the averaged model will be applied to study the effect of grid impedance [59, 122]. Note that when there is no grid impedance ($L_g = 0$ mH, $R_g = 0\ \Omega$), the model resembles the average model of VSC connected to an ideal grid. Assuming that the SPWM is working in the linear region, we have

$$L\frac{di_{gx}}{dt} = -R_s i_{gx} + v_{pccx} - v_{kx} \tag{5.1}$$

$$C\frac{dv_{\rm dc}}{dt} = \sum_{x=a,b,c} i_{gx} n_{kx}(t) - i_{\rm dc} \tag{5.2}$$

where

$$n_k(t) = \frac{v_k*}{V_{tri,\rm peak}} \tag{5.3}$$

with v_k* being the voltage command signal and $V_{tri,\text{peak}}$ the peak of SPWM triangle waveform.

In order to facilitate the incorporation of the control, we transform the system to the dq rotating coordinate, i.e.,

$$L\frac{di_{gd}}{dt} = \omega L i_{gq} - R_s i_{gd} + v_{pccd} - v_{kd} \tag{5.4}$$

$$L\frac{di_{gq}}{dt} = -\omega L i_{gd} - R_s i_{gq} + v_{pccq} - v_{kq} \tag{5.5}$$

$$C\frac{dv_{\text{dc}}}{dt} = \frac{3}{2v_{\text{dc}}}(v_{kd}i_{gd} + v_{kq}i_{gq}) - i_{\text{dc}} \tag{5.6}$$

where subscripts d, q and 0 correspond to the standard d-q-0 transformed variables. Also, i_{gd} and i_{gq} can be used to represent the magnitude and phase, respectively, of i_{gx}, where $x = a, b, c$. Equations (5.4) and (5.5) are used in the inner-current loop and (5.6) is used in the outer-voltage loop. The variables $v_{pccd,q}$ is used to represent the voltage at PCC in the dq-axis.

The line currents stay the same on both the grid side and the converter side. Thus, i_{gd}, i_{gq} should also satisfy the following equations:

$$L_g\frac{di_{gd}}{dt} = v_{gd} - v_{pccd} - R_g i_{gd} + \omega L_g i_{gq} \tag{5.7}$$

$$L_g\frac{di_{gq}}{dt} = v_{gq} - v_{pccq} - R_g i_{gq} - \omega L_g i_{gd} \tag{5.8}$$

Hence, the line voltage at the PCC can be represented as

$$v_{pccd} = \frac{Lv_{gd} - LR_g i_{gd} + L_g(R_s i_{gd} + v_{kd})}{L_g + L} \tag{5.9}$$

$$v_{pccq} = \frac{Lv_{gq} - LR_g i_{gq} + L_g(R_s i_{gq} + v_{kq})}{L_g + L} \tag{5.10}$$

First, we will complete the system's state equations. For the outer voltage

loop, we have

$$\frac{dx_1}{dt} = V_{\text{dc,ref}} - v_{\text{dc}} \tag{5.11}$$

$$i_{d,\text{ref}} = K_{vp}(V_{\text{dc,ref}} - v_{\text{dc}}) + K_{vi}x_1 \tag{5.12}$$

For the inner current loop, we have

$$\frac{dx_2}{dt} = i_{d,\text{ref}} - i_{gd} \tag{5.13}$$

$$v_{kd} = v_{pccd} + \omega L i_{gq} - K_{ip}(i_{d,\text{ref}} - i_{gd}) - K_{ii}x_2 \tag{5.14}$$

$$\frac{dx_3}{dt} = I_{q,\text{ref}} - i_{gq} \tag{5.15}$$

$$v_{kq} = v_{pccq} - \omega L i_{gd} - K_{ip}(I_{q,\text{ref}} - i_{gq}) - K_{ii}x_3 \tag{5.16}$$

It is obvious that $v_{pccd,q}$ is not ideal in a grid-connected converter system. Thus, the expression of $v_{kd,q}$ should be

$$v_{kd} = v_{gd} - R_g i_{gd} + \frac{L_g}{L}R_s i_{gd} + \frac{L+L_g}{L}(\omega L i_{gq} - K_{ip}(i_{d,\text{ref}} - i_{gd}) - K_{ii}x_2) \tag{5.17}$$

$$v_{kq} = v_{gq} - R_g i_{gq} + \frac{L_g}{L}R_s i_{gq} + \frac{L+L_g}{L}(-\omega L i_{gd} - K_{ip}(I_{q,\text{ref}} - i_{gq}) - K_{ii}x_3) \tag{5.18}$$

Since $v_{pccd,q}$ is the control output of the converter, the effects of L_g and R_g on $v_{pccd,q}$ will be reflected in the Jacobian and eigenvalues of the closed-loop system.

There are 6 independent state variables forming the state vector $x = [i_{gd}\ i_{gq}\ v_{\text{dc}}\ x_1\ x_2\ x_3]^T$. The control output variables are represented by $y = [v_{kd}\ v_{kq}]^T$. In addition, the input variables are $u = [v_{gd}\ v_{gq}\ V_{\text{dc,ref}}\ I_{q,\text{ref}}\ R_L]^T$. Therefore, the complete state equations can be represented as

$$\dot{x} = f(x, y, u), \tag{5.19}$$

where

$$y = g(x, u). \tag{5.20}$$

The function f in the state equation can be derived from (5.4), (5.5), (5.6), (5.11), (5.13) and (5.15), and can be arranged as follows.

$$f_1(i_{gd}) = \frac{di_{gd}}{dt} = (K_{ip}(i_{d,\text{ref}} - i_{gd}) + K_{ii}x_2) - R_s i_{gd})/L \tag{5.21}$$

$$f_2(i_{gq}) = \frac{di_{gq}}{dt} = (K_{ip}(I_{q,\text{ref}} - i_{gq}) + K_{ii}x_3) - R_s i_{gq})/L \tag{5.22}$$

$$f_3(v_{\text{dc}}) = \frac{dv_{\text{dc}}}{dt} = \frac{3}{2Cv_{\text{dc}}}(v_{kd}i_{gd} + v_{kq}i_{gq}) - i_{\text{dc}} \tag{5.23}$$

$$f_4(x_1) = \frac{dx_1}{dt} = V_{\text{dc,ref}} - v_{\text{dc}} \tag{5.24}$$

$$f_5(x_2) = \frac{dx_2}{dt} = i_{d,\text{ref}} - i_{gd} \tag{5.25}$$

$$f_6(x_3) = \frac{dx_3}{dt} = I_{q,\text{ref}} - i_{gq} \tag{5.26}$$

The control function g can be found from (5.17) and (5.18), and can be arranged as follows.

$$g_1(i_{gd}) = v_{kd} = v_{gd} - R_g i_{gd} + \frac{L_g}{L}R_s i_{gd} + \frac{L + L_g}{L}(\omega L i_{gq} - K_{ip}(i_{d,\text{ref}} - i_{gd}) - K_{ii}x_2) \tag{5.27}$$

$$g_2(i_{gq}) = v_{kq} = v_{gq} - R_g i_{gq} + \frac{L_g}{L}R_s i_{gq} + \frac{L + L_g}{L}(-\omega L i_{gd} - K_{ip}(I_{q,\text{ref}} - i_{gq}) - K_{ii}x_3) \tag{5.28}$$

5.2.1 Steady-State Point

The steady-state values of the state variables, X_Q, can be found by setting the time-derivatives to zero, giving

$$I_d = I_{d,\text{ref}} = \frac{V_{gd} - \sqrt{V_{gd}^2 - \frac{8(R_s+R_g)V_{\text{dc,ref}}^2}{3R_L}}}{2(R_s+R_g)} \tag{5.29}$$

$$I_q = I_{q,\text{ref}} = 0 \tag{5.30}$$

$$V_{\text{dc}} = V_{\text{dc,ref}} \tag{5.31}$$

$$X_1 = \frac{I_{d,\text{ref}}}{K_{vi}} \tag{5.32}$$

$$X_2 = \frac{R_s I_{d,\text{ref}}}{K_{ii}} \tag{5.33}$$

$$X_3 = 0 \tag{5.34}$$

5.2.2 The Jacobian

The Jacobian can be derived from the state equation (5.19) and (5.20) by perturbing around the steady-state point X_Q, and is given as

$$J(X_Q) = \frac{\partial f}{\partial x} + \frac{\partial f}{\partial g} \cdot \frac{\partial g}{\partial x}\bigg|_{x=X_Q} \tag{5.35}$$

where x and g are the state vector and control function, respectively.

The Jacobian shown in (5.35) is a 6-dim square matrix, whose elements are

$$J_{11} = -(K_{ip}+R_s)/L; J_{12} = 0; J_{13} = -K_{ip}K_{vp}/L;$$

$$J_{14} = K_{ip}K_{vi}/L; J_{15} = K_{ii}/L; J_{16} = 0; \tag{5.36}$$

$$J_{21} = 0; J_{22} = -(K_{ip}+R_s)/L; J_{23} = 0;$$

$$J_{24} = 0; J_{25} = 0; J_{26} = K_{ii}/L; \tag{5.37}$$

$$J_{31} = \frac{3}{2CV_{\mathrm{dc,ref}}}(V_{gd} - 2R_g I_{d,\mathrm{ref}} - \frac{L - L_g}{L} R_s I_{d,\mathrm{ref}} + \frac{L + L_g}{L} K_{ip} I_{d,\mathrm{ref}});$$

$$J_{32} = 0;$$

$$J_{33} = \frac{3I_{d,\mathrm{ref}}}{2CV^2_{\mathrm{dc,ref}}}(\frac{L + L_g}{L} K_{ip} K_{vp} V_{\mathrm{dc,ref}} - V_{gd} + R_g I_{d,\mathrm{ref}} + R_s I_{d,\mathrm{ref}});$$

$$J_{34} = -\frac{3}{2CV_{\mathrm{dc,ref}}}(\frac{L + L_g}{L} K_{ip} K_{vp} I_{d,\mathrm{ref}});$$

$$J_{35} = -\frac{3}{2CV_{\mathrm{dc,ref}}}(\frac{L + L_g}{L} K_{ii} I_{d,\mathrm{ref}});$$

$$J_{36} = 0; \tag{5.38}$$

$$J_{41} = J_{42} = 0; J_{43} = -1; J_{44} = J_{45} = J_{46} = 0; \tag{5.39}$$

$$J_{51} = -1; J_{52} = 0; J_{53} = -K_{vp};$$

$$J_{54} = K_{vi}; J_{55} = J_{56} = 0; \tag{5.40}$$

$$J_{61} = 0; J_{62} = -1; J_{63} = J_{64} = J_{65} = J_{66} = 0. \tag{5.41}$$

Finally, the characteristic equation of the system can be written as

$$\det|\lambda I - A| = 0, \tag{5.42}$$

where $A = J(X_Q)$. The eigenvalues, which are the roots of the characteristic equation (5.42), can be calculated numerically.

Then, the stability of the system can be studied by calculating the eigenvalues. We mainly focus on the grid inductance which is varying according to the location where VSC is connected to the power grid. It can be found that as the grid impedance increases, the system becomes unstable with the pair of eigenvalues crossing to the right half complex plane. The eigenvalues around the critical point are listed in Table 5.3.

Furthermore, the stability of the system in the parameter space can be studied by inspecting the root locus. We take an analytical approach by examining the sign of the real part of the pair of eigenvalues. If it goes from negative to

Table 5.3: Eigenvalues of the system with varying L_g.

L_g	Eigenvalues	Stability
11.86 mH	$-0.155 \pm j1459.0$, -3.122, -3.997, -1729.4, -3.854	Stable
11.87 mH	$0.4286 \pm j1459.0$, -3.122, -3.997, -1729.4, -3.854	Unstable

positive, the system would exhibit a Hopf bifurcation and become oscillatory. We summarize the root loci in Fig. 5.4 under variations of selected parameters, including grid impedance, load resistance, outer voltage loop gain and link capacitor. The initial values of these parameters are $L_g = 6$ mH, $R_L = 75\ \Omega$, $K_{vp} = 2$, and $C = 1.5$ mF. The root locus locates the critical point of instability which is also the bifurcation point in the parameter space. The simulations reported in Section 5.4 verify the critical points found from the above analysis, and provide design-oriented boundaries of operation.

5.3 Simulation of the Low-Frequency Instability Using an Averaged Model

The phenomenon can be reexamined by simulation using an averaged model, as shown in Fig. 5.5. The transient waveform is shown in Fig. 5.6 (a), where low-frequency instability is observed. Also, in Fig. 5.6 (b), the steady-state low-frequency oscillation (before the bifurcation point) is shown as a red dot in the phase plane, and as the low-frequency instability develops beyond the bifurcation point, the phase portrait expands to a limit cycle.

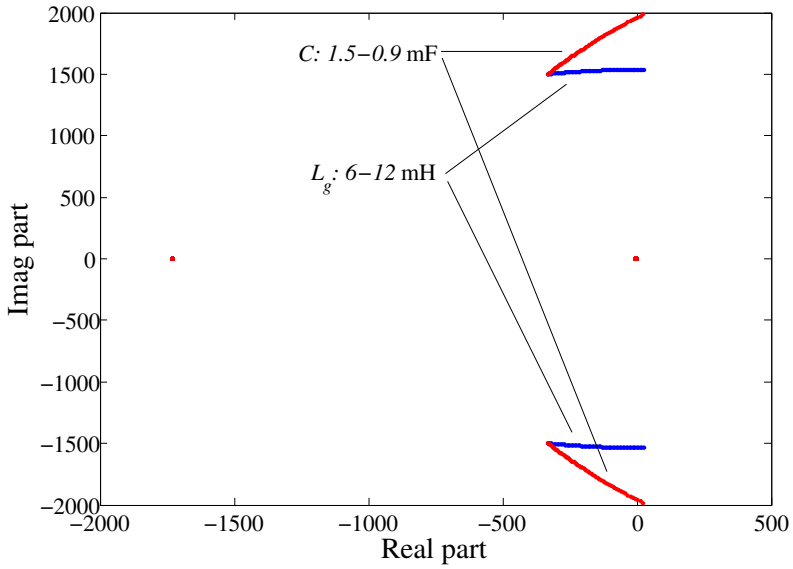

(a)

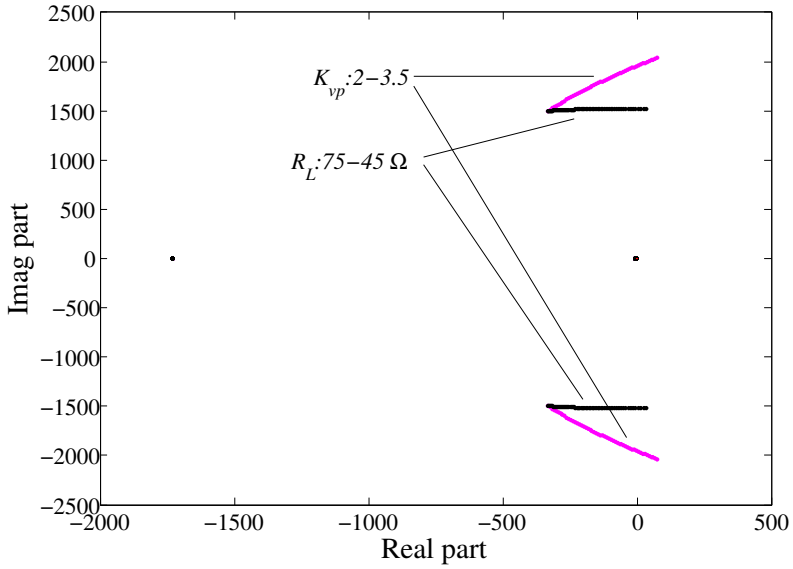

(b)

Figure 5.4: Root loci with parameters varying, (a) blue: grid impedance, red: link capacitor; (b) magenta: outer voltage loop gain, black: load resistance.

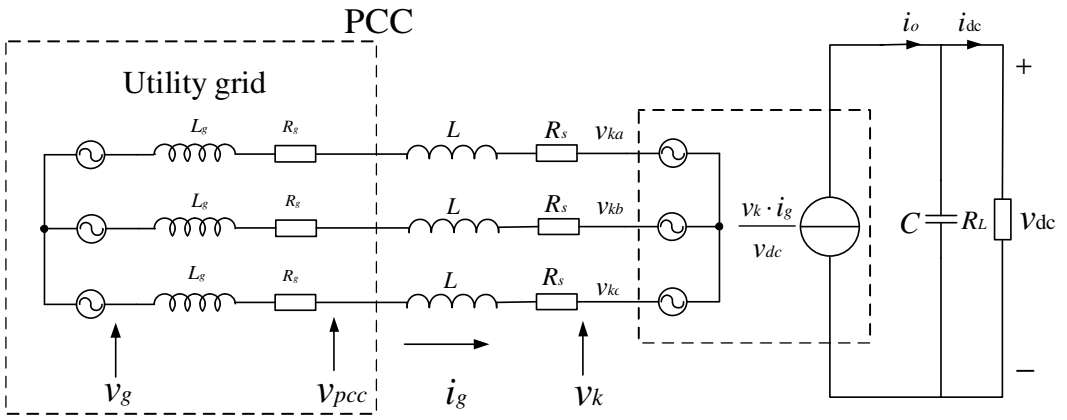

Figure 5.5: The average model of a three-phase voltage source converter connecting to non-ideal power grid.

5.4 Design-Oriented Analysis of Low-Frequency Instability

The precise operation of the three-phase VSC can be analyzed cycle by cycle with a detailed switch model. However, it is complicated and not readily applied in engineering design of the whole system. So, a design-oriented analysis is adopted here to examine the effects of system parameters on the location of Hopf bifurcation boundaries [117, 118]. In this section, the grid impedance L_g, DC gain of voltage loop K_{vp}, DC link capacitor C and load resistance R_L, which are most relevant to the instability, will be examined.

5.4.1 Grid Impedance

The grid impedance is a key parameter which affects the Hopf bifurcation boundary. The load resistance R_L and DC output voltage K_{vp} are chosen as the parameters to be varied, forming a R_L–K_{vp} parameter plane. The stability boundaries on this parameter plane at different values of grid impedance L_g are studied. For a specific value of L_g, a relatively larger load resistance and lower DC voltage loop gain would keep the system stable. The boundaries for different values of

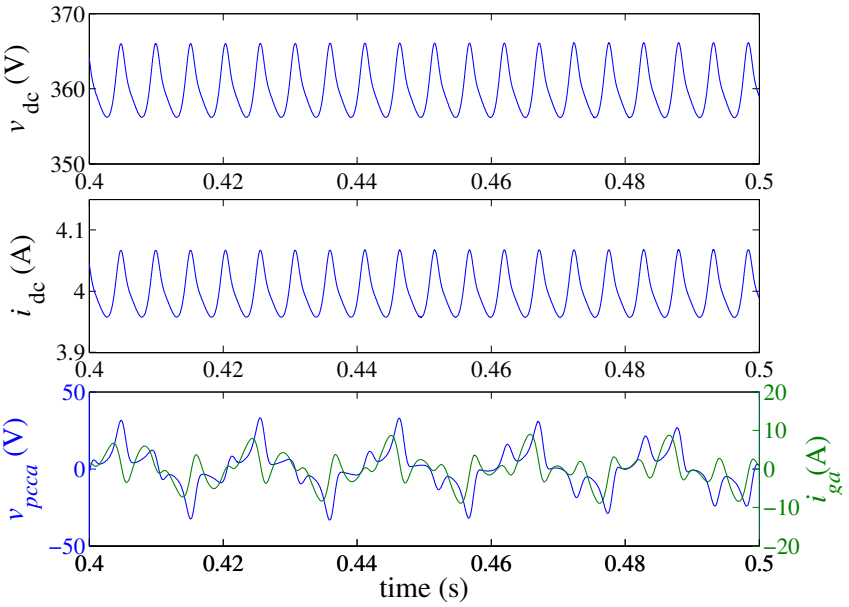

(a)

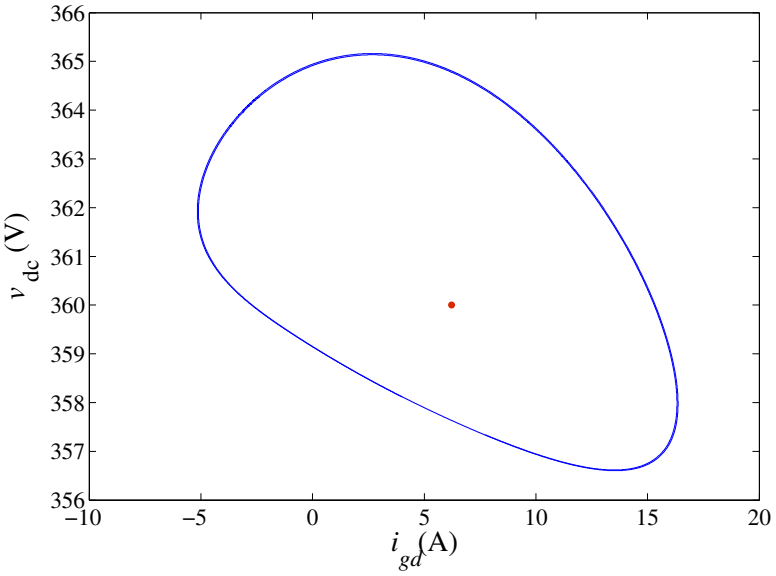

(b)

Figure 5.6: Simulations based on averaged model. The results are consistent with the cycle-by-cycle simulations. (a) The DC output oscillates at 150 Hz, and a large amount of harmonics emerges on line current; (b) when Hopf bifurcation occurs, the stable operation point (red dot) expands to a limit cycle (blue cycle).

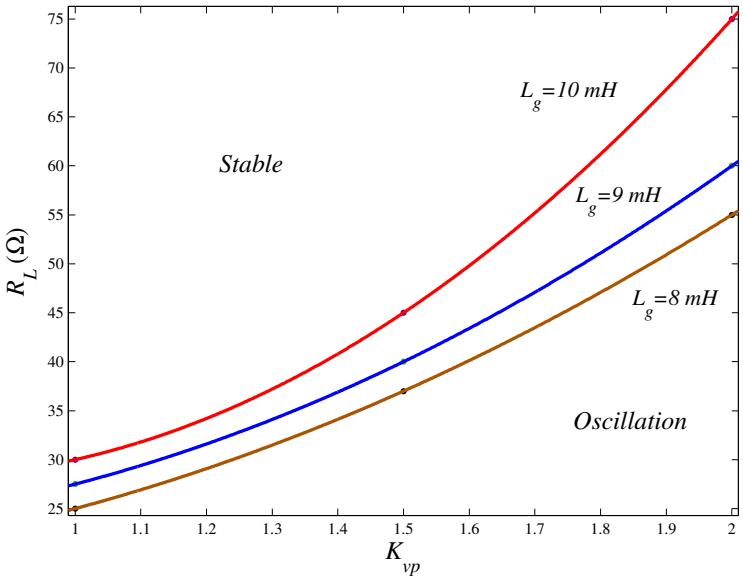

Figure 5.7: Stability boundaries on R_L–K_{vp} plane for different values of grid impedance L_g when $C = 1.5$ mF.

L_g are shown in Fig. 5.7.

5.4.2 DC Gain of Voltage Loop

The DC gain of the outer voltage loop K_{vp} is another key parameter which determines the Hopf bifurcation. Here, R_L and C are selected as two axis of the parameter plane. The stability boundaries on the R_L–C plane for different values of K_{vp} are shown in Fig. 5.8.

5.4.3 DC Link Capacitor

With a smaller DC link capacitor, the converter will more easily cross the Hopf bifurcation boundary. The DC link capacitor C also affects the locations of the stability boundaries, as shown in Fig. 5.9.

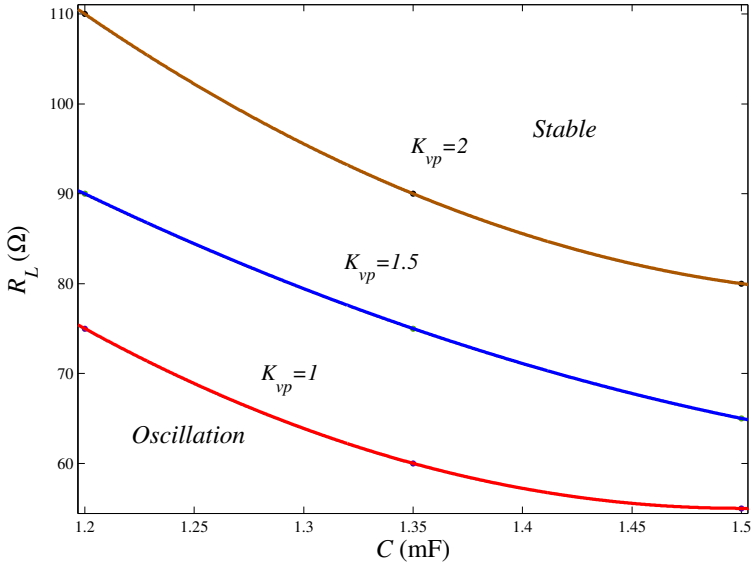

Figure 5.8: Stability boundaries on the R_L–C plane for different values of outer voltage loop gain K_{vp} when $L_g = 9$ mH.

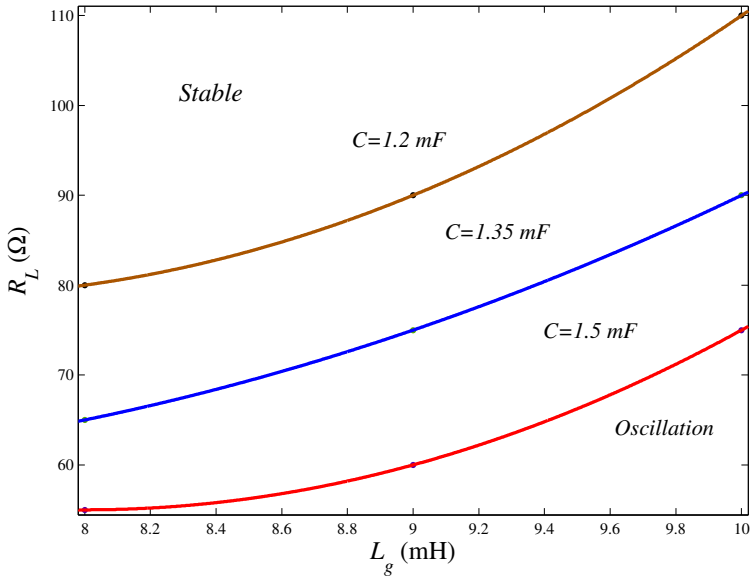

Figure 5.9: Stability boundaries on the R_L–L_g plane for different values of DC link capacitor C when $K_{vp} = 2$.

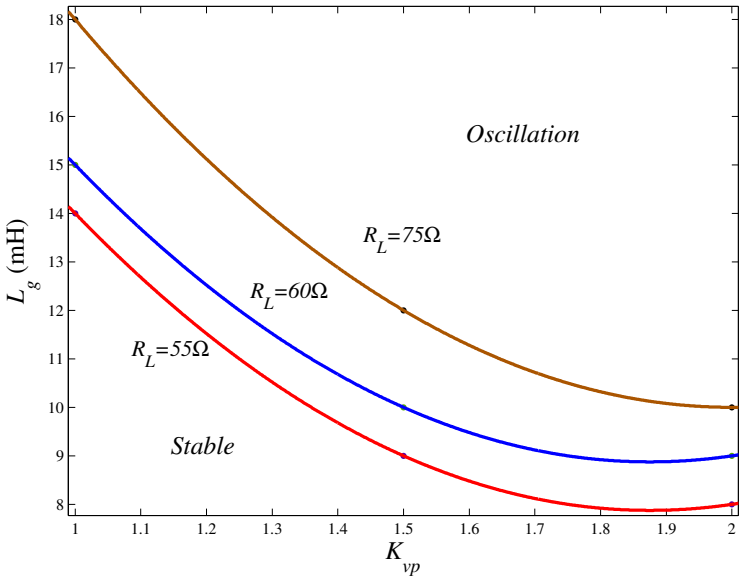

Figure 5.10: Stability boundaries on the L_g–K_{vp} plane for different values of load resistance R_L when $C = 1.5$ mF.

Table 5.4: Effects of increase of parameters on low-frequency oscillation. "+" means increased stability margin and "−" means reduced stability margin. The results are found to be robust in a wide range of operating points

Parameters (increase)	Stability
Grid impedance	−
DC gain of voltage loop	−
DC link capacitor	+
Load resistance	+

5.4.4 Load Resistance

With a heavier load, the system will more likely become unstable. As shown in Fig. 5.10, with a larger resistance R_L, the system may have a bigger stable region, i.e., more margin for system stability.

From the analysis above, a qualitative analysis of the effects of different system parameters is summarized in Table 5.4. This table indicates how the stability of the system is affected when parameters increase, with the "+" sign and "−" sign indicating a larger and small stability margin, respectively. For instance, when the VSC is connected to a weak grid with higher impedance, the stability margin

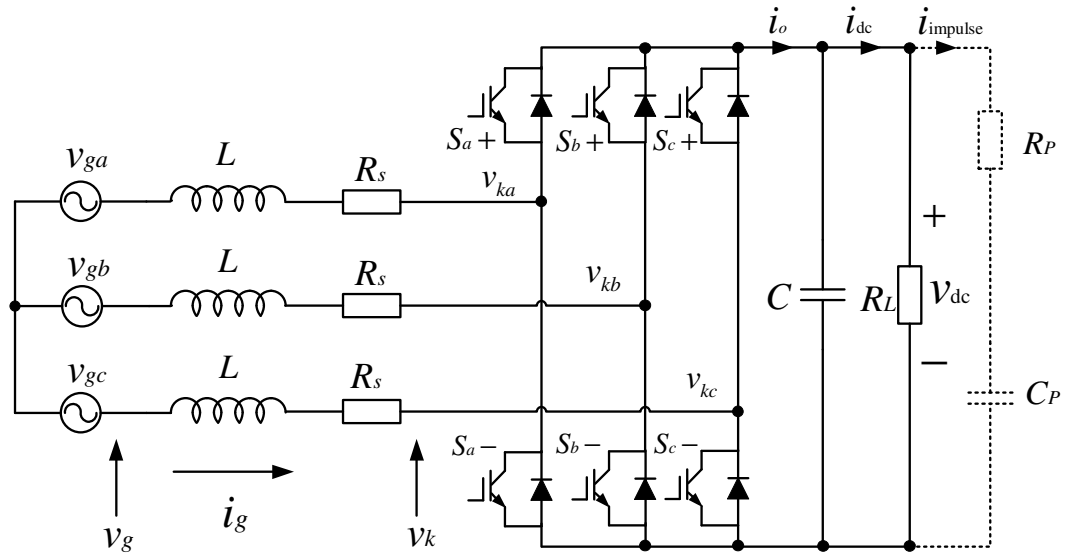

Figure 5.11: A series capacitive load consisting R_P and C_P is added to the DC load of the converter.

will be reduced. In this case, the designer can use a larger DC link capacitor to improve stability and acquire enough margin.

5.5 Interacting with Catastrophic Bifurcation

As pointed out in Chapter 3, the three-phase voltage source converter will exhibit catastrophic bifurcation when an external disturbance is applied to the DC load, as shown in Fig. 5.11. With the initial voltage of C_P set at 0 V, the additional load R_P and C_P as drawn in dotted lines will draw an impulse current from the original converter system. The system responds to the perturbation, and will get into catastrophic bifurcation. However, when the low-frequency instability occurs, the value of i_{gd} is varying around the operation point. Therefore, the system will be more prone to this catastrophic bifurcation. In other words, the occurrence of Hopf bifurcation affects the location of the catastrophic bifurcation boundary, representing another form of interacting bifurcation [99].

5.5.1 Limit Cycles

The magnitude of the triggering current has been shown to affect the stability of the system. As shown in Chapter 3, the system will be stable with small impulse perturbation, and may enter unstable operation when the perturbation is large enough. In order to study the limit cycle behavior, the system is set to work with low-frequency instability initially, and disturbed by an impulse current of various magnitudes.

A series of simulations are shown in Fig. 5.12. The system is configured with the same parameters as in Tables 5.1 and 5.2. With different choices of the grid impedance, the system exhibits a low-frequency limit cycle, whose magnitude varies for each choice of the grid impedance, as shown in Figs. 5.12 (a), (c) and (e). The critical impulse current magnitude that can drive the system into catastrophic bifurcation is shown in Figs. 5.12 (b), (d) and (f). For instance, the system may work with the red limit cycle A_1 of Fig. 5.12 (a). Then, a relatively larger impulse current, which is about 2.4 A and shown as point A_1 in Fig. 5.12 (b), is needed to drive the system into catastrophic bifurcation.

The simulation results show that the stability region is getting smaller with a higher grid impedance. However, with a particular grid impedance, heavier DC loading will drive the system closer to the boundary of catastrophic bifurcation.

5.5.2 Triggering Points

We define the triggering point as the time when the additional load is connected to the system. Since i_{gd} is oscillating when low-frequency instability occurs, the triggering point determines the response of the system. Two simulations are compared in Fig. 5.13 (a). When an additional load is connected to the system at different time points, the system behaves differently. The system behavior shown in Figs. 5.12 (e) and (f) is used here as an example. When the system is

triggered at 0.5 s by a series resister (280 Ω) and capacitor (2.35 mF), it damps for several cycles and converges to the original limit cycle. However, when the system is triggered at 0.504 s with the same components, it loses stability via catastrophic bifurcation.

When the external perturbation is connected to the system, the outer voltage loop will respond after a short delay. The transient dynamics of the system determines the trajectory of the system after the triggering point. If the system starts at a triggering point which leads to a trajectory that goes beyond the threshold value of i_{gd}, the system will exhibit catastrophic bifurcation (like the one shown in Fig. 5.13 (a) triggered at 0.504 s). However, the system is kept within the low-frequency oscillation if it is triggered at a point which leads to a trajectory that traverses within the threshold of i_{gd} and converges to low-frequency limit cycle (like the one shown in Fig. 5.13 (a) triggered at 0.5 s).

Therefore, for the same set of system parameters and perturbation, there is a conservative boundary within which the triggering signal will not push the i_{gd} to reach the critical value that leads to catastrophic bifurcation. The system will keep operating with a low-frequency limit cycle after being triggered. Meanwhile, there is an optimistic boundary within which the system can keep operating with low-frequency limit cycle after being triggered by a relative high impulse current. The two boundaries are both shown in Fig. 5.13 (b), where the conservative boundary (red) shows a small stable region and the optimistic boundary (blue) shows a relative large stable region. The two boundaries are shown to illustrate the interaction of the two bifurcations, since the varying control signals due to the existence of limit cycle arising from the Hopf bifurcation may affect the final operation the system after perturbation.

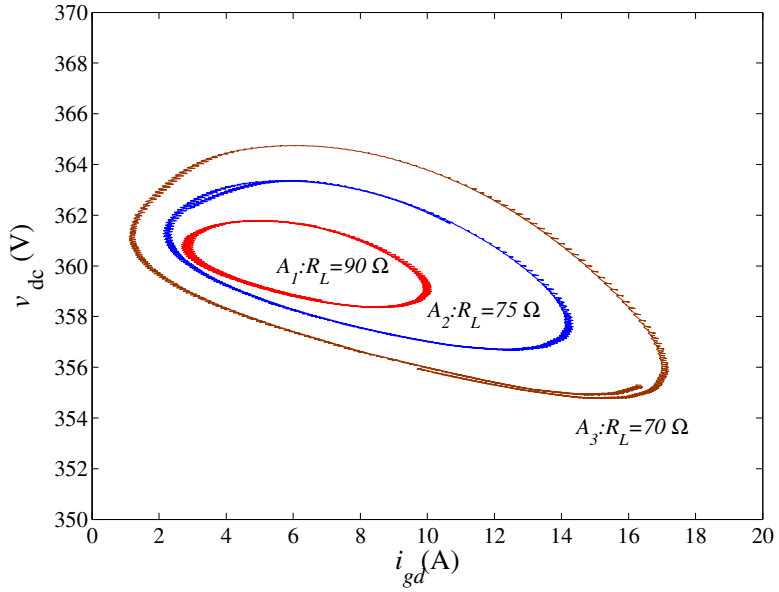
370
368
366
364
362
360
358
356
354
352
350
v_{dc} (V)
A_1:R_L=90 Ω
A_2:R_L=75 Ω
A_3:R_L=70 Ω
0
2
4
6
8
10
12
14
16
18
20
i_{gd}(A)

(a)

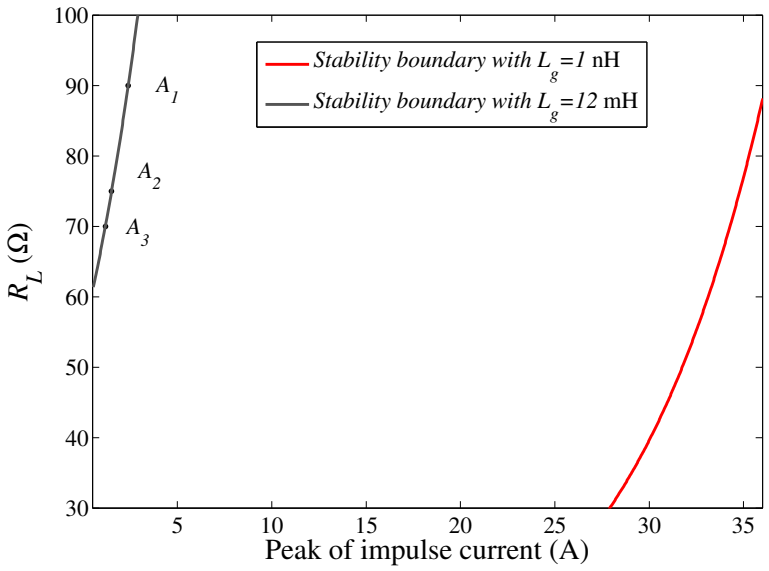
100
90
80
70
60
50
40
30
R_L (Ω)
Stability boundary with L_g=1 nH
Stability boundary with L_g=12 mH
A_1
A_2
A_3
5
10
15
20
25
30
35
Peak of impulse current (A)

(b)

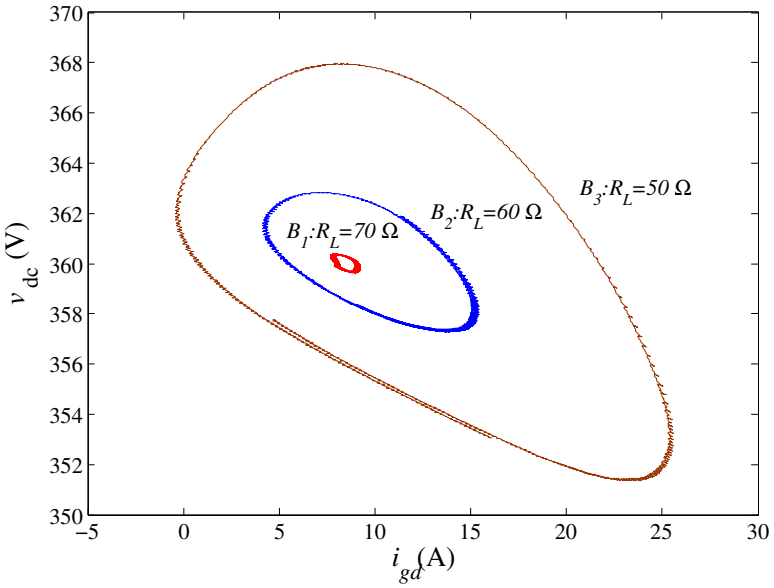
370
368
366
364
362
360
358
356
354
352
350
−5
0
5
10
15
20
25
30
v_{dc} (V)
i_{gd} (A)
B_3:R_L=50 Ω
B_2:R_L=60 Ω
B_1:R_L=70 Ω

(c)

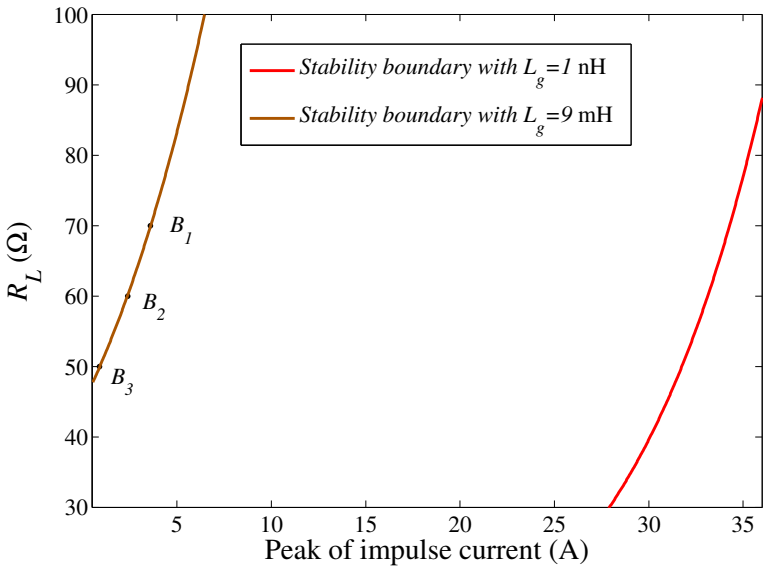
100
90
80
70
60
50
40
30
5
10
15
20
25
30
35
R_L (Ω)
Peak of impulse current (A)
Stability boundary with L_g=1 nH
Stability boundary with L_g=9 mH
B_1
B_2
B_3

(d)

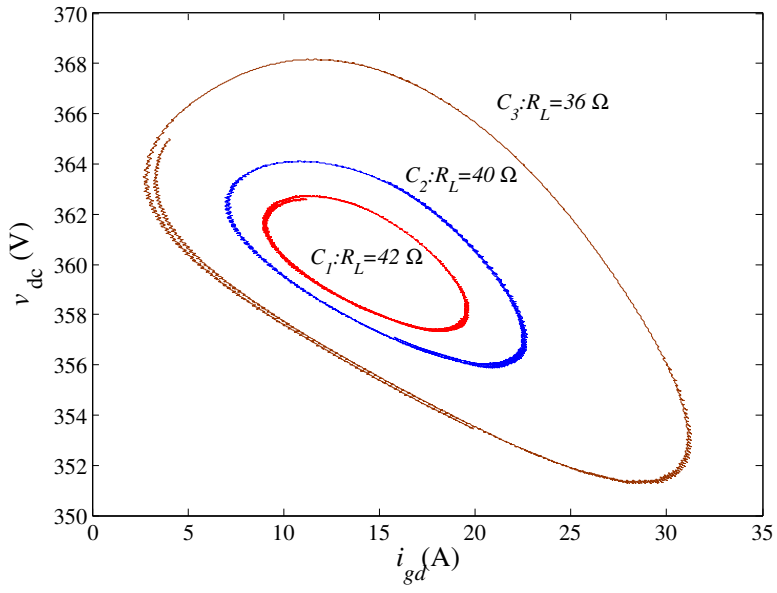

(e)

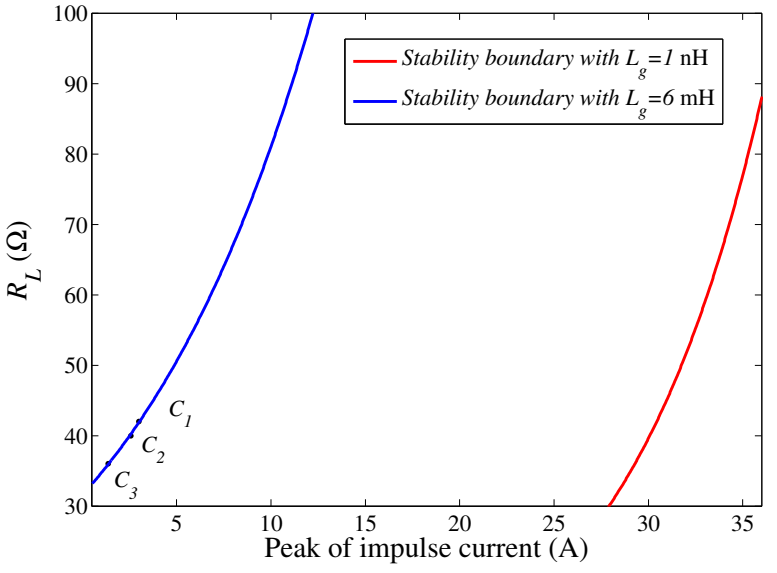

(f)

Figure 5.12: Variation of critical points of catastrophic bifurcation due to the emergence of low-frequency instability. (a), (c) and (e) show limit cycles. (b), (d) and (f) are critical impulse current.

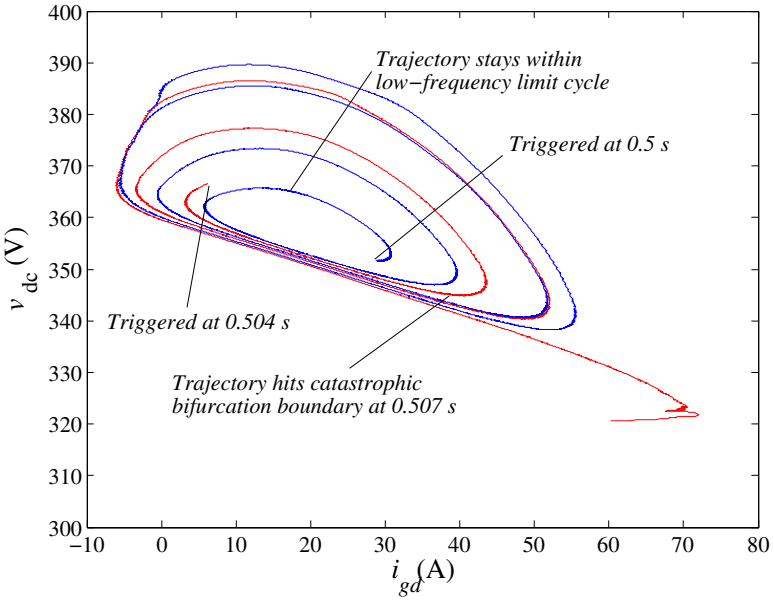

(a)

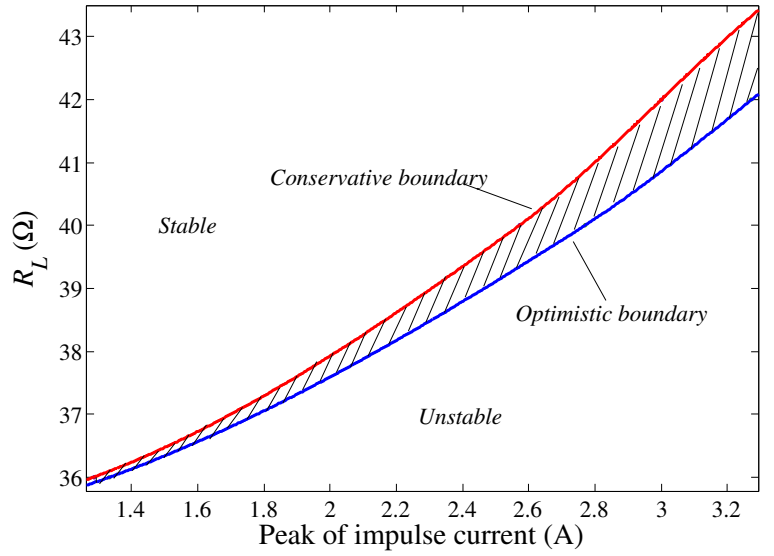

(b)

Figure 5.13: (a) The system is triggered at 0.5 s which leads to a trajectory (blue) that traverses within the threshold of i_{gd} and converges to low-frequency limit cycle. The system starts at a triggering point at 0.504 s which leads to a trajectory (red) that goes beyond the threshold value of i_{gd} at 0.507 s, and exhibits catastrophic bifurcation. (b) Conservative stability boundary (red) and optimistic stability boundary (blue) corresponding to different triggering times.

5.5.3 Analysis of Interaction

The presence of the grid impedance causes two separate mechanisms responsible for reducing the stability margin of the three-phase voltage source converter.

First, as shown in Chapter 3, there is a critical value $i_{gd}(i_{o,\max})$ of i_{gd} which is $\frac{v_{gd}}{2R_s}$, above which the system will exhibit catastrophic bifurcation. It is shown in the following that the value of $i_{gd}(i_{o,\max})$will decrease significantly due to the presence of the grid impedance.

From (5.9) and (5.17), v_{pccd} can be expressed as

$$v_{pccd} = v_{gd} - R_g i_{gd} - \frac{L_g}{L + L_g} R_s i_{gd}. \tag{5.43}$$

Since the output power of the PFC converter, which is $P_{out} = \frac{3}{2}(v_{pccd} i_{gd} - R_s i_{gd}^2)$, will saturate due to the increase of i_{gd}, the value of $i_{gd}(i_{o,\max})$ can be found by setting $\frac{dP_{out}}{di_{gd}} = 0$, i.e.,

$$i_{gd}(i_{o,\max}) = \frac{v_{gd}}{2(R_g + \frac{L_g}{L+L_g} R_s + R_s)}, \tag{5.44}$$

which explains the reduction of the stability region, as shown in Figs. 5.12 (b), (d) and (f), as the grid impedance increases.

Second, the emergence of the limit cycle will affect the transient process when the system loses stability, depending on the magnitude of the limit cycles and the triggering points. When low-frequency instability occurs, the outer voltage loop is oscillating. The voltage loop-gain state-space equations can be obtained

as follows.

$$e_v = V_{\text{dc,ref}} - v_{dc} \tag{5.45}$$

$$i_{gd} = K_{vp} e_v + K_{vi} \int e_v dt \tag{5.46}$$

$$C \frac{de_v}{dt} = \frac{v_{dc}}{R_L} - \frac{3}{2} \frac{v_{gd} i_{gd} - R_e i_{gd}^2}{v_{dc}}, \tag{5.47}$$

where

$$R_e = R_g + \frac{L_g}{L + L_g} R_s + R_s. \tag{5.48}$$

To find a periodic solution for equation (5.47), sinusoidal approximation of state variables of up to second order is used and written as

$$\begin{aligned} e_v &= a_0 + a_1 \cos(\omega t) + a_2 \sin(\omega t) \\ &\quad + a_3 \cos(2\omega t) + a_4 \sin(2\omega t) \end{aligned} \tag{5.49}$$

$$\begin{aligned} i_{gd} &= K_{vp} e_v + K_{vi} T e_v \\ &= K_{vp} a_0 + K_{vi} a_0 t \\ &\quad + (K_{vp} a_1 - \frac{K_{vi} a_2}{\omega}) \cos(\omega t) + (K_{vp} a_2 + \frac{K_{vi} a_1}{\omega}) \sin(\omega t) \\ &\quad + (K_{vp} a_3 - \frac{K_{vi} a_4}{2\omega}) \cos(2\omega t) + (K_{vp} a_4 + \frac{K_{vi} a_3}{2\omega}) \sin(2\omega t) \\ &\approx i_0 + \frac{K_{vi} a_0}{\omega} \sin(\omega t) \\ &\quad + (K_{vp} a_1 - \frac{K_{vi} a_2}{\omega}) \cos(\omega t) + (K_{vp} a_2 + \frac{K_{vi} a_1}{\omega}) \sin(\omega t) \\ &\quad + (K_{vp} a_3 - \frac{K_{vi} a_4}{2\omega}) \cos(2\omega t) + (K_{vp} a_4 + \frac{K_{vi} a_3}{2\omega}) \sin(2\omega t) \end{aligned} \tag{5.50}$$

where i_0 is fundamental component of i_{gd} in Fourier expansion, i.e.,

$$i_0 = K_{vp} a_0, \tag{5.51}$$

and ω is the oscillation frequency of the limit cycle beyond Hopf bifurcation. From (5.49), de_v/dt can be written as

$$\frac{de_v}{dt} = e_v' = -a_1\omega\sin(\omega t) + a_2\omega\cos(\omega t) - 2a_3\omega\sin(2\omega t) + 2a_4\omega\cos(2\omega t), \quad (5.52)$$

and e_v^2 can be approximated as

$$\begin{aligned} e_v^2 = {} & a_0^2 + 2a_0a_1\cos(\omega t) + 2a_0a_2\sin(\omega t) \\ & + (2a_0a_3 + \frac{a_1}{2} - \frac{a_2}{2})\cos(2\omega t) + (2a_0a_4 + a_1a_2)\sin(2\omega t). \end{aligned} \quad (5.53)$$

Using the above approximations, the state equation, i.e., (5.47), can be simplified as

$$C(V_{\mathrm{dc,ref}} - e_v)e_v' + \frac{3}{2}(v_{gd}i_{gd} - R_e i_{gd}^2) - \frac{(V_{\mathrm{dc,ref}} - e_v)^2}{R_L} = 0 \quad (5.54)$$

The coefficients $a_0, a_1, \cdots, a_4$ can be found by equating the coefficients of (5.54) for each of the harmonic bases, i.e., $1, \cos\omega t, \sin\omega t, \cdots, \sin 2\omega t$. The expressions for a_0, a_1 and a_2 are calculated as

$$a_0 = \frac{i_0}{K_{vp}} \quad (5.55)$$

$$\begin{aligned} a_1 = {} & -(9K_{vi}K_{vp}\omega R_L^2 a_0 v_{gd}^2 + 12K_{vi}\omega R_L a_0^2 v_{gd} \\ & - 12K_{vi}V_{\mathrm{dc,ref}}\omega R_L a_0 v_{gd})/(4C^2R_L^2a_0^2\omega^4 \\ & - 8C^2R_L^2a_0V_{\mathrm{dc,ref}}\omega^4 + 4C^2R_L^2V_{\mathrm{dc,ref}}^2\omega^4 \\ & + 12CR_L^2a_0K_{vi}v_{gd}\omega^2 - 12CR_L^2K_{vi}V_{\mathrm{dc,ref}}v_{gd}\omega^2 \\ & + 9R_L^2K_{vi}^2v_{gd}^2 + 9R_L^2K_{vp}^2v_{gd}^2\omega^2 + 24R_La_0K_{vp}v_{gd}\omega^2 \\ & - 24R_LK_{vp}V_{\mathrm{dc,ref}}v_{gd}\omega^2 + 16a_0^2\omega^2 \\ & - 32a_0V_{\mathrm{dc,ref}}\omega^2 + 16V_{\mathrm{dc,ref}}^2\omega^2) \end{aligned} \quad (5.56)$$

$$
\begin{aligned}
a_2 = (&6CR_L^2 a_0^2 K_{vi} v_{gd}\omega^2 + 9R_L^2 a_0 K_{vi}^2 v_{gd}^2 \\
&- 6CV_{\mathrm{dc,ref}} R_L^2 a_0 K_{vi} v_{gd}\omega^2)/(4C^2 R_L^2 a_0^2 \omega^4 \\
&- 8C^2 R_L^2 a_0 V_{\mathrm{dc,ref}}\omega^4 + 4C^2 R_L^2 V_{\mathrm{dc,ref}}^2 \omega^4 \\
&+ 12CR_L^2 a_0 K_{vi} v_{gd}\omega^2 - 12CR_L^2 K_{vi} V_{\mathrm{dc,ref}} v_{gd}\omega^2 \\
&+ 9R_L^2 K_{vi}^2 v_{gd}^2 + 9R_L^2 K_{vp}^2 v_{gd}^2\omega^2 + 24R_L a_0 K_{vp} v_{gd}\omega^2 \\
&- 24R_L K_{vp} V_{\mathrm{dc,ref}} v_{gd}\omega^2 + 16a_0^2\omega^2 \\
&- 32a_0 V_{\mathrm{dc,ref}}\omega^2 + 16V_{\mathrm{dc,ref}}^2\omega^2)
\end{aligned} \tag{5.57}
$$

The expressions for a_3 and a_4 are omitted here as they can be readily found in terms of a_1 and a_2.

The first-order approximation of the magnitude of the limit cycle is given as

$$|i_{gd,\mathrm{ripple}}| \approx \sqrt{a_1^2 + a_2^2}. \tag{5.58}$$

The magnitude calculated from equation (5.58) is shown in Fig. 5.14, which shows similar relationship to the value of load resister R_L as obtained from the simulation shown in Fig. 5.12 (a).

Thus, the stability margin can be re-defined as

$$i_{gd,\mathrm{margin}} = i_{gd}(i_{o,\max}) - i_{g0} - |i_{gd,\mathrm{ripple}}| \tag{5.59}$$

where i_0 is defined in (5.51).

For the system with parameters configured as in Table 5.5, the calculated

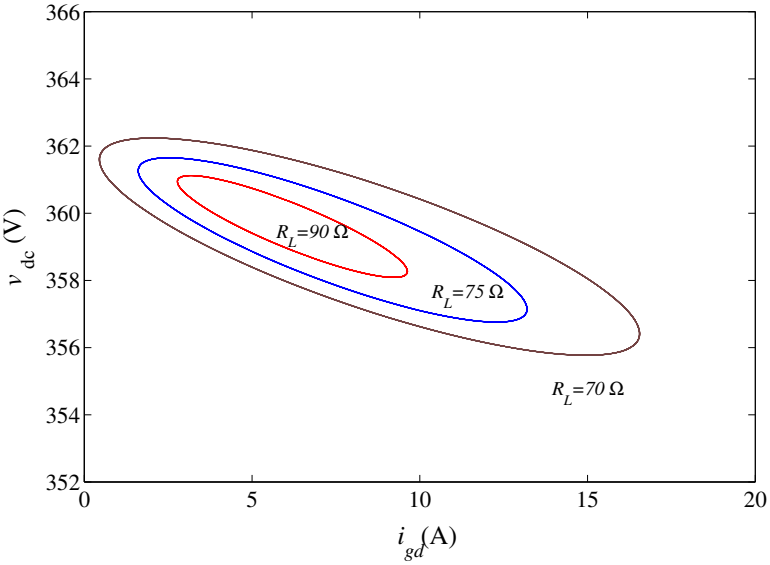

Figure 5.14: Calculated periodic solutions for the system using the parameters in Fig. 5.12 (a).

result is

$$e_v = 2.5756 + 0.7253\cos(\omega t) - 1.9629\sin(\omega t) + 0.004\cos(2\omega t) - 0.007\sin(2\omega t) \quad (5.60)$$

$$i_{gd} = 5.1513 + 4.5762\cos(\omega t) - 2.7653\sin(\omega t) + 0.014\cos(2\omega t) - 0.011\sin(2\omega t) \quad (5.61)$$

As before, we use a step change on the DC load to trigger the catastrophic bifurcation. As predicted above, the stability margin is reduced dramatically due to the presence of R_g, L_g and $i_{gd,\text{ripple}}$. For the system with parameters shown in Table 5.5, the stability margin is only 5 A. Hence, a small step change of 5 A is applied to the DC side of the system which causes low-frequency oscillation (Hopf) and drives the system into unstable region through catastrophic bifurcation, as shown in Fig. 5.15.

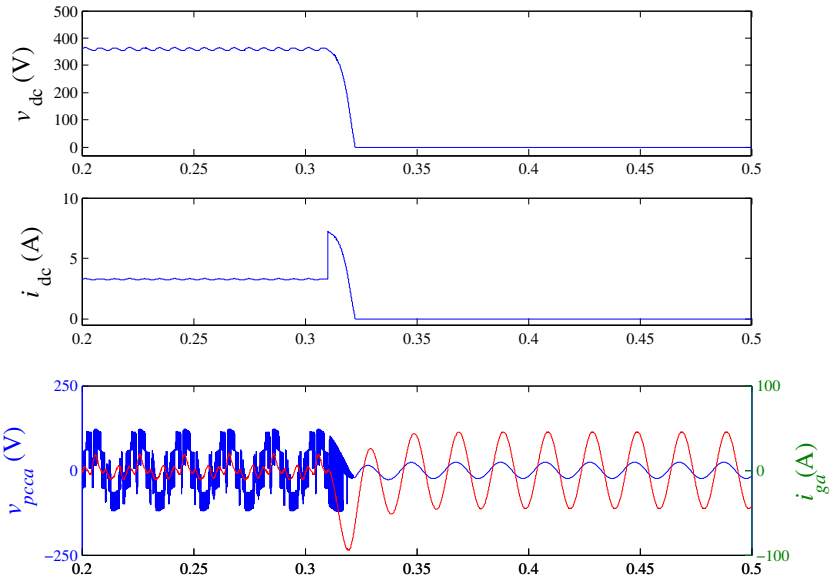

Figure 5.15: The system are easily enters an abnormal operation though catastrophic bifurcation due to the existence of Hopf-type low-frequency oscillation at the initial time of operation.

5.6 Experimental Observation

Our purpose here is to verify the low-frequency instability phenomenon identified and analyzed in the previous sections. A 1.2 kW three-phase PFC power supply has been used in the experiment. Table 5.5 gives the component values used. The set of inductors, $L_g = 3$ mH, are inserted here to represent the large set of grid impedance.

Figure 5.16 shows the experimentally observed low-frequency instability behavior, which is in perfect agreement with the simulated results given in Fig. 5.2 (a). The undesirable operation can be clearly identified in the waveform. The system achieves a low-frequency oscillation on the DC output voltage and has large amount of distortions on the line current. It can be found that the oscillation frequency on the DC output voltage is 150 Hz. The result verifies that the converter exhibits the Hopf bifurcation phenomenon mentioned in Section 5.1.

As analyzed in Section 5.5, due to the existence of Hopf bifurcation, the sta-

Table 5.5: Circuit components values of the experimental three-phase voltage source converter with an input protective transformer. The component values of L, L_g and C correspond to the transformer secondary.

Parameters/Components	Values
$v_{ga,gb,gc}$	110 Vrms
secondary v_{dc}	360 V
f	50 Hz
f_s	10 kHz
L	1.2 mH
L_g	3 mH
R_L	110 Ω
C	2.35 mF

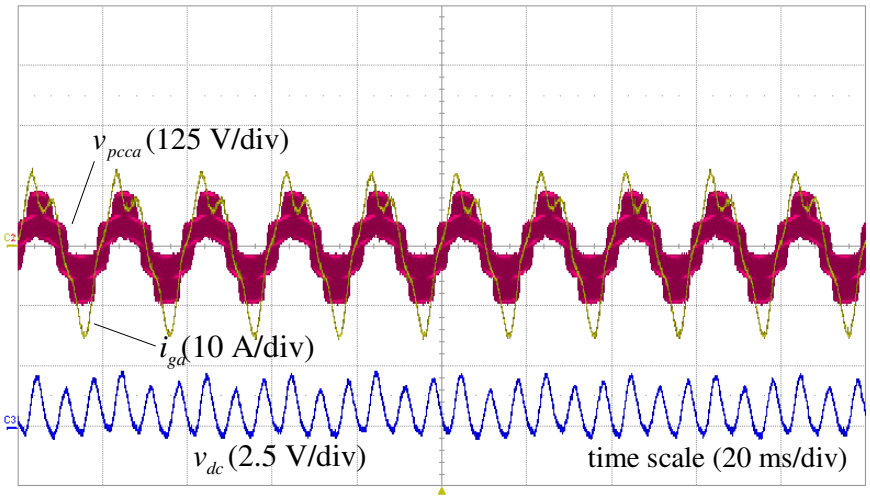

Figure 5.16: Experimental waveforms showing low-frequency instability of the rectifier. Channel 1 (red), channel 2 (yellow) and channel 3 (blue) are waveforms of phase "a" line voltage v_{pcca}, line current i_{ga}, and AC coupled output voltage v_{dc} respectively. The line current is highly distorted. A 150 Hz oscillation is observed at output voltage v_{dc}. As there is a slight unbalance of the three-phase practical power grid, the peak of the oscillation wave repeats itself at two peaks interval.

bility boundary of the catastrophic bifurcation changes dramatically. Specifically, the converter is much more prone to catastrophic bifurcation, and gets into the unstable region more readily.

Here, a step change of about 5 A is applied at the DC side of the converter mentioned above. For experimental feasibility, a non-optimized equivalent value of $R_s = 1\ \Omega$ is used to illustrate the existence of the catastrophic bifurcation. Without the appearance of low-frequency oscillation, the system can respond correctly to the step change, and will recover to its normal operation after the transient, as shown in Fig. 5.17 (a). However, when the low-frequency oscillation occurs, as shown in the initial time portion of Fig. 5.17 (b), the system will quickly move to an abnormal operation through catastrophic bifurcation. Note that the DC output of converter collapses, and the line current expands to very high value which clips the bottom portion of the initial current transient of the output of the current probe.

5.7 Summary

Three-phase voltage source converters connected to a non-ideal power grid are a practical form of system configuration. In this chapter, we study the stability of such grid-connected systems, and observe the Hopf bifurcation phenomenon, which appears as low-frequency instability in the grid-connected three-phase voltage source converters. An averaged model of the VSC and non-ideal power grid is appropriately adopted in this study. The system characteristic equations, calculated eigenvalues and root loci are presented. The stability boundaries indicated by numerical study have been verified using cycle-by-cycle simulations. Due to the complex operation of the converter, a design-oriented analysis is adopted in to obtain a direct design guidance of the VSC [123, 124]. Furthermore, the expanded limit cycle pushes the VSC closer to its stability boundary of catastrophic

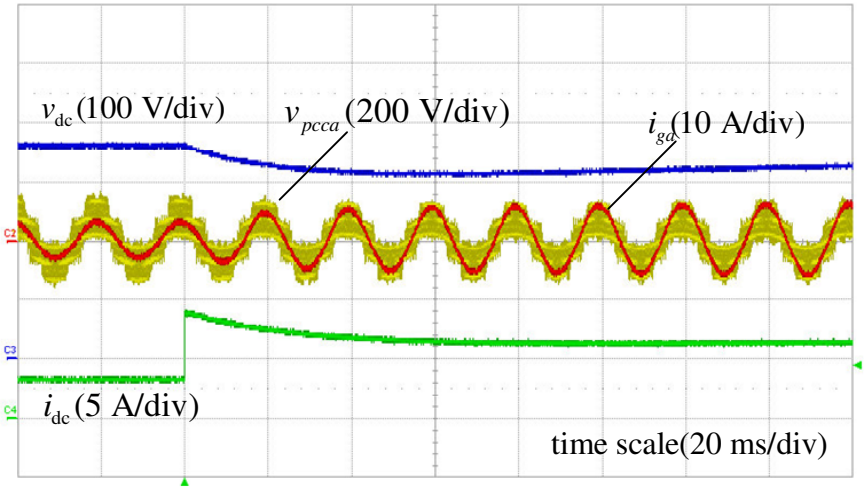

(a)

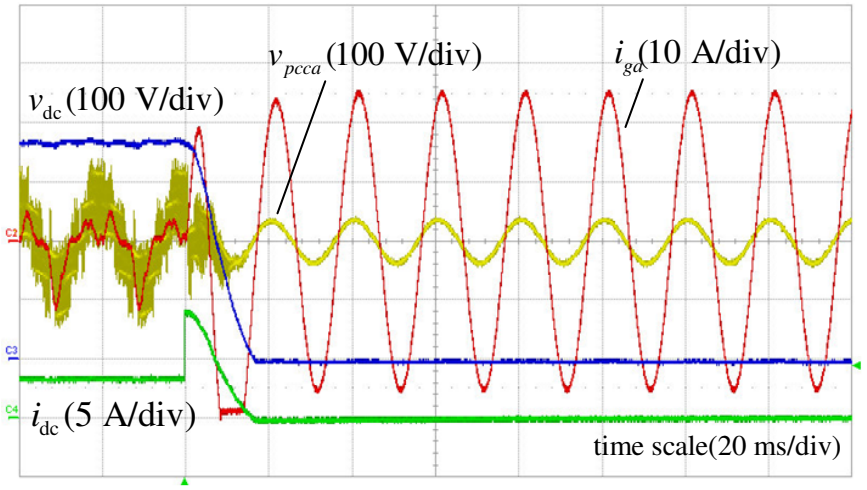

(b)

Figure 5.17: Experimental waveforms showing the interaction of Hopf-type low-frequency instability and catastrophic bifurcation of the rectifier. Channel 1 (yellow), channel 2 (red), channel 3 (blue), and channel 4 (green) are waveforms of phase a line voltage v_{pcca}, line current i_{ga}, DC output voltage $v_{\rm dc}$ and DC output current $i_{\rm dc}$ respectively. (a) The system achieves normal operation after a step change of about 5 A at the DC output. (b) The system exhibits a catastrophic bifurcation and moves to abnormal operation due to the existence of Hopf bifurcation with a same step change at the DC output.

bifurcation, which is highly undesirable for practical purposes. To prevent the catastrophic bifurcation, a common practical method is to clamp the control reference current below the maximum point, even when it is pushed to increase by the limit cycle or the external perturbation. Our study has illustrated how stability could be affected by variation of grid and converter parameters. The result provides useful design information regarding the choice of operating parameters that would ensure proper stable operation.

Chapter 6

Conclusions and Suggestions for Future Research

This chapter summarizes the contributions that have been achieved in this project. Also, some suggestions and potential areas of investigation will be given for future research extension.

6.1 Contributions of the Thesis

The three-phase voltage source converter (VSC) is a widely used bidirectional AC-DC interface converter in three-phase power systems. Recently, instead of using traditional centralized power generation, there is a trend that an increasing number of renewable energy sources are connected to the power grid in an attempt to alleviate the "energy crisis". These renewable energy sources can provide clean energy to replace the fossil fuels. The three-phase VSC plays an important role in connecting the DC devices and the AC grid. Although application-oriented research has emerged from the late 1980s, the three-phase VSC has attracted much attention recently due to its application in distributed hybrid power systems (DHPS), where some stability problems may occur. The previous research mainly

focuses on the three-phase VSC connected to an ideal grid and deals with the stability problem within a relatively small range of operating conditions. In this thesis, we re-examined the stability problem from the bifurcation analysis' point of view. The specific contributions are re-iterated here under the following four main areas:

1. The catastrophic bifurcation in the three-phase voltage source converter has been identified, and the nonlinearity characteristic in the converter has been described in detail.

This phenomenon may occur when a sufficiently large step load is connected, or under variation of other parameters. When catastrophic bifurcation occurs, the output DC voltage will collapse, and the input line current will expand to a very high value, which is dangerous for the VSC and grid. The nonlinearity lies in the current transfer function of the VSC because of the presence of the series resistance of the line reactor or the saturation in the over-modulation region of the PWM. When triggered by an impulsive load current or the application of a large step load, the output current will reach a maximum as the control reference current increases, altering the system's loop-gain, thereby destabilizing the system. The system loses stability in a catastrophic bifurcation which is accompanied by an expansion of reactive power or equivalently an expanded excursion in the state space. Our results provide design information regarding the choice of operating parameters that would ensure proper stable operation.

2. An irreversible bifurcation phenomenon has been identified under the variation of the grid impedance and an interacting load in the system of a three-phase voltage source converter connected to a non-ideal power grid with interacting load.

The system under study here represents a practical form of system configuration. The three-phase VSC is connected to the power grid which is non-ideal while some other interacting loads may be connected to the same point of com-

mon coupling (PCC). The root cause of this irreversible bifurcation phenomenon is also the nonlinearity in the current transfer function, which is caused by the limited input active power provided by the power grid. After the bifurcation occurs, the drop of the DC output voltage and expansion of the AC input current reveal that only reactive power is sunk by the converter, which is undesirable for the application. A detailed analysis of the control system failure and the cause of instability are given. The study clearly illustrates how stability could be affected by variation of power grid and interacting load parameters. The result provides useful design information regarding the choice of operating parameters that would ensure proper stable operation.

3. The low-frequency Hopf-type bifurcation in the three-phase voltage source converter has been identified due to the existence of a set of grid impedance.

A simple system configuration has been proposed, which consists of a three-phase VSC connected to a non-ideal power grid with inductive grid impedance. This system is a common configuration in DHPS. The stability of such a grid-connected converter systems has been studied, and a Hopf-type bifurcation phenomenon has been identified. An averaged model of the VSC and non-ideal power grid is adopted in this study. The system characteristic equations are presented with calculated eigenvalues and root loci. The analysis clearly shows the emergence of Hopf bifurcation when the root loci move to the right half plane (RHP). The design-oriented stability boundaries indicated by numerical study have been verified using simulations and experiments. The study clearly illustrates how stability could be affected by variation of grid and converter parameters.

4. The interaction between the low-frequency Hopf-type bifurcation and catastrophic bifurcation has been analyzed in the three-phase voltage source converter. It is found that the limit cycle of Hopf-type bifurcation will affect the stability margin for the catastrophic bifurcation dramatically.

Due to the occurrence of Hopf bifurcation, the three-phase VSC operating

point expands to a limit cycle which will push the converter closer to its stability boundary of catastrophic bifurcation. Adopting a harmonic balance method, the periodic solution has been found for the system and the magnitude of the limit cycles can be calculated from the solution. The result illustrates that the limit cycle affects the stability margin of the catastrophic bifurcation. A series of simulations shows how stability could be affected by variation of grid and converter parameters. The result provides useful design information regarding the choice of operating parameters that would ensure proper stable operation.

6.2 Suggestions for Future Research

Based on the theoretical study conducted in this project, some feasible suggestions and potential areas of investigation are given for future research extension.

6.2.1 Parallel-Connected Converters

In practice, there can be a large number of converters connected to the power grid. These converters can fetch or inject power at the same time. The topology of the whole system can be abstracted as a parallel system of converters. The working principle might be complex because the operating states will be determined by a number of factors related to the renewable energy sources and the final users.

6.2.2 Effects of Grid Impedance

Traditionally, the power grid can be simply modeled as an ideal voltage source. However, the practical power grid is not an ideal one, especially under weak grid conditions. The grid impedance has been shown to result in harmonic distortion problems [60, 119] for power converters, and some serious stability problems as identified in Chapters 4 and 5. Despite the rich possibility of dynamical behav-

ior of switching converters, the effects of the grid impedance have rarely been discussed. Further study in this direction should be encouraged.

6.2.3 Unbalanced Grid or Loads

For a balanced three-phase system, the Park and Clarke transformation provides an easy way to model and analyze the system. However, the real situation will be an unbalanced three-phase system because some single-phase devices may connect to the system or there are mismatches of the three-phase devices. The former Park and Clarke transformation cannot deal with the unbalanced components. Effective representation of the unbalanced three-phase systems would be highly desirable and further work would be needed to facilitate nonlinear analysis of the unbalanced systems.

Bibliography

[1] B. Bose, "Global warming: Energy, environmental pollution, and the impact of power electronics," *IEEE Industrial Electronics Magazine*, vol. 4, no. 1, pp. 6–17, 2010.

[2] "Global status report: 2005-2012," http://www.ren21.net/gsr.

[3] "Northeast blackout," http://en.wikipedia.org/wiki/Northeast_Blackout_of_2003.

[4] J. Romero, "Blackouts illuminate india's power problems," *IEEE Spectrum*, vol. 49, no. 10, pp. 11–12, 2012.

[5] J. Svensson, "Active distributed power systems functional structures for real-time operation of sustainable energy systems," Ph.D. dissertation, Lund University, 2006.

[6] N. Prabhu and K. Padiyar, "Investigation of subsynchronous resonance with VSC-based HVDC transmission systems," *IEEE Transactions on Power Delivery*, vol. 24, no. 1, pp. 433–440, 2009.

[7] L. Maharjan, T. Yamagishi, and H. Akagi, "Active-power control of individual converter cells for a battery energy storage system based on a multilevel cascade PWM converter," *IEEE Transactions on Power Electronics*, vol. 27, no. 3, pp. 1099–1107, 2012.

[8] A. K. Verma, B. Singh, and D. Shahani, "Grid interfaced solar photovoltaic power generating system with power quality improvement at AC mains," in *Proceedings, IEEE Third International Conference on Sustainable Energy Technologies (ICSET)*, 2012, pp. 177–182.

[9] Z. Chen, J. Guerrero, and F. Blaabjerg, "A review of the state of the art of power electronics for wind turbines," *IEEE Transactions on Power Electronics*, vol. 24, no. 8, pp. 1859–1875, 2009.

[10] A. Trzynadlowski, *Introduction to Modern Power Electronics*, 2nd ed. New York: John Wiley & Sons, 2010.

[11] T. Lipo, "Analog computer simulation of a three-phase full-wave controlled rectifier bridge," *Proceedings of the IEEE*, vol. 57, no. 12, pp. 2137–2146, 1969.

[12] N. Mohan, T. Udeland, and W. Robbins, *Power Electronics: Converters, Applications and Design*, 2nd ed. New York: Wiley, 1995.

[13] R. Ridley, S. Kern, and B. Fuld, "Analysis and design of a wide input range power factor correction circuit for three-phase applications," in *Proceedings, Eighth Annual Applied Power Electronics Conference and Exposition (APEC)*, 1993, pp. 299–305.

[14] M. Rastogi, R. Naik, and N. Mohan, "A comparative evaluation of harmonic reduction techniques in three-phase utility interface of power electronic loads," *IEEE Transactions on Industry Applications*, vol. 30, no. 5, pp. 1149–1155, 1994.

[15] H. Mao, C. Lee, D. Boroyevich, and S. Hiti, "Review of high-performance three-phase power-factor correction circuits," *IEEE Transactions on Industrial Electronics*, vol. 44, no. 4, pp. 437–446, 1997.

[16] J. Kolar and H. Ertl, "Status of the techniques of three-phase rectifier systems with low effects on the mains," in *Proceedings, 21st International Telecommunication Energy Conference (INTELEC)*, 1999, Paper 14–1.

[17] Y. Jang and M. Jovanovic, "A comparative study of single-switch three-phase high-power-factor rectifiers," *IEEE Transactions on Industry Applications*, vol. 34, no. 6, pp. 1327–1334, 1998.

[18] B. Singh, B. N. Singh, A. Chandra, K. Al-Haddad, A. Pandey, and D. Kothari, "A review of three-phase improved power quality AC-DC converters," *IEEE Transactions on Industrial Electronics*, vol. 51, no. 3, pp. 641–660, 2004.

[19] R. Datta and V. Ranganathan, "Variable-speed wind power generation using doubly fed wound rotor induction machine-a comparison with alternative schemes," *IEEE Transactions on Energy Conversion*, vol. 17, no. 3, pp. 414–421, 2002.

[20] A. Miller, E. Muljadi, and D. Zinger, "A variable speed wind turbine power control," *IEEE Transactions on Energy Conversion*, vol. 12, no. 2, pp. 181–186, 1997.

[21] S. Roy, "Optimal planning of wind energy conversion systems over an energy scenario," *IEEE Transactions on Energy Conversion*, vol. 12, no. 3, pp. 248–254, 1997.

[22] J. Miret, M. Castilla, A. Camacho, L. García de Vicuña, and J. Matas, "Control scheme for photovoltaic three-phase inverters to minimize peak currents during unbalanced grid-voltage sags," *IEEE Transactions on Power Electronics*, vol. 27, no. 10, pp. 4262–4271, 2012.

[23] B. Sahan, A. Vergara, N. Henze, A. Engler, and P. Zacharias, "A single-stage PV module integrated converter based on a low-power current-source inverter," *IEEE Transactions on Industrial Electronics*, vol. 55, no. 7, pp. 2602–2609, 2008.

[24] C. Cecati, A. Dell'Aquila, and M. Liserre, "A novel three-phase single-stage distributed power inverter," *IEEE Transactions on Power Electronics*, vol. 19, no. 5, pp. 1226–1233, 2004.

[25] Z. Du, B. Ozpineci, L. Tolbert, and J. Chiasson, "DC–AC cascaded h-bridge multilevel boost inverter with no inductors for electric/hybrid electric vehicle applications," *IEEE Transactions on Industry Applications*, vol. 45, no. 3, pp. 963–970, 2009.

[26] H.-C. Chang and C.-M. Liaw, "An integrated driving/charging switched reluctance motor drive using three-phase power module," *IEEE Transactions on Industrial Electronics*, vol. 58, no. 5, pp. 1763–1775, 2011.

[27] R. Pena, J. Clare, and G. Asher, "Doubly fed induction generator using back-to-back PWM converters and its application to variable-speed wind-energy generation," *IEE Proceedings on Electric Power Applications*, vol. 143, no. 3, pp. 231–241, 1996.

[28] C.-C. Hou, C.-C. Shih, P.-T. Cheng, and A. M. Hava, "Common-mode voltage reduction pulsewidth modulation techniques for three-phase grid-connected converters," *IEEE Transactions on Power Electronics*, vol. 28, no. 4, pp. 1971–1979, 2013.

[29] K. Jezernik, "VSS control of unity power factor," *IEEE Transactions on Industrial Electronics*, vol. 46, no. 2, pp. 325–332, 1999.

[30] J. Rodriguez, J. Dixon, J. Espinoza, J. Pontt, and P. Lezana, "PWM regenerative rectifiers: state of the art," *IEEE Transactions on Industrial Electronics*, vol. 52, no. 1, pp. 5–22, 2005.

[31] J. W. A. Wilson, "The forced-commutated inverter as a regenerative rectifier," *IEEE Transactions on Industry Applications*, vol. IA-14, no. 4, pp. 335–340, 1978.

[32] B.-T. Ooi, J. C. Salmon, J. W. Dixon, and A. B. Kulkarni, "A three-phase controlled-current PWM converter with leading power factor," *IEEE Transactions on Industry Applications*, vol. IA-23, no. 1, pp. 78–84, 1987.

[33] R. Wu, S. Dewan, and G. Slemon, "A PWM AC-to-DC converter with fixed switching frequency," *IEEE Transactions on Industry Applications*, vol. 26, no. 5, pp. 880–885, 1990.

[34] J. W. Dixon and B.-T. Ooi, "Indirect current control of a unity power factor sinusoidal current boost type three-phase rectifier," *IEEE Transactions on Industrial Electronics*, vol. 35, no. 4, pp. 508–515, 1988.

[35] R. Wu, S. Dewan, and G. Slemon, "Analysis of an AC-to-DC voltage source converter using PWM with phase and amplitude control," *IEEE Transactions on Industry Applications*, vol. 27, no. 2, pp. 355–364, 1991.

[36] T. Ohnishi, "Three phase PWM converter/inverter by means of instantaneous active and reactive power control," in *Proceedings, International Conference on Industrial Electronics, Control and Instrumentation (IECON)*, 1991, vol. 1, pp. 819–824.

[37] M. Liserre, A. Dell'Aquila, and F. Blaabjerg, "An overview of three-phase voltage source active rectifiers interfacing the utility," in *Proceedings, IEEE Power Tech Conference*, 2003, vol. 3, pp. 1–7.

[38] H. Sugimoto, S. Morimoto, and M. Yano, "A high performance control method of a voltage-type PWM converter," in *Proceedings, 19th Annual IEEE Power Electronics Specialists Conference (PESC)*, 1988, vol. 1, pp. 360–368.

[39] C. Rim, N. Choi, G. Cho, and G. Cho, "A complete DC and AC analysis of three-phase controlled-current PWM rectifier using circuit d-q transformation," *IEEE Transactions on Power Electronics*, vol. 9, no. 4, pp. 390–396, 1994.

[40] V. Blasko and V. Kaura, "A new mathematical model and control of a three-phase AC-DC voltage source converter," *IEEE Transactions on Power Electronics*, vol. 12, no. 1, pp. 116–123, 1997.

[41] H. Komurcugil and O. Kukrer, "A novel current-control method for three-phase PWM AC/DC voltage-source converters," *IEEE Transactions on Industrial Electronics*, vol. 46, no. 3, pp. 544–553, 1999.

[42] X. Wang, X. Ruan, S. Liu, and C. K. Tse, "Full feedforward of grid voltage for grid-connected inverter with LCL filter to suppress current distortion due to grid voltage harmonics," *IEEE Transactions on Power Electronics*, vol. 25, no. 12, pp. 3119–3127, 2010.

[43] A. Schonung and H. Stemmler, "Static frequency changers with subharmonic control in conjunction with reversible variable speed AC drives," *Brown Boueri Review*, pp. 555–577, 1964.

[44] H. van der Broeck, H.-C. Skudelny, and G. Stanke, "Analysis and realization of a pulsewidth modulator based on voltage space vectors," *IEEE Transactions on Industry Applications*, vol. 24, no. 1, pp. 142–150, 1988.

[45] T. M. Rowan, R. J. Kerkman, and T. A. Lipo, "Operation of naturally sampled current regulators in the transition mode," *IEEE Transactions on Industry Applications*, vol. IA-23, no. 4, pp. 586–596, 1987.

[46] J. Holtz, "Pulsewidth modulation-a survey," *IEEE Transactions on Industrial Electronics*, vol. 39, no. 5, pp. 410–420, 1992.

[47] A. M. Hava, R. Kerkman, and T. Lipo, "Carrier-based PWM-VSI overmodulation strategies: analysis, comparison, and design," *IEEE Transactions on Power Electronics*, vol. 13, no. 4, pp. 674–689, 1998.

[48] J. Holtz, W. Lotzkat, and A. Khambadkone, "On continuous control of PWM inverters in the overmodulation range including the six-step mode," *IEEE Transactions on Power Electronics*, vol. 8, no. 4, pp. 546–553, 1993.

[49] R. Kerkman, T. Rowan, D. Leggate, and B. Seibel, "Control of PWM voltage inverters in the pulse dropping region," *IEEE Transactions on Power Electronics*, vol. 10, no. 5, pp. 559–565, 1995.

[50] V. Kaura and V. Blasko, "A new method to extend linearity of a sinusoidal PWM in the overmodulation region," *IEEE Transactions on Industry Applications*, vol. 32, no. 5, pp. 1115–1121, 1996.

[51] M. Huang, S.-C. Wong, C. K. Tse, and X. Ruan, "Catastrophic bifurcation in three-phase voltage-source converters," *IEEE Transactions on Circuits and Systems—Part I: Regular Papers*, vol. 60, no. 4, pp. 1062–1071, 2013.

[52] I. Barbi and F. Batista, "Space vector modulation for two-level unidirectional PWM rectifiers," *IEEE Transactions on Power Electronics*, vol. 25, no. 1, pp. 178–187, 2010.

[53] H.-M. Ryu, J.-H. Kim, and S.-K. Sul, "Analysis of multiphase space vector pulse-width modulation based on multiple d-q spaces concept," *IEEE Transactions on Power Electronics*, vol. 20, no. 6, pp. 1364–1371, 2005.

[54] S. Bolognani and M. Zigliotto, "Novel digital continuous control of SVM inverters in the overmodulation range," *IEEE Transactions on Industry Applications*, vol. 33, no. 2, pp. 525–530, 1997.

[55] Z. Bai, X. Ruan, and Z. Zhang, "A generic six-step direct PWM (SS-DPWM) scheme for current source converter," *IEEE Transactions on Power Electronics*, vol. 25, no. 3, pp. 659–666, 2010.

[56] M. Liserre, R. Teodorescu, and F. Blaabjerg, "Stability of photovoltaic and wind turbine grid-connected inverters for a large set of grid impedance values," *IEEE Transactions on Power Electronics*, vol. 21, no. 1, pp. 263–272, 2006.

[57] G. Ledwich and H. Sharma, "Connection of inverters to a weak grid," in *Proceedings, IEEE 31st Annual Power Electronics Specialists Conference (PESC)*, 2000, vol. 2, pp. 1018–1022.

[58] I. Hiskens and E. Fleming, "Control of inverter-connected sources in autonomous microgrids," in *Proceedings, American Control Conference*, 2008, pp. 586–590.

[59] J. Sun, "Small-signal methods for AC distributed power systems: a review," *IEEE Transactions on Power Electronics*, vol. 24, no. 11, pp. 2545–2554, 2009.

[60] ——, "Impedance-based stability criterion for grid-connected inverters," *IEEE Transactions on Power Electronics*, vol. 26, no. 11, pp. 3075–3078, 2011.

[61] M. Cespedes and J. Sun, "Modeling and mitigation of harmonic resonance between wind turbines and the grid," in *Proceedings, IEEE Energy Conversion Congress and Exposition (ECCE)*, 2011, pp. 2109–2116.

[62] ——, "Methods for stability analysis of unbalanced three-phase systems," in *Proceedings, IEEE Energy Conversion Congress and Exposition (ECCE)*, 2012, pp. 3090–3097.

[63] X. Chen and J. Sun, "A study of renewable energy system harmonic resonance based on a DG test-bed," in *Proceedings, Twenty-Sixth Annual IEEE Applied Power Electronics Conference and Exposition (APEC)*, 2011, pp. 995–1002.

[64] H. O. Wang, E. H. Abed, and A. M. A. Hamdan, "Bifurcations, chaos, and crises in voltage collapse of a model power system," *IEEE Transactions on Circuits and Systems—Part I: Fundamental Theory and Applications*, vol. 41, no. 4, pp. 294–302, 1994.

[65] S. D. Sudhoff, S. F. Glover, P. T. Lamm, D. H. Schmucker, and D. E. Delisle, "Admittance space stability analysis of power electronic systems," *IEEE Transactions on Aerospace and Electronic Systems*, vol. 36, no. 3, pp. 965–973, 2000.

[66] M. Belkhayat, R. Cooley, and E. H. Abed, "Stability and dynamics of power systems with regulated converters," in *Proceedings, IEEE International Symposium Circuits and Systems (ISCAS)*, 1995, pp. 143–145.

[67] R. D. Middlebrook, "Input filter consideration in design and application of switching regulators," in *Proceedings, IEEE Industial Applications Society Annual Meeting*, 1976, pp. 94–107.

[68] F. C. Lee and Y. Yu, "Input-filter design for switching regulators," *IEEE Transactions on Aerospace and Electronic Systems*, vol. AES-15, no. 5, pp. 627 –634, 1979.

[69] S. Kelkar and F. C. Lee, "Adaptive input filter compensation for switching regulators," *IEEE Transactions on Aerospace and Electronic Systems*, vol. AES-20, no. 1, pp. 57–66, 1984.

[70] P. Barbosa, F. Canales, J.-C. Crebier, and F. C. Lee, "Interleaved three-phase boost rectifiers operated in the discontinuous conduction mode: analysis, design considerations and experimentation," *IEEE Transactions on Power Electronics*, vol. 16, no. 5, pp. 724–734, 2001.

[71] V. Singh, "Formulation of a criterion for the absence of limit cycles in digital filters designed with one quantizer," *IEEE Transactions on Circuits and Systems*, vol. 32, no. 10, pp. 1062–1064, 1985.

[72] P. Mantovanelli and I. Barbi, "A new current-fed, isolated PWM DC-DC converter," *IEEE Transactions on Power Electronics*, vol. 11, no. 3, pp. 431–438, 1996.

[73] H. Kar and V. Singh, "A new criterion for the overflow stability of second-order state-space digital filters using saturation arithmetic," *IEEE Transactions on Circuits and Systems—Part I: Fundamental Theory and Applications*, vol. 45, no. 3, pp. 311–313, 1998.

[74] X. Feng, J. Liu, and F. C. Lee, "Impedance specifications for stable DC distributed power systems," *IEEE Transactions on Power Electronics*, vol. 17, no. 2, pp. 157–162, 2002.

[75] J. Liu, X. Feng, F. C. Lee, and D. Borojevich, "Stability margin monitoring for DC distributed power systems via perturbation approaches," *IEEE Transactions on Power Electronics*, vol. 18, no. 6, pp. 1254–1261, 2003.

[76] P.-L. Wong, F. C. Lee, and X. Zhou, "Stability study of PC power system," *IEEE Transactions on Industry Applications*, vol. 37, no. 1, pp. 73–80, 2001.

[77] Y. Familiant, J. Huang, K. Corzine, and M. Belkhayat, "New techniques for measuring impedance characteristics of three-phase AC power systems," *IEEE Transactions on Power Electronics*, vol. 24, no. 7, pp. 1802–1810, 2009.

[78] J. Huang, K. Corzine, and M. Belkhayat, "Small-signal impedance measurement of power-electronics-based AC power systems using line-to-line current injection," *IEEE Transactions on Power Electronics*, vol. 24, no. 2, pp. 445–455, 2009.

[79] ——, "Online synchronous machine parameter extraction from small-signal injection techniques," *IEEE Transactions on Energy Conversion*, vol. 24, no. 1, pp. 43–51, 2009.

[80] P. Xiao, G. Venayagamoorthy, K. Corzine, and J. Huang, "Recurrent neural networks based impedance measurement technique for power electronic systems," *IEEE Transactions on Power Electronics*, vol. 25, no. 2, pp. 382–390, 2010.

[81] M. Belkhayat, "Stability criteria for AC power systems with regulated loads," Ph.D. dissertation, Purdue University, 1997.

[82] L. Moran, P. Ziogas, and G. Joos, "Design aspects of synchronous PWM rectifier-inverter systems under unbalanced input voltage conditions," *IEEE Transactions on Industry Applications*, vol. 28, no. 6, pp. 1286–1293, 1992.

[83] A. Stankovic and T. Lipo, "A novel control method for input output harmonic elimination of the PWM boost type rectifier under unbalanced operating conditions," *IEEE Transactions on Power Electronics*, vol. 16, no. 5, pp. 603–611, 2001.

[84] H.-S. Song and K. Nam, "Dual current control scheme for PWM converter under unbalanced input voltage conditions," *IEEE Transactions on Industrial Electronics*, vol. 46, no. 5, pp. 953–959, 1999.

[85] D. Hamill and D. Jeffries, "Subharmonics and chaos in a controlled switched-mode power converter," *IEEE Transactions on Circuits and Systems*, vol. 35, no. 8, pp. 1059–1061, 1988.

[86] J. Deane and D. Hamill, "Instability, subharmonics and chaos in power electronic systems," in *Proceedings, 20th Annual IEEE Power Electronics Specialists Conference (PESC)*, 1989, vol. 1, pp. 34–42.

[87] ——, "Instability, subharmonics, and chaos in power electronic systems," *IEEE Transactions on Power Electronics*, vol. 5, no. 3, pp. 260–268, 1990.

[88] P. T. Krein and R. M. Bass, "Types of instability encountered in simple power electronic circuits: unboundedness, chattering, and chaos," in *Proceedings, Fifth Annual Applied Power Electronics Conference and Exposition (APEC)*, 1990, pp. 191–194.

[89] C. K. Tse, "Flip bifurcation and chaos in three-state boost switching regulators," *IEEE Transactions on Circuits and Systems—Part I: Fundamental Theory and Applications*, vol. 41, no. 1, pp. 16–23, 1994.

[90] W. Chan and C. K. Tse, "On the form of feedback function that can lead to chaos in discontinuous-mode DC/DC converters," in *Proceedings, 28th*

Annual IEEE Power Electronics Specialists Conference (PESC), 1997, vol. 2, pp. 1317–1322.

[91] A. El Aroudi, L. Benadero, E. Toribio, and G. Olivar, "Hopf bifurcation and chaos from torus breakdown in a PWM voltage-controlled DC-DC boost converter," *IEEE Transactions on Circuits and Systems—Part I: Fundamental Theory and Applications*, vol. 46, no. 11, pp. 1374–1382, 1999.

[92] J. Deane, "Chaos in a current-mode controlled boost DC-DC converter," *IEEE Transactions on Circuits and Systems—Part I: Fundamental Theory and Applications*, vol. 39, no. 8, pp. 680–683, 1992.

[93] W. Chan and C. K. Tse, "Study of bifurcations in current-programmed DC/DC boost converters: from quasiperiodicity to period-doubling," *IEEE Transactions on Circuits and Systems—Part I: Fundamental Theory and Applications*, vol. 44, no. 12, pp. 1129–1142, 1997.

[94] S. Banerjee and G. Verghese, Eds., *Nonlinear Phenomena in Power Electronics: Attractors, Bifurcations, Chaos, and Nonlinear Control*. IEEE Press, 2001.

[95] H. H. C. Iu and C. K. Tse, "Instability and bifurcation in parallel-connected buck converters under a master-slave current sharing scheme," in *Proceedings, IEEE 31st Annual Power Electronics Specialists Conference (PESC)*, 2000, vol. 2, pp. 708–713.

[96] ——, "Bifurcation behavior in parallel-connected buck converters," *IEEE Transactions on Circuits and Systems—Part I: Fundamental Theory and Applications*, vol. 48, no. 2, pp. 233–240, 2001.

[97] ——, "Study of low-frequency bifurcation phenomena of a parallel-connected boost converter system via simple averaged models," *IEEE*

Transactions on Circuits and Systems—Part I: Fundamental Theory and Applications, vol. 50, no. 5, pp. 679–685, 2003.

[98] Y. Huang, H. H. C. Iu, and C. K. Tse, "Boundaries between fast-and slow-scale bifurcations in parallel-connected buck converters," in *Proceedings, IEEE International Symposium on Circuits and Systems (ISCAS)*, 2007, pp. 2419–2422.

[99] Y. Chen, C. K. Tse, S.-S. Qiu, L. Lindenmuller, and W. Schwarz, "Coexisting fast-scale and slow-scale instability in current-mode controlled DC/DC converters: analysis, simulation and experimental results," *IEEE Transactions on Circuits and Systems—Part I: Regular Papers*, vol. 55, no. 10, pp. 3335–3348, 2008.

[100] M. Orabi and T. Ninomiya, "Nonlinear dynamics of power-factor-correction converter," *IEEE Transactions on Industrial Electronics*, vol. 50, no. 6, pp. 1116–1125, 2003.

[101] S.-C. Wong, C. K. Tse, M. Orabi, and T. Ninomiya, "The method of double averaging: an approach for modeling power-factor-correction switching converters," *IEEE Transactions on Circuits and Systems—Part I: Regular Papers*, vol. 53, no. 2, pp. 454–462, 2006.

[102] G. Chu, C. K. Tse, S.-C. Wong, and S.-C. Tan, "A unified approach for the derivation of robust control for boost PFC converters," *IEEE Transactions on Power Electronics*, vol. 24, no. 11, pp. 2531–2544, 2009.

[103] Z. Süto and I. Nagy, "Analysis of nonlinear phenomena and design aspects of three-phase space-vector-modulated converters," *IEEE Transactions on Circuits and Systems—Part I: Fundamental Theory and Applications*, vol. 50, no. 8, pp. 1064–1071, 2003.

[104] Y. Gao and K. T. Chau, "Hopf bifurcation and chaos in synchronous reluctance motor drives," *IEEE Transactions on Energy Conversion*, vol. 19, no. 2, pp. 296–302, 2004.

[105] G. Chen, D. J. Hill, and X. Yu, Eds., *Bifurcation Control: Theory and Application*. Berlin: Springer, 2003.

[106] G. Poddar, K. Chakrabarty, and S. Banerjee, "Experimental control of chaotic behavior of buck converter," *IEEE Transactions on Circuits and Systems—Part I: Fundamental Theory and Applications*, vol. 42, no. 8, pp. 502–504, 1995.

[107] P. C. Krause, O. Wasynczuk, and S. D. Sudhoff, *Analysis of Electric Machinery*. New York: IEEE Press, 1995.

[108] B. C. Kuo and F. Golnaraghi, *Automatic Control Systems*. New York: John Wiley & Sons, 2003.

[109] A. M. Hava, "Carrier based PWM-VSI drives in the overmodulation region," Ph.D. dissertation, University of Wisconsin-Madison, 1998.

[110] N. Zargari and G. Joos, "Performance investigation of a current-controlled voltage-regulated PWM rectifier in rotating and stationary frames," *IEEE Transactions on Industrial Electronics*, vol. 42, no. 4, pp. 396–401, 1995.

[111] P. Verdelho and G. Marques, "DC voltage control and stability analysis of PWM-voltage-type reversible rectifiers," *IEEE Transactions on Industrial Electronics*, vol. 45, no. 2, pp. 263–273, 1998.

[112] V. Caliskan, D. Perreault, T. Jahns, and J. Kassakian, "Analysis of three-phase rectifiers with constant-voltage loads," *IEEE Transactions on Circuits and Systems—Part I: Fundamental Theory and Applications*, vol. 50, no. 9, pp. 1220–1225, 2003.

[113] T. Jin, L. Li, and K. M. Smedley, "A universal vector controller for four-quadrant three-phase power converters," *IEEE Transactions on Circuits and Systems—Part I: Regular Papers*, vol. 54, no. 2, pp. 377–390, 2007.

[114] Y. Jiang, H. Mao, F. C. Lee, and D. Borojevic, "Simple high performance three-phase boost rectifiers," in *Proceedings, 25th Annual IEEE Power Electronics Specialists Conference (PESC)*, 1994, vol. 2, pp. 1158–1163.

[115] A. H. Nayfeh and B. Balachandran, *Applied Nonlinear Dynamics: Analytical, Computational, and Experimental Methods*. New York: Wiley, 1995.

[116] C. K. Tse, *Complex Behavior of Switching Power Converters*. Boca Raton: CRC Press, 2003.

[117] C. K. Tse and M. Li, "Design-oriented bifurcation analysis of power electronics systems," *International Journal of Bifurcation and Chaos*, vol. 21, no. 6, pp. 1523–1537, 2011.

[118] E. Rodriguez, A. El Aroudi, F. Guinjoan, and E. Alarcon, "A ripple-based design-oriented approach for predicting fast-scale instability in DC-DC switching power supplies," *IEEE Transactions on Circuits and Systems—Part I: Regular Papers*, vol. 59, no. 1, pp. 215–227, 2012.

[119] Y.-R. Mohamed, "Mitigation of converter-grid resonance, grid-induced distortion, and parametric instabilities in converter-based distributed generation," *IEEE Transactions on Power Electronics*, vol. 26, no. 3, pp. 983–996, 2011.

[120] C. Wan, M. Huang, C. K. Tse, S.-C. Wong, and X. Ruan, "Irreversible bifurcation phenomenon in power-grid connected converter systems," *International Journal of Bifurcation and Chaos*, vol. 22, no. 6, pp. 1 250 155–1–8, 2012.

[121] ——, "Nonlinear behavior and instability in a three-phase boost rectifier connected to a nonideal power grid with an interacting load," *IEEE Transactions on Power Electronics*, vol. 28, no. 7, pp. 3255–3265, 2013.

[122] P. T. Krein, J. Bentsman, R. M. Bass, and B. L. Lesieutre, "On the use of averaging for the analysis of power electronic systems," *IEEE Transactions on Power Electronics*, vol. 5, no. 2, pp. 182–190, 1990.

[123] M. Huang, C. K. Tse, and S.-C. Wong, "Line-frequency instability of three-phase PFC power supplies connecting to non-ideal power grid," in *Proceedings, IEEE International Symposium on Circuits and Systems (ISCAS)*, 2012, pp. 213–216.

[124] M. Huang, C. K. Tse, S.-C. Wong, C. Wan, and X. Ruan, "Low-frequency Hopf bifurcation and its effects on stability margin in three-phase PFC power supplies connected to non-ideal power grid," *IEEE Transactions on Circuits and Systems—Part I: Regular Papers*, to appear.